Waste Heat Recovery from a Compression Ignition Engine using a Combined Diesel Particulate Filter Heat Exchanger

By

Bailey Ann Spickler

Submitted to the graduate degree program in Mechanical Engineering and the Graduate Faculty of the University of Kansas in partial fulfillment of the requirements for the degree of Master of Science.

Chair: Dr. Christopher Depcik

Dr. Theodore L. Bergman

Dr. Ronald L. Dougherty

Date Defended: November 30th, 2018

The thesis committee for Bailey Ann Spickler certifies that this is
the approved version of the following thesis:

Waste Heat Recovery from a Compression Ignition Engine using a Combined Diesel Particulate Filter Heat Exchanger

Chair: Dr. Christopher Depcik

Date Approved: February 12th, 2019

Abstract

Compression ignition (CI) engines have been a figurehead in the transportation industry for decades. However, as environmental regulations dictate increasingly strict emissions guidelines for engines, technologies must accordingly advance. To this end, this thesis describes the work of validating a combined diesel particulate filter heat exchanger (DPFHX) for CI engine exhaust waste heat recovery (WHR) in a Rankine Cycle (RC), a concept introduced in the first chapter of this thesis.

The second chapter includes a comprehensive literature review, indicating the increasing prevalence of WHR in the literature. Additionally, with RC as the principal system for WHR and engine exhaust as the primary heat source, this research is exceptionally relevant. Furthermore, the primary aspects of an RC WHR system requiring individual optimization are the heat exchangers and expanders along with working fluid selection.

As such, the third chapter discusses experiments to analyze and compare the DPFHX with various working fluids; thus, incorporating the literature trends of working fluid comparison and component specificity in the methodology. Consequently, in the DPFHX, water achieved a higher heat transfer rate by over 60% than the 50% by volume mixture of water and ethylene glycol, the two optimal working fluids in the apparatus without DPF cores. However, alterations made to the DPF cores' outer diameters and lengths when installing them in the heat exchanger tubes prevented them from achieving the expected outcome (i.e., improving apparatus performance). Finally, the fourth chapter links the conclusions from this work to recommendations for future efforts to investigate DPFHXs.

Acknowledgements

First, I'd like to thank my advisor, Dr. Christopher Depcik, for providing me with the opportunity to pursue my Master of Science, as well as the tremendous guidance, support, and revisions he provided along the way. I'd also like to recognize Dr. Bergman and Dr. Dougherty for serving on my committee and lending their expertise to the research I have conducted. Moreover, I wish to acknowledge Madison and Lila Self, as well as the staff of the Madison and Lila Self Graduate Fellowship, for providing me with the funding and professional development to pursue and improve my graduate education. Furthermore, without the assistance, recommendations, and witticisms of my lab mates, specifically Jon Mattson, Charu Srivasta, Shah Saud Alam, and Khalaf Alzeeby, this process would have been vastly more difficult and far less enjoyable. I'd also like to recognize Dr. Charles Sprouse for setting the foundation for my research.

On a more personal note, I cannot begin to thank my parents, Keith and Robin, enough for the lifetime of encouragement and strength they have provided. They emboldened me to strive for whatever I desired, and I add this thesis to the list of achievements that would have been impossible without them. I would also like to recognize my best friend Nick for helping me through the daily challenges and triumphs I faced, ensuring that there were good moments on even the worst of days and regularly inspiring me to improve. Additionally, I'd like to thank my friends, Cheyenne, Deanna, Andie, and Allyson, and my siblings, Cole and Brittany, for keeping me stable and loved over the years. And finally, I'd like to acknowledge Jax, though he may never see this, for being my greatest daily motivation to complete my work.

Table of Contents

Figures

Tables

Nomenclature

Abbreviations

1-D	one-dimensional
3-D	three-dimensional
50/50	50% by volume mixture
ARC	absorption refrigeration cycle
BC	Brayton cycle
BRC	basic Rankine Cycle configuration
BSFC	brake specific fuel consumption
CAC	charge air cooler
CCE-RC	confluent cascade expansion Rankine Cycle
CFD	computational fluid dynamics
CI	compression ignition
CNG	compressed natural gas
CRC	cascade Rankine Cycle configuration
CSCR	component-to-system cost ratio
CTPC	CO_2 transcritical power cycle
CTRC	CO_2-based transcritical Rankine cycle

DOC	diesel oxidation catalysts
DPF	diesel particulate filter
DPFHX	diesel particulate filter heat exchanger
DPP	depreciated payback period
DRC	dual-loop Rankine Cycle configuration
EG	ethylene glycol
EGMR-RC	Combined exhaust gas mixture recirculation and Rankine Cycle
EGR	exhaust gas recirculation
EPA	Environmental Protection Agency
EPC	electricity production cost
ESC	European Stationary Cycle
FP	free piston
FPLG	free piston coupled to a linear generator
GHG	greenhouse gas
GMV	generalize minimum variance
GUI	graphical user interface
GWP	global warming potential
HC	hydrocarbons
HD	heavy-duty

HEX	heat exchanger
HT	high temperature
IC	internal combustion
ICE	internal combustion engine
ID	inner diameter
LEC	levelized energy cost
LP	low-pressure
LSQ	least-squares factor
LT	low temperature
MP	mid-pressure
NEDC	New European Driving Cycle
NI	National Instruments
NPV	net present value
ODP	ozone depletion potential
OECE	overall energy conversion efficiency
ORC	Organic Rankine Cycle
OS-RC	combined intermediate thermal-oil storage and Rankine cycles
P-CTPC	CO_2 transcritical power cycle with preheat
PG	propylene glycol

PM	particulate matter
PRC	preheat Rankine Cycle configuration
PR-CTPC	CO_2 transcritical power cycle with preheat and regeneration
PR-CTRC	CO_2-based transcritical Rankine cycle with preheat and regeneration
PRRC	preheat and regenerative Rankine Cycle configuration
RC	Rankine Cycle
RC-ORC	cascaded Rankine and Organic Rankine cycles
R-CTPC	CO_2 transcritical power cycle with regeneration
RPM	revolutions per minute
RRC	regenerative Rankine Cycle configuration
SCO	selective catalytic oxidation
SCR	selective catalytic reduction
SFC	single flash cycle
SI	spark-ignition
SIC	specific investment cost
SIR	savings-to-investment ratio
TDMS	technical data management solution
TEG	thermoelectric generator
TEG-RC	coupled thermoelectric generator with a Rankine Cycle

TFC	trilateral flash cycle
TKE	turbulent kinetic energy
TRC	transcritical Rankine Cycle
VC	volume coefficient
WHR	waste heat recovery

Variables

A	area [m^2]
a	constant coefficient [-]
b	constant coefficient [-]
Bi	Biot number [-]
c	specific heat (liquid) [kJ/kg·K]
c_p	specific heat (gases) [kJ/kg·K]
d	constant coefficient [-]
F	correction factor [-]
h	convection heat transfer coefficient [W/m^2K]; enthalpy [kJ/kg]
$\bar{h}$	molar enthalpy [kJ/kg·kmol]
J	product of correction factors accounting for tube arrangement, recirculation flow, and temperature gradient [-]
k	thermal conductivity [W/m·K]

L	tube length [m]
L_c	characteristic length [m]
$LMTD$	log mean temperature difference [K]
M	molecular weight [kg/kmol]
$\dot{m}$	fluid mass flow rate [kg/s]
$\left(\dot{m} c_p\right)$	heat capacity [kJ/s·K]
$\dot{n}$	molar flow rate [mol/s]
NM	number of species [-]
Nu	Nusselt number [-]
Pr	Prandtl number [-]
Q	heat transfer rate [W]
R	thermal resistance [K/W]
r	radius [m]
Re	Reynolds number [-]
R_u	universal gas constant [kJ/kmol·K]
T	temperature; shell-side temperature in Figure 3.9 [K]
t	tube-side temperature in Figure 3.9 [K]
U	overall heat transfer coefficient [W/m^{2}K]
W	power [W]

Y	mass fraction [-]
Z	number of air molecules for balanced lean combustion equation [moles]

Greek Variables

α	constant coefficient [-]
β	constant coefficient [K^{-1}]
Δ	difference or change in a quantity [-]
δ	constant coefficient [K^{-3}]
ε	heat exchanger effectiveness [-]
φ	constant coefficient [K^{-4}]
γ	constant coefficient [K^{-2}]

Subscripts & Modifiers

1-10	differentiate between multiple variables of the same type
a	first heat exchanger temperature difference, defined based on heat exchanger flow type
amb	ambient
b	second heat exchanger temperature difference, defined based on heat exchanger flow type
bl	hydrodynamically developing
c	cold fluid
calculated	calculated

cond	conduction
conv	convection
core	DPF core
correlation	correlation
diff	difference
ex	exhaust
experimental	experimental
fd	fully developed
h	hot fluid
HT	heat transfer
i	species
ideal	ideal
in	inlet
initial	initial
inner	inner
laminar	laminar
lit	literature
loss	losses
min	minimum

new	new
opt	optimized
out	outlet
outer	outer
S	surface
shell	shell
th	thermally developing
total	total
tube	tube of the heat exchanger
turbulent	turbulent
worst	worst case
wf	working fluid
α	inlet with ambient losses considered
β	outlet with ambient losses considered
$-$	molar
$\cdot$	rate
^	average

Chapter 1: Introduction

1.1 Introduction to Waste Heat Recovery

Since its inception, the internal combustion (IC) engine has been a primary source of power for the transportation field. In an IC engine, a fuel and air mixture is combusted, with the pressure from this combustion process subsequently moving a piston; thus, the engine transforms the chemical potential of the fuel into mechanical work. One type of IC engine is known as the compression ignition (CI) or diesel engine in which the air and fuel mixture ignites due to the physical compression of the mixture by the piston without an external spark. Two specific operating characteristics of CI engines include lean air-to-fuel ratios and generally heterogeneous combustion, which leads to nitrogen oxides (NO_x) and particulate matter (PM or colloquially, soot) emissions, respectively [1]. While other chemical species, such as nitrogen (N_2), oxygen (O_2), water (H_2O), carbon dioxide (CO_2), carbon monoxide (CO), and hydrocarbons (HC), also occur in the exhaust, NO_x and PM are the primary toxic species and are regulated in many countries [2].

Generally, NO_x forms due to relatively high combustion temperatures at lean equivalence ratios (i.e., less than one), which allows excess O_2 to react with N_2 [2]. While catalytic devices exist to moderate NO_x, the operation of CI engines at lean equivalence ratios diminishes the efficacy of such catalysts [1]. Concerning NO_x mitigation, the primary in-cylinder technique used is exhaust gas recirculation (EGR), which decreases NO_x formation by lowering combustion temperatures within the cylinder [1]. In contrast, PM principally forms from poorly

mixed, relatively cool fuel rich pockets in the combustion chamber; however, its exact composition depends on engine conditions [1]. Once formed, the removal of PM can only occur using a filter to trap particles from the exhaust stream.

While the lessening of NO_x via the aforementioned tactics is achievable, it brings with it additional challenges due to the so-called NO_x-PM tradeoff. As stated, NO_x forms due to excess O_2 reacting with N_2 at high temperatures. However, if the engine is run at a richer or larger equivalence ratio and/or a lower combustion temperature, the reduction of NO_x comes at the cost of increased PM formation. In contrast, if there are higher combustion temperatures and leaner equivalence ratios and/or better mixing of the fuel/air mixture, less PM is generated at the cost of elevated NO_x emissions. As such, the formation of each species is closely linked, thereby connecting their removal in catalytic aftertreatment systems.

As shown in Figure 1.1, there are multiple distinct types of aftertreament devices for CI engines, with each apparatus targeting different emitted species. These components are often implemented in a series arrangement in order to address all hazardous emissions. Here, the primary method of abatement occurs in the form of catalytic reactions. Specifically, diesel oxidation catalyst (DOC) devices remove HC and CO; whereas, selective catalytic reduction (SCR) removes NO_x through the addition of a diesel exhaust fluid (i.e., urea that decomposes into ammonia) [3]. Furthermore, if necessary, selective catalytic oxidation (SCO) can remove any remaining ammonia in the exhaust stream, since ammonia poses health hazards if emitted [3].

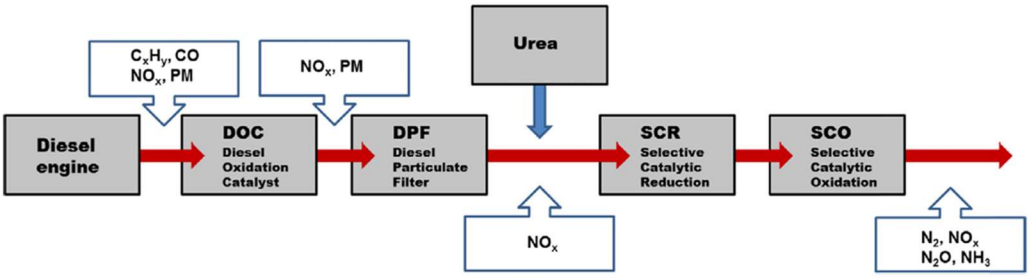

Figure 1.1: Typical diesel aftertreament system components and the associated emissions they target [3].

The remaining component of most common CI aftertreatment systems is a diesel particulate filter (DPF). DPFs utilize a porous ceramic material to capture the PM in the exhaust stream with channels alternately blocked at either end. Therefore, the exhaust gas flows through the open channels on one end of the core, where it is then forced to traverse through the porous ceramic wall of the channel due to the blockage at the end of that channel. During passage through the wall, the PM is trapped within the porous filter. Subsequently, the exhaust gas leaves the filter through the unblocked channels. Generally, DPFs experience filtration efficiencies of up to 98%, making them an attractive method of reducing PM emissions [4].

When traveling through a DPF, the exhaust gas experiences a pressure drop due to various flow mechanisms. The first of these is due to the passage of the gas through the porous DPF wall, as the permeability of the wall presents an initial impedance to the flow, creating a pressure gradient. This pressure drop changes based on the wall's soot loading, with the presence and amount of soot altering the wall's permeability [5]. Furthermore, contraction and expansion of the exhaust gas at the DPF's inlet and outlet, frictional effects of the gas entering and exiting individual DPF channels, and plugged lengths of the inlet and outlet channels contribute to the pressure drop, as well as variable influences (e.g., ash accumulation or geometric differences in

channels) [6, 7]. Subsequently, this generated pressure drop incurs a temperature decrease, while imposing backpressure on the engine, negatively affecting fuel consumption and performance.

While effective at removing PM emissions, the DPF eventually reaches its capacity for soot loading. Regeneration events (active or passive) are used to remove accumulated PM from the cores, extending the life of the filter and mitigating the negative repercussions of a highly loaded DPF (i.e., increased backpressure). Active regeneration requires temperatures of 500-600^{o}C in order for the O_2 to oxidize the PM; whereas, passive regeneration only requires temperatures around 200^{o}C while utilizing NO_2 to oxidize the PM [1]. For active regeneration, techniques such as a late fuel injection or external heating of the DPF must be implemented to reach the temperatures needed. However, for passive regeneration, catalysts are required (e.g., DOC or a catalyzed DPF) to provide the necessary NO_2 [2]. Generally, the initiation of a regeneration event is typically handled by on-board diagnostics systems that are triggered by an excessive backpressure or a specific fuel consumption metric [8, 9]. During this event, the exothermic PM oxidation reactions create high levels of thermal energy, and care must be taken to control these events in order to prevent damage, such as melting or cracking of the DPF substrate from thermal stresses [10]. Thus, regeneration initiation and control strategies are viewed as primary opportunities for improvement in DPF systems.

Through a combination of in-cylinder techniques (i.e., EGR) and aftertreatment systems (i.e., SCR, DPF, etc.), emissions concerns of CI engines can be effectively managed. However, additional issues facing CI engines stem from increasing fuel efficiency standards. In an effort to reduce carbon pollution and improve fuel efficiency, the Environmental Protection Agency

(EPA) has proposed a series of standards for medium- and heavy-duty trucks. These standards, implemented in two phases, are aimed at reducing fuel consumption, thereby decreasing the associated expense for both consumers and businesses along with diminishing greenhouse gas (GHG) emissions. Specifically, Phase 1 standards were implemented for 2014-2018 heavy-duty (HD) vehicles to reduce both carbon emissions and fuel consumption through existing technologies. Phase 2 standards, geared towards 2021-2027 HD vehicles, augment the Phase 1 standards and encourage the development of new technologies [11]. Based on the proposed Phase 2 EPA standards, diesel fuel consumption by large trucks is expected to decrease by nearly one million barrels per day over the course of the next 20 years [12]. Overall, a reduction in fuel consumption will directly result in fewer carbon emissions, but achieving such a drop requires the employment and development of technological innovations.

Hence, a primary opportunity for improving fuel efficiency of CI engines is highlighted via the estimate of one-thirds as shown Figure 1.2, which states that, of the available energy from the fuel used in combustion, only approximately one-third of this energy yields effective power. Furthermore, an additional estimated one-third is lost in the exhaust gases, and the final amount is lost to the coolant within the system, with a margin for other internal losses. From this, it is readily apparent that an opportunity exists to recover a portion of the two-thirds of fuel energy that is currently lost. Specifically, Waste Heat Recovery (WHR) is an effective method to recoup the fuel energy lost by converting the thermal energy of a heat source, in this case either the coolant or exhaust, into electrical or mechanical energy through a power cycle. Therefore, to increase the fuel efficiency of a vehicle, the energy generated from the WHR power cycle could

be utilized on-board the vehicle; thus, reducing the load on the engine and subsequently decreasing fuel consumption.

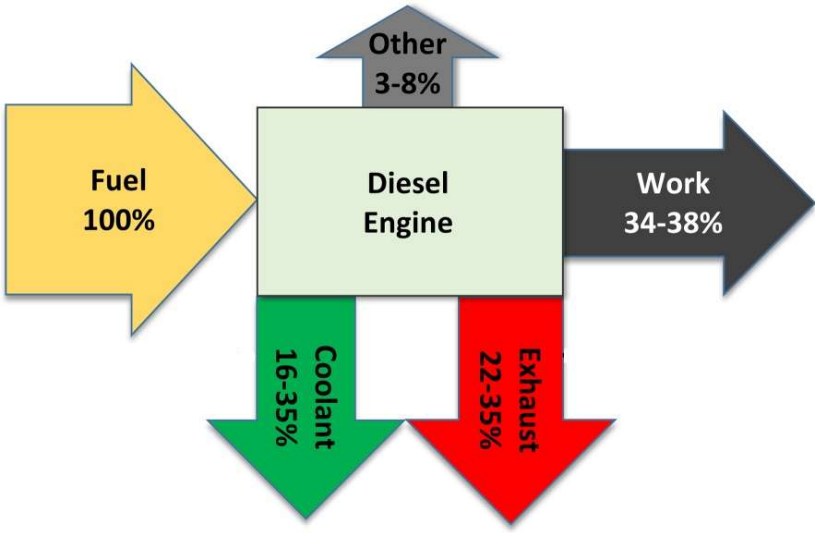

Figure 1.2: Diagram of the estimate of one-thirds for fuel energy distribution in diesel engines [13]

.

1.2 Combined Diesel Particulate Filter Heat Exchanger for WHR

Of the various power cycles available for WHR, a prevalent option is a Rankine Cycle (RC), due to its simplicity and cost effectiveness (e.g., RC having a payback period one year less than that of the Brayton Cycle [14]), as well as relatively high efficiencies with moderate temperature differences (e.g., 60-70% of Carnot efficiencies for temperature differences of approximately 350 K [15]) [16]. Traditionally, an RC consists of four components (i.e., evaporator, expander, condenser, and pump) through which a fluid is circulated. The processes taking place within an RC, as seen in Figure 1.3, can be described as follows:

- Process 1-2: Waste heat is captured from the heat source via an evaporator and transferred to the working fluid.

- Process 2-3: The working fluid is expanded, generating power.
- Process 3-4: The remaining thermal energy in the working fluid that was not used to generate power is rejected from the system by passing through a condenser.
- Process 4-1: The working fluid passes through a pump and returns to its initial state.

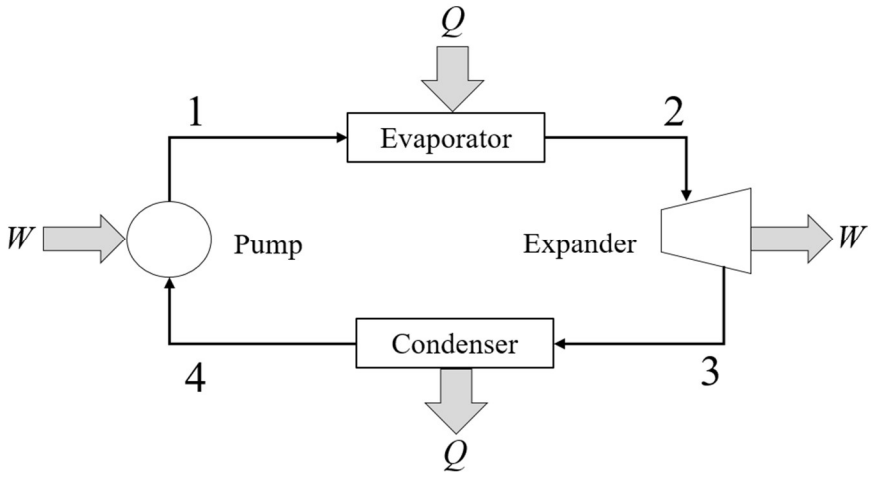

Figure 1.3: Components of an RC, where *W* represents power and *Q* represents a heat transfer rate with the associated arrows indicating their directions into or out of the system.

Accordingly, the component most directly responsible for recovering the thermal energy from the heat source is the evaporator, a heat exchanger (HEX). Both the coolant, a low temperature heat source (e.g., approximately 300 to 400 K) and the exhaust, a medium temperature heat source (e.g., approximately 500 to 900 K), can be utilized within the RC [17]. However, since the recovery potential of any heat source is highly dependent on its temperature (i.e., following the Carnot efficiency), the exhaust is a more thermodynamically attractive working fluid [18]. As a result, when installed on a vehicle, an RC-based WHR has the potential to offer around a 10% increase in overall engine efficiency [19].

For WHR implementation on-board a vehicle, consideration must be given to the location of the HEX evaporator in the exhaust stream. The catalysts used for CI engines do not require significant thermal considerations (except for warm-up), and thus do not drastically influence this determination. However, the temperature drop across the DPF, as well as the high temperature regeneration events that it experiences, greatly influence where the HEX evaporator can be placed. Specifically, installation of the HEX evaporator downstream of the DPF would not fully utilize the thermal energy of the exhaust, with temperature and subsequent energy decreases occurring across the DPF. Moreover, placement of the HEX evaporator upstream of the DPF would require greater operational changes to achieve temperatures for regeneration events (i.e., increased heating, more fuel injected late, etc.). Consequently, a novel idea is the coupling of the HEX evaporator and the DPF, creating a combined diesel particulate filter heat exchanger (DPFHX).

As shown in Figure 1.4, when creating a DPFHX, the DPF cores (brown) could be installed in the tubes (gray) of a shell-and-tube HEX, allowing continued operation as a traditional DPF. In the shell (blue) of the DPFHX, a working fluid can circulate around these tubes, extracting thermal energy from the exhaust. The DPF cores within the tubes of the HEX would create further heat transfer pathways, namely convection within the channels and the walls of the cores along with conduction through the cores. These pathways would facilitate additional heat transfer, generating the potential for more effective WHR and greater improvements in engine efficiency than traditional WHR.

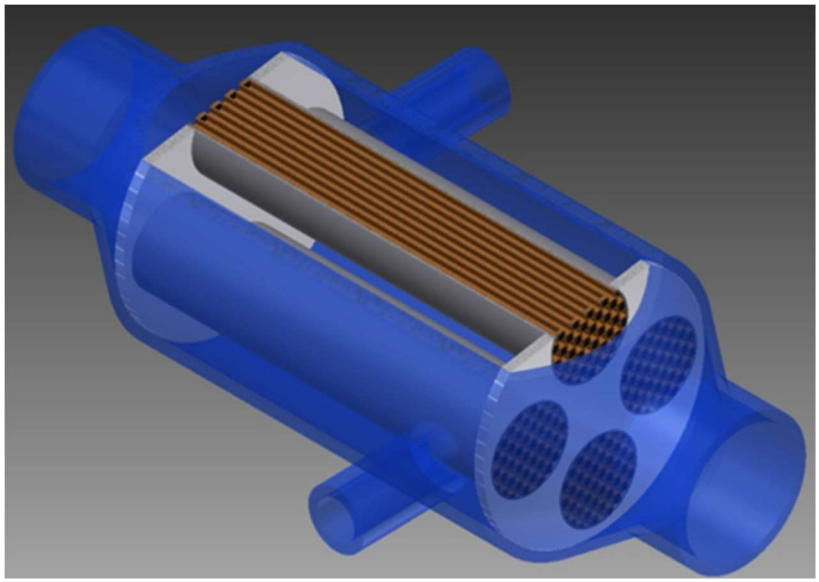

Figure 1.4: Rendering of a novel combined DPFHX [20].

Further opportunities exist in the inherent operation of a DPF, such as during regeneration. As discussed, regeneration techniques can include the late injection of additional fuel or externally heating the DPF in order to reach the required temperatures. Not only could the DPFHX recover the additional thermal energy from the high temperature regeneration process, penalties on the engine's efficiency from the additional energy input for external heating or fuel for late injection could be lessened. Moreover, an exhaust HEX also presents enhanced control opportunities to prevent excess temperatures in the DPF cores, mitigating potential damage from thermal stresses and cracking. Conceptually, the working fluid would stop circulating in the DPFHX until the DPF cores achieve regeneration temperatures. At this point the working fluid would begin circulating again to recover any excess heat from this regeneration while also preventing temperature runaway in the DPF cores. Possible extensions of the WHR system include utilization of a working fluid preheater (via a thermoelectric generator or the exhaust of the RC expander) to assist the DPFHX warmup during startup conditions and to help the DPFHX

achieve regeneration temperatures quicker, or implementing an electric heater powered by the RC during start-up conditions to pre-heat the exhaust for aftertreament [21, 22].

1.3 Scope of Work

Due to the potential of the DPFHX device, the subsequent chapters in this thesis describe the work completed investigating this aftertreatment option for CI engines. Previously, Sprouse [20] detailed the creation of a WHR apparatus for use with a Yanmar single-cylinder CI engine. This included experimental testing of the WHR apparatus along with computational modeling of the DPFHX [20]. Building on that prior effort, this thesis explains the work of the author in further investigating the DPFHX for WHR. This involved experimental testing of various working fluids both with and without DPF cores.

Before presenting the procedures and results of the experiments and simulations, Chapter 2 aims to provide a contextual overview of the RC WHR analysis including the state-of-the-art in the field. The chapter begins with a discussion of RC WHR configurations, components, working fluids, and the terms used to assess their performance; thereby, developing an analytical framework for the subsequent literature review. Following a historical summary of RC WHR from 1973 to 2011 is an exhaustive review of the literature from 2012 to the present. Subsequently, the trends of RC WHR spanning the past 40 years are succinctly summarized, highlighting the direction of the field and specific topics requiring consideration.

Next, the third chapter of this thesis covers the three rounds of experiments conducted: validating the performance of the WHR apparatus, assessing the performance of four working

fluids in the WHR apparatus, and testing the operation of the DPFHX. Overall, the results of each round will be discussed and compared where appropriate. Moreover, a thermal resistance analysis was completed to further elucidate the heat transfer mechanisms occurring within the DPFHX; hence, the methodology and results of this study are also included. Finally, through discussion and analysis of the experimental results, conclusions regarding operation of the DPFHX are presented based on the current apparatus and extrapolated to future research.

Finally, Chapter 4 presents a summary of the entire work. It is at this point that the trends seen in the literature review are linked with the experimental exercises completed, indicative of the relevance and importance of this work in the context of the current state-of-the-art. Furthermore, these linkages are expanded upon to indicate the direction of and motivation for the author's future undertakings. Thus, the efforts described in this thesis provide the background and validation for the continuation of research on the DPFHX concept, while also indicating specific aspects for enhancement based on the outcomes presented herein.

Chapter 2: RC WHR Literature Review

2.1 RC WHR Overview

Before delving into the state of the art of RC WHR, it is imperative to understand the fundamental aspects of RC WHR operation and analysis. First and foremost are the various configurations of cycles that are prevalently employed. The basic RC consists of an evaporator, expander, condenser, and pump in a single loop, as shown in Figure 2.1 [23]. When this, or any other configuration, utilizes engine exhaust gas as the heat source, it is commonly referred to as an RC bottoming cycle or mid-grade WHR [24]. Furthermore, if the engine coolant is used as the heat source, it is often referred to as low-grade WHR, a distinction made based on the temperature of the heat source used [17]. Although the coolant and exhaust are the primary sources of waste heat considered, additional energy sources employed include EGR, Charge Air Cooler (CAC), or general process waste heat in power plant applications.

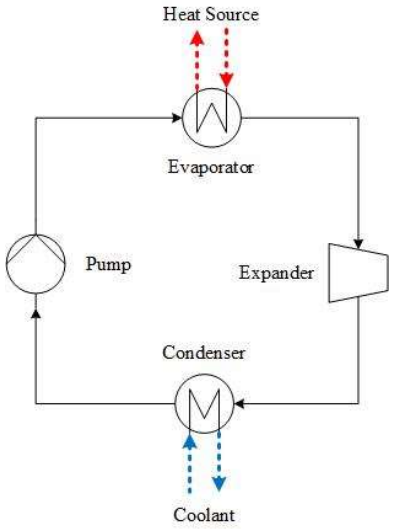

Figure 2.1: RC configuration highlighting the pump, evaporator, expander, and condenser.

In order to improve waste heat utilization, there are several modifications frequently made to the RC. For example, in a preheat RC (PRC) as in Figure 2.2a, an additional HEX is placed prior to the main evaporator to preheat the working fluid via a secondary heat source. Traditionally, this heat source for the preheater is the engine coolant, with the exhaust as the main heat source. Depending on the expander, the inclusion of preheat in the cycle can aid in vaporization of the working fluid, which can potentially prevent damage to the expander from liquid droplets in the working fluid stream, while also allowing for the utilization of additional waste heat sources [23, 25, 26].

An equally simplistic adaptation of the RC is the regenerative RC (RRC), in which an internal HEX is situated after the expander. This regenerative HEX captures residual heat from the working fluid after it passes through the expander, not only reducing the cooling load of the condenser, but also providing additional heat to the working fluid prior to the expander, similar to the preheater [27]. Figure 2.2b shows the most common RRC configuration, with the regenerator placed upstream, in series with the evaporator. However, placement of the regenerator can be further varied (i.e., placing the regenerator parallel to the evaporator). To additionally maximize waste heat utilization, both preheat and regeneration can be used in an RC (PRRC), shown in Figure 2.3. As in the PRC, the coolant is commonly used as the preheat source for the main exhaust heat source and as in the RRC, the location of the regenerator can be moved in relation to either the preheater or the evaporator.

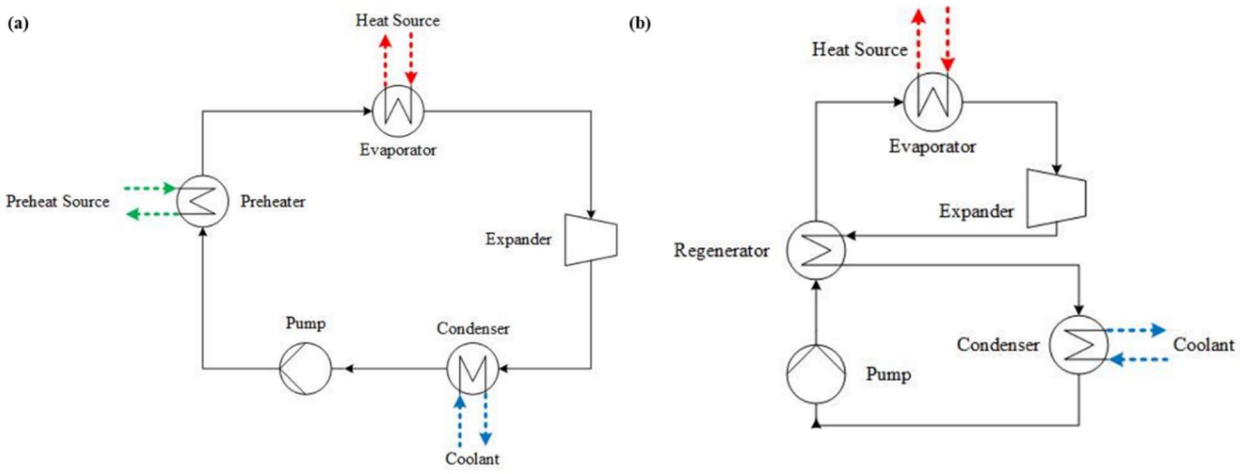

Figure 2.2: (a) PRC and (b) RRC configurations.

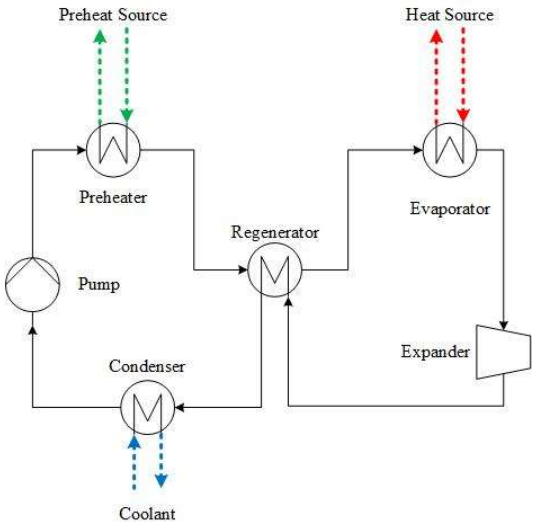

Figure 2.3: PRRC configuration.

In contrast to the previously mentioned single-loop RC modifications, cascade RCs (CRCs) and dual-loop RCs (DRCs) consist of two full RC loops. Specifically, for a CRC, the high-temperature (HT) loop is essentially a standard RC, but instead of transferring residual heat from the condenser to an external coolant, the residual heat of the HT loop is the heat source of the low-temperature (LT) loop, as shown in Figure 2.4. Comparatively, in a DRC as in Figure 2.5,

two different heat sources are used in the LT and HT loops, traditionally the coolant and the exhaust. In this way, multiple heat sources can be combined in a single WHR system with improvements in heat utilization and power output coming at the added expense of increased system complexity and supplementary components [27]. It is important to note that although the two loops in Figure 2.5 are completely separate RCs, the complexity can be increased using preheaters and regenerators, oftentimes connecting the two loops to form a cascade DRC. Ultimately, the configurations in Figure 2.1 through Figure 2.5 display basic set-ups for each cycle, with a large number of further variations and added complexities possible.

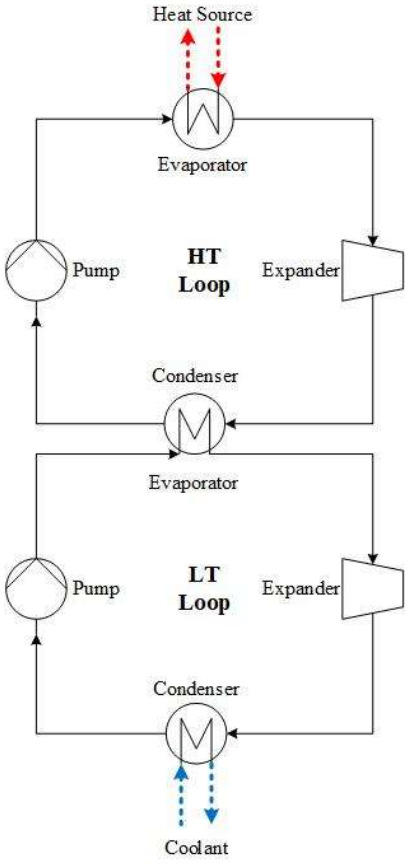

Figure 2.4: CRC configuration.

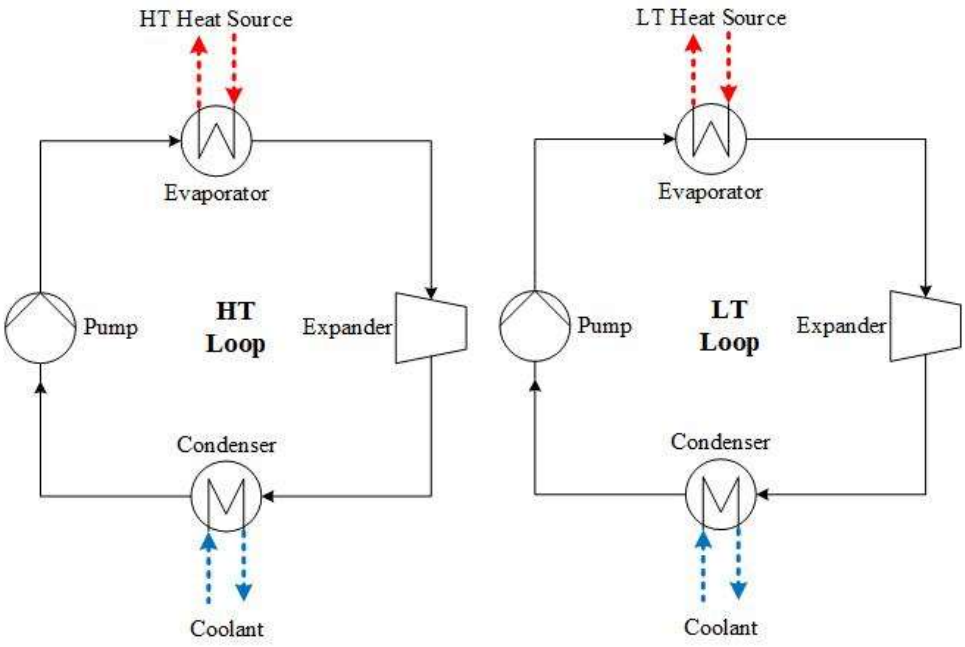

Figure 2.5: DRC configuration.

Traditionally, the analysis of RC WHR systems, either through experiments or models, is done by energy balances on individual components. Most simplistically, steady-state systems are used to calculate the work with isentropic efficiencies for the pump and the expander along with finding the heat transfer for both the condenser and evaporator. Thus, the net work output can be calculated as the difference between the work generated in the expander and the work consumed by the pump. Furthermore, the comparison of the heat transfer to the working fluid versus that from the heat source yields indications about the waste heat utilization of the system. Also indicative of system performance are the various efficiency values calculated. In addition to individual component efficiencies, thermal efficiency, system efficiency, and conversion efficiency are all used to characterize the efficacy of RC WHR. The thermal efficiency of the cycle is calculated as the ratio of net work over the absorbed energy from the heat source, evaluating how well the cycle transfers the recovered waste heat to power output. While the system efficiency is the ratio of net power to the maximum heat available in the heat source and

can often be combined with the engine or heat source efficiency to provide an overall efficiency. Finally, the conversion efficiency takes into consideration losses in converting the energy from the expander to usable energy for the system.

Although the efficiencies generally describe the system, there are also several analysis methods strictly applicable to HEXs, commonly used in the literature for optimization. The first of these is a pinch point analysis, in which the minimum temperature difference between the two streams in a HEX provides correlations for performance and surface area. The lower the pinch point temperature difference, the fewer losses within the HEX, but a larger heat transfer surface area is required. This indicates the tradeoffs between lower operating costs of heat sources with higher costs of larger HEXs, which can be targeted and optimized during RC WHR operation [28]. The second calculation method is the overall heat transfer coefficient, which takes into consideration the thermal resistances from conduction, convection, and fouling within a HEX [29]. Since this overall heat transfer coefficient also takes into account the cold or hot surface area within the HEX, this coefficient can be optimized to minimize the heat transfer surface area and subsequently the cost of the HEX.

Moreover, an economic analysis is just as crucial to the overall design of RC WHR systems as the thermodynamic performance metrics mentioned. While different authors utilize dissimilar methodologies for assessing the economic performance of a system (e.g., only considering working fluid performance [30], optimizing thermodynamic, economic, and environmental performance concurrently [31], etc.), there are several overarching terms used. One such expression is the levelized energy cost (LEC), which evaluates the energy cost per

kWh based on the net power output, capital recovery cost, total cost of equipment, and operation and maintenance costs over the evaluated period [32]. The total investment cost, primarily based on the cost of the components, and the electricity production cost (EPC), calculated similar to that of LEC, also evaluate economic performance [33]. Calculated from the average price of electricity and the depreciation of system components, the depreciated payback period (DPP) is used to quantify the long term costs associated with a WHR system [34]. These terms, among others, are used to assess and compare the economic performance of various working fluids, cycle configurations, or waste heat sources.

The final factor for consideration is the working fluid. When a working fluid is organic, the cycle is referred to in literature as an Organic Rankine cycle (ORC). For organic working fluids, which generally have lower boiling points and critical temperatures than inorganic fluids, the classification of wet, dry, or isentropic is also applied, based on the slope of the fluid's saturation curve [27]. However, in order to prevent damage to the expander from condensation and subsequently removing the need for superheating, dry and isentropic fluids, such as hydrocarbons and refrigerants, are preferred [35]. Additional criteria imperative to working fluid selection include thermal and chemical stability, low cost, environmental impact, safety, high latent heat of vaporization, density, specific heat, and general heat transfer properties (i.e., low viscosity, high thermal conductivity) [17].

Based on cycle configuration, efficiencies, RC performance, economic performance, and working fluid selection, the efficacy of RC WHR systems for various applications can be assessed. Moreover, via multiple difference facets of RC design, the performance of these

systems can be optimized. Thus, this introductory overview frames these types of assessments carried out in the literature.

2.2 Literature Review

From 2010 to 2016, the number of publications on the topic of RC increased by nearly 400% after remaining steady from 2000 to 2010, indicating the growing interest in RCs for various applications across the globe [36]. However, conducting innovative and thorough research requires a wide literature search to understand the current state-of-the-art. The work of Sprouse [20] comprehensively reviewed WHR and RCs through 2011, including power cycle comparisons, WHR applications, component and working fluid selection, experimental/simulated performance, and economic approximations. Thus, after summarizing the state-of-the-art as of 2011, the current literature review will assess RCs for engine WHR between 2012 and 2018 to fully cover the growth in this research area.

2.2.1 Early Literature Review Summary (1973-2011)

The study of WHR began as early as the 1970s in an attempt to mitigate increasing fuel prices and growing concern over air pollution driven by the Clean Air Act. As fuel prices fluctuated through the years, so did interest in WHR methods, with publications dwindling in the late 1980s before picking up again in the mid-1990s and dramatically increasing in the mid-2000s. The first two instances of Rankine cycles for automotive WHR occurred in 1973 and 1976, respectively. In 1973, Morgan et al. developed a model and prototype RC for WHR using a 1972 Ford Galaxie for component sizing, indicating the potential for 11% fuel economy

improvement [37]. Furthermore, in 1976, Patel et al. installed an RC system on the exhaust of a Mack 676 diesel engine for a long-haul truck, yielding a 15% fuel economy improvement and a 13% increase in maximum power output [38].

From these benchmark studies, many researchers went on to compare other WHR methods to RCs, including Brayton cycles (BCs), Kalina cycles, Stirling engines, and gas turbine systems. However, even in the cases where the other cycles outperform the RC (e.g., the Kalina cycle in [39]), the simplicity and cost-effectiveness of the RC made it the more viable option. Furthermore, different heat sources for RC WHR were studied modestly, with researchers indicating that maximum heat recovery occurred when the exhaust and the coolant were used together [40, 41]. However, the exhaust gas alone was also utilized in the literature with success [42, 43], further improved by coupling the exhaust gas with the heat of the engine block [44]. Notably, Oomori et al. implemented the coolant as a heat source to negate the negative impact of exhaust heat fluctuations; thus, recovering 3% of the engine's output energy [45].

More so than cycle type or heat source comparisons, working fluids were largely considered in the performance optimization of WHR methods. Specifically, the working fluids used early in RC WHR were subsequently phased out due to environmental considerations with global warming potential (GWP) and ozone depletion potential (ODP) becoming increasingly important selection criteria. Additionally, thermal stability, capital and investment costs, system size, and performance were all imperative criteria for working fluid selection beyond the necessary thermo-physical properties.

Although Badr et al. developed specific correlations for working fluid thermo-physical properties in one paper; authors customarily provided general correlations for specific properties and WHR performance [46]. For example, higher boiling points and higher critical temperatures yielded improved performance [47-50]. Furthermore, refrigerants performed better with decreasing source temp, while wet fluids attained superior cycle efficiencies for increasing turbine inlet superheat [47, 51]. Since the optimal working fluid varied and no single working fluid was persistently regarded as superior, determination of the appropriate working fluid for a given application was considered of great importance across the literature. Nonetheless, water, benzene, and R-123 regularly displayed preeminence, necessitating their consideration for most RC WHR applications.

Rivaling in importance to working fluid selection was that of the expander. The efficiency of the expander, in conjunction with its coupling to energy conversion or storage technologies, affects overall cycle efficiencies, as well as the practicality of RC implementation. Turbines were the preferred expander for high temperature and power output situations, achieving high efficiencies, but requiring strict inlet working fluid conditions to prevent fouling. Thus, reciprocating expanders were widely applied in smaller systems, performing better at varying operating conditions and being more forgiving of inlet conditions. Also considered, though not as prevalent, were Wankel, screw, and scroll expanders, with their potential ability to outperform other types [52, 53]. Furthermore, aside from initial studies mechanically coupling the expander to the vehicle, hybridized vehicles or battery storage after energy conversion were extensively implemented as the field progressed.

Throughout the field, primary applications of WHR included on-board vehicle systems for spark-ignition (SI) and hybridized electric passenger vehicles, CI passenger vehicles, and CI HD long-haul trucks. As such, appropriate component sizing and the integral corollary, determination of working fluid selection, targeted minimization, as well as integration within existing vehicle components. Moreover, similar trends were displayed for economic concerns in system design, with cost becoming considerably larger for working fluids and components as system size increased. Furthermore, despite the cost of an RC system decaying dramatically as the power output grows, the economic optimization of operation is rarely the same as thermodynamic optimization [50, 54]. Hence, a compromise between economics and performance, including the previously discussed considerations (e.g., working fluids, components, and sizing) must be holistically targeted during RC design.

Notwithstanding the design and optimization challenges facing RC WHR, modeling and experimental thermal efficiency improvements from 2-30% were achieved in the literature prior to 2012, with power output upgrades ranging from 10-20%. Additionally, fuel economy grew by 3-15%, with payback periods of around three years for several systems. Ultimately, the state of the art as of 2011 indicated the viability of RC WHR for enhancing the efficiency of internal combustion engines (ICEs). Furthermore, ameliorations in the RC systems themselves were achievable through effective working fluid and component selection and appropriate system sizing for the given application. With no single preferable RC system design developed, the trends in the literature stress the significance and weight that each constituent carries, as well as the need for further refinement and advancements in technology for WHR applications.

2.2.2 Recent Literature Review (2012-2018)

In 2012, Boretti modeled an RC for WHR using a four-cylinder turbocharged 1.6 L gasoline passenger car engine in order to identify the most effective heat source with R245fa as the working fluid [55]. Furthermore, to eliminate the complication of transferring energy from the expander to the vehicle's crankshaft, Boretti recommended installing the RC configuration on-board a hybridized vehicle. Ignoring additional losses such as conversion efficiencies, usable power versus fuel energy flow rate improvements of 3.4%, 1.7%, and 5.1% were found for exhaust, coolant, and combined exhaust and coolant WHR, respectively. Moreover, despite providing a lower improvement in usable power versus. fuel energy flow rate than the other heat sources, WHR utilizing the coolant was a competitive heat source, since the coolant back pressure reduces the engine's thermal efficiency less than the exhaust back pressure.

In the same year, Shu et al. theoretically analyzed the performance of a combined thermoelectric-generator (TEG) with an RC (TEG-RC) system for exhaust gas waste heat recovery in which the TEG and the coolant preheat R123 with an additional, conditional preheating occurring when the cycle was subcritical [21]. Moreover, the most effective operation of the combined TEG-RC system occurred at an evaporator pressure of 4 MPa and a condenser pressure of 0.06 MPa, yielding 28 kW of additional power and an improvement of nearly 5% in the indicated thermal efficiency. Although the TEG produced only 6% of the power of the RC system, the TEG allowed for a wider range of RC operation, with improvements in technology and performance crucial for practical application.

Additionally at the same time, Latz et al. theoretically compared pure and zeotropic mixture working fluids in both supercritical and subcritical Rankine cycles for WHR on HD CI engines from the exhaust, coolant, and through the EGR system [56]. Of the seven pure working fluids, ethanol was superior in a subcritical cycle and HCFC-123 performed best in a supercritical cycle. Moreover, R430a and a mixture of water and methanol were the top achieving zeotropic working fluids in supercritical and subcritical cycles, respectively. From both types of working fluids, the supercritical cycle provided no significant thermal efficiency benefits at a costly higher pressure; thus, the water/methanol mixture in a subcritical cycle was deemed the most promising working fluid.

Instead of investigating different working fluids, Arunachalam et al. in 2012 conducted a theoretical evaluation of RC WHR from five different heat source combinations on a 13 L HD CI engine in a dual loop cycle [57]. Using IPSEpro with water as the working fluid, the power available from each source at the primary operating point of the C75 European Stationary Cycle (ESC) and a sweep of operating points was compared. Overall, the authors obtained the highest power output from the dual loop cycle utilizing EGR, exhaust gas, and the CAC; however, the EGR alone proved to have a higher heat utilization efficiency (22.2% versus 15.6%). For the loading sweep, employing just the EGR achieved comparable power output to the three combined sources at 25-50% load (typical for HD operation). Therefore, while the ideal source for WHR depends greatly on the engine load, the EGR system by itself demonstrated improved consistency, while minimizing cost and size.

Following the recommendations from their previous study, Boretti et al. (in the same year) researched the implementation of an RC WHR cycle with water as a working fluid on a gasoline engine fitted with a parallel hybrid powertrain for cold start driving cycles [58]. While the parallel hybrid system incurred conversion penalties, it also allowed the WHR energy to be directly utilized on-board the vehicle. Overall, considering thermal, electrical, and transmission losses, the authors achieved 10.2% additional fuel economy savings on the parallel hybrid over a traditional powertrain.

Concurrently, Lopes et al. thoroughly reviewed the state of the art of RCs for WHR via hybrid engines, investigating cycle components and literature trends [59]. Specifically, shell-and-tube, plate, and metal foam HEXs were all used for RC applications, yet plate HEXs were the ideal option due to their compact design. Furthermore, five different types of expanders were typically used; nonetheless, the scroll expander was the most prevalent with the highest efficiencies. Of the three main pump types, the operation of diaphragm pumps most appropriately met the needs of an RC. Accordingly, the authors emphasized the importance of component sizing and working fluid selection specific to the application.

Also in 2012, Dolz et al. studied RC working fluids and WHR heat sources for a HD CI engine in order to achieve maximum power output [60]. Comparing working fluids, all energy sources leaving the 12.0 L two-stage engine (i.e., exhaust gas, EGR cooler, intercooler, aftercooler, and engine block cooling water) were used in a single RC. From this, water performed better in HT cycles with superheating, while R245fa functioned better in LT cycles. Subsequent simulations included two heat source configurations with water as a working fluid:

only HT heat sources (i.e., exhaust, EGR, aftercooler) and a binary cycle using a top cycle (i.e., EGR, exhaust) and a bottom cycle (i.e., aftercooler, intercooler, cooling water, cooled exhaust gases). Consequently, the binary cycle achieved the highest power improvement of 19% over the baseline engine, followed by the HT cycle, and then the single cycle with all heat sources, at 14.7% and 10%, respectively.

Continuing the previous study by Dolz et al., Serrano et al. adapted the RC WHR system to resolve issues when coupling the RC to the engine, namely, by removing the low-pressure turbine [61]. Moreover, they modified the RC with the following heat sources: mid-pressure (MP) EGR, low-pressure (LP) EGR, and LP EGR with additional HT sources (i.e., exhaust gases, aftercooler). Specifically, compared to the standalone engine, they achieved RC power improvements of 6.4% and 7.7% for the MP EGR and LP EGR, respectively, and power degradation of 6.8% for the LP EGR/HT. Thus, when compared to the power improvements from Dolz et al., the reduced pumping losses from removing the LP turbine were inadequate to improve RC performance. Although the best performing RC configuration was the binary cycle from Dolz et al., it incurred additional complexity using every available source; thus, Dolz et al.'s HT heat source configuration utilizing the exhaust, EGR, and aftercooler was the most promising.

Boretti followed up their work in the same year by modeling an RC WHR using the coolant and the exhaust of a hybrid gasoline vehicle; however, this time employing R245fa as the working fluid [62]. Experimentally obtained engine operating parameters permitted steady-state simulation of an RC using exhaust, coolant, or the two heat sources combined for WHR. Overall,

these options increased the average and maximum fuel efficiency by the following amounts: 3.4% and 6.4% (exhaust); 1.7% and 2.8% (coolant); 5.1% and 8.2% (combined), without consideration of losses.

As a different approach, in 2012 Tian et al. analyzed the thermo-economic performance of twenty working fluids in an RC WHR system, using the exhaust gas from a six-cylinder, supercharged CI engine [30]. Three working fluids exhibited superior behavior across all the parameters optimized, R141b, R123, and R245fa, with thermal efficiency values ranging from 13.3 to 16.6%, net power from 49 to 60 kJ/kg, expansion ratios from 18 to 41, and ratios of total heat transfer area to net power output from 0.436 to 0.572 m^2/kW. Furthermore, R141b, R123, and R245fa achieved electricity production costs of 0.30 to 0.35 $/kWh, indicating their economic capabilities, in addition to their thermal capabilities.

The same year, Boretti again modeled an RC WHR system, but this time on a direct injected engine running on ethanol over the New European Driving Cycle (NEDC) startup and highway conditions [63]. This RC system consisted of exhaust gas as a heat source with the coolant as a preheater, R245fa as the working fluid, and an electrically operated pump. The simulation obtained fuel efficiency increases of 4.2% over NEDC with a faster engine warm-up and 6.4% over highway conditions. Further fuel efficiency improvements are possible by considering reductions in the cold start penalty along with enhancements provided by a hybrid powertrain (i.e., regenerative braking, engine start/stop, and the mixture of the thermal and electric power supplies).

The following year, Xie et al. simulated on-road RC WHR performance for a HD CI engine using the exhaust and cooling water as heat sources and R123 as the working fluid [64]. The simulation was based on four different driving modes: start-up, turbine turning at no-load, power, and protection implementing turbine bypasses when needed (e.g., when the working fluid cannot evaporate). However, on-road system efficiencies of the RC were as low as 3.63%, largely due to the variability of switching modes and the turbine bypassing required; hence, this creates significant opportunities for improvement.

Also in 2013, Shu et al. evaluated the full installation of an RC WHR on a CI engine, using three plate HEXs to recover exhaust gas waste heat via a thermal oil circuit with a jacket water pre-heater [65]. Based on engine test data for two operating points, the cycle was simulated using R245fa and R601a as the working fluids. The maximum expansion power was 12.4 kW for R245fa under the first operating condition versus 18.8 kW for R601a under the second operating condition, ultimately providing an enhancement of 9.0% and 7.7% for thermal efficiency, respectively.

In the same year, Tian et al. expanded the traditional application of an RC for WHR on a CI engine by employing the power output of the RC as the input for a compression refrigeration cycle in four configurations as shown in Figure 2.6: standard, with an expander to recover the throttling power, with an internal HEX to preheat/cool the working fluid at the HEX (HEX) inlet/turbine outlet, and with both an expander and an internal HEX [66]. Based on the simulations with CO_2 as the working fluid, the inclusion of both the expander and the internal HEX in the provided improved system performance, due to the expander lowering the

compression refrigeration cycle high pressure and the internal HEX growing the expansion power. Moreover, they state that targeted high pressure values can further optimize performance.

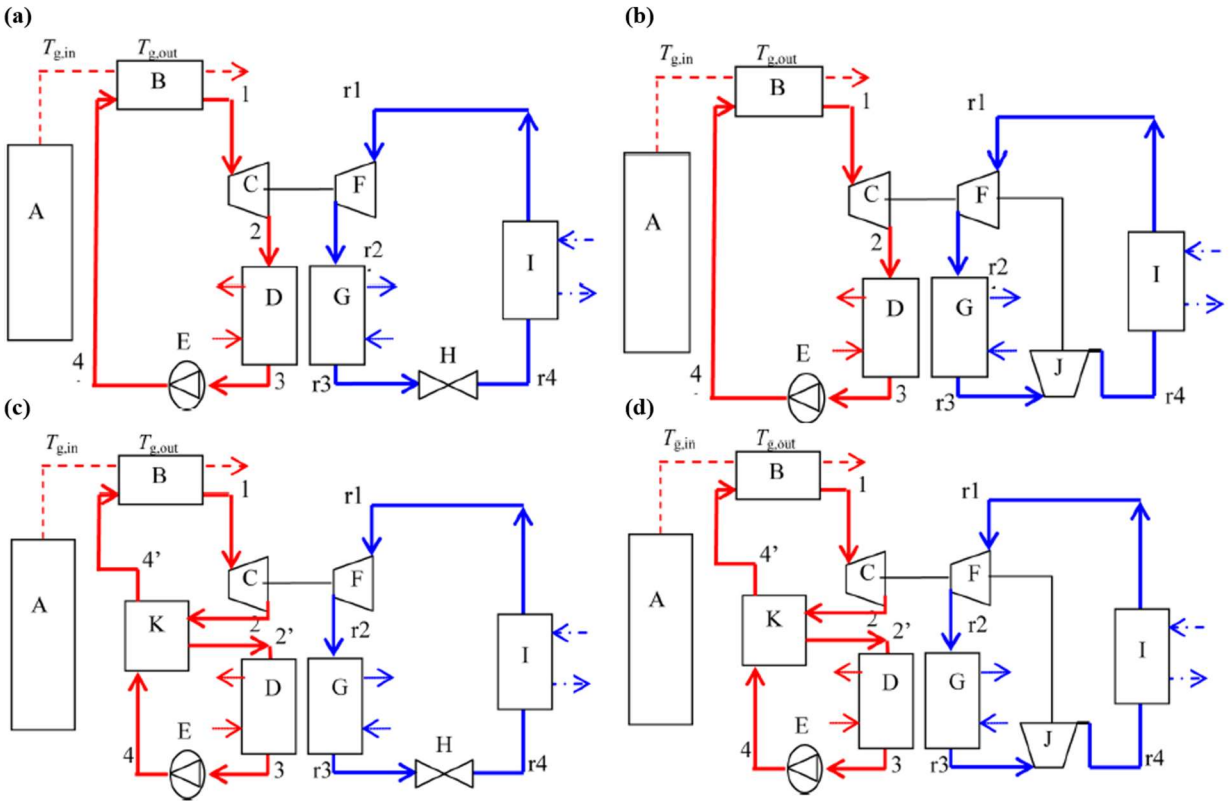

Figure 2.6: Diagrams of the combined RC-compression refrigeration cycle with (a) no modifications, (b) an expander, (c) an internal HEX, and (d) both an expander and an internal HEX [66].

Contrary to most previous WHR vehicle applications employed using parallel hybrids, in 2013 Jung et al. introduced an RC WHR system on a series hybrid electric intra-city bus with a compressed natural gas (CNG) engine [67]. Two working fluids, water and R245fa, and two HEX surface types, 10.27T and 30.33T, were compared in a quasi-one-dimensional (1-D) simulation. Ultimately, the combination of R245fa and 30.33T provided the greatest overall improvement of fuel consumption at 8%, while maintaining power output across the operating

conditions of a typical bus route. Moreover, the engine and drivetrain in series allowed the engine with the RC to meet the same power loads while maintaining a reduced fuel consumption.

The same year, Yamaguchi et al. used the exhaust heat of a single cylinder, high boosted, high EGR CI engine as the simulated input for an RC WHR system using water after comparing six potential working fluids [68]. Based on the available exhaust energy, coupled with their simulation results, the authors determined that medium to high driving loads (e.g., highway operation) were prime for RC operation, achieving an improvement in brake specific fuel consumption (BSFC) of 2.6-3.0% for full load conditions.

Concurrently, Hossain et al. investigated the ability of two shell-and-tube HEXs to extract exhaust energy on a four-cylinder test engine with water as a working fluid [69]. After achieving a maximum HEX effectiveness value of 0.55 and a maximum combined RC and engine efficiency increase of 4.4% in their experimental set-up, the authors developed three dimensional (3-D) CFD models using ANSYS CFX to optimize the HEX design. Based on the optimized HEX design parameters (19 tubes, inner tube diameter of 76 mm, length of 2 m), the counterflow orientation recovered heat more effectively than parallel flow, attaining 23.7% additional power for an optimized working pressure of 30 bar.

Also in 2013, Xu et al. developed a holistic approach to comparing different cycles for use in exhaust WHR through the generation of three new efficiency terms: energy recovery efficiency, energy conversion efficiency, and overall energy conversion efficiency (OECE) [24]. Using these terms, the authors compared six different bottoming cycles to determine which one would provide the maximum OECE: the Brayton air cycle with isothermal compression. However, due

to the difficulties involved in the implementation of isothermal compression, the superheated and standard Rankine cycles were subsequently the best performing WHR bottoming cycles.

Furthermore, Domingues et al. continued the analysis in 2013 by creating an RC and a HEX model for the application of WHR from the exhaust gases of a 2.78 L SI engine, while additionally comparing thermal and vehicle mechanical efficiencies of water, R123, and R245fa as the working fluids [70]. Specifically, these models revealed water as the ideal working fluid, with R123 and R245fa as being more effective for LT WHR. Moreover, upon comparing HEX design, the ideal HEX (i.e., set model evaporating pressures) obtained maximum improvements of 3.52% and 15.95% for ICE thermal and vehicle mechanical efficiencies, respectively; whereas, full simulations of shell-and-tube HEXs obtained maximums of only 1.2% and 6.96%. However, the authors noted a coupled increase in evaporation pressure with thermal and mechanical efficiencies, indicating the importance of evaporator and expander designs.

Continuing a busy year, Zhu et al. presented a theoretical energy and exergy study of a bottoming RC WHR using five different working fluids and a wide range of engine operating conditions [71]. Subsequently, the most important parameters influencing RC performance were working fluid properties, superheating temperatures, and evaporating pressures. Furthermore, the superheat temperatures and evaporating pressures greatly depended on working fluid properties subsequently influencing component sizing. Of the working fluids, ethanol and R113 achieved maximum recovery efficiencies across the operating conditions employed. However, at heat source temperatures above 800 K, water performed better. Despite the comparatively poor

thermodynamic performance of R245fa, its environmental safety makes it extremely attractive for low-grade WHR.

The same year, Peris et al. simulated and compared six different RC configurations with ten distinct working fluids for RC WHR using engine cooling water [27]. The six RC configurations were as follows: basic, regenerative, double regenerative, reheat regenerative, ejector, and transcritical regenerative. Consequently, the most efficient WHR occurred in the double regenerative RC configuration with SES36 as a working fluid, improving the ICE electrical efficiency up to 5.3%. However, the double regenerative configuration is quite complex, and the other configurations provided similar system improvements with fewer alterations. In particular, the regenerative configuration with R236fa or the reheat regenerative configurations with R134a both provided similar improvements in the ICE electrical efficiency with simpler structures.

Hajabdollahi et al. completed a thermodynamic, economic, and environmental optimization of an RC system in 2013 for CI WHR, targeting the maximum thermal efficiency and minimum total annual cost for working fluids [31]. Accordingly, the best economic and thermodynamic working fluid was R123 with a thermal efficiency of 51.27% and a total annual cost of $86,253 per year. Notably, R245fa performed closely to R123, achieving a thermal efficiency and total annual cost less than R123 of 1.01% and 0.01%, respectively.

In the same year, Shu et al. examined four different DRCs for WHR: basic, HT regeneration, LT regeneration, and both HT and LT regeneration [72]. Within the HT loop, several cycle modes and working fluid combinations were compared: subcritical with water, subcritical with siloxane, and transcritical with siloxane, while the LT loop operation and working fluid (R143a)

remained constant. Subsequently, the basic DRC with a subcritical water HT loop provided the highest performance, with a maximum net power output of 39.67 kW and a conversion efficiency of 11.93%.

With the DRC performing best, Shu et al. focused the next year on its simulation for WHR from a six-cylinder turbocharged CI engine, while comparing the performance of six working fluids in the LT loop with water employed in the HT loop [73]. The heat source of the HT loop was the high-temperature exhaust, while the heat sources of the LT loop were the engine coolant, the residual heat of the HT loop, and low-temperature exhaust in series. Subsequently, through the optimization of the HT and LT evaporation temperatures, the results indicated that at high operating loads, R1234yf was the most suitable working fluid, obtaining maximum power and exergy efficiencies of 36.77 kW and 55.05%, respectively. However, maximum thermal efficiencies were obtained by R600 (20.07%) and R245fa (20.06%). Regardless of the load, R124 yielded the worst performance.

In the same year, Zhang et al. theoretically surveyed the performance implications of a combined TEG and DRC system for exhaust WHR [74]. The DRC consisted of a HT loop with toluene as the working fluid and a LT loop with R123 as the working fluid. Subsequently, a combined thermal efficiency improvement of 5.2% was achieved; however, the authors concluded that the overall performance improvements of the combined system were not worthwhile considering the additional operational attention and costs incurred.

Also in 2014, Yang et al. assessed the performance of a RC for exhaust energy recovery under driving conditions using a model of a HD CI bus with R123 as the working fluid [75]. The

authors achieved system efficiencies of 3.63% for actual driving cycles, in contrast to 7.77% under the rated operating condition; thus, displaying a significant variation in performance during driving cycles. Comparing control strategies for optimal RC performance elucidated the superiority of a combined control strategy through the rated efficiency, effective operating range, and dynamic control.

Based on the HEX optimization efforts from previous studies, Bari et al. conducted working fluid and load investigations in 2014 for RC WHR from CI engine exhaust [76]. Using ANSYS CFX modeling software, the authors compared ammonia and water as the working fluids under full and partially loaded conditions for two optimally designed HEXs. At full load, water produced a higher power generation at lower working pressures; whereas, ammonia achieved the opposite trend. Consequently, water managed the highest power recovery at full load and outperformed ammonia down to 70% load, despite the higher engine backpressure imposed. Conversely, below 70% load ammonia outperformed water as the working fluid.

The same year, Furukawa et al. designed and tested an RC system for WHR from a HD CI truck [77]. Subsequently, the authors optimized the system efficiency by increasing the saturation temperature difference via HEX optimization and a high pressure turbine, with further improvements from the installation of a turbine energy recuperator. Consequently, upon selection of HFE as the working fluid, the authors attained a 7.5% fuel economy improvement using the exhaust gas, EGR species, and engine coolant as heat sources in comparison to only 3.8% for the engine coolant and EGR species; subsequently, corresponding to a fuel savings of 27% for the truck studied.

Concurrently, Dickson et al. utilized CFD simulations to optimize the design of the condenser for WHR on the Cummins-Peterbilt SuperTruck [78]. Through several design iterations, a condenser placed with the CAC, air conditioner condenser, and the radiator in the front grill of the SuperTruck was developed under the A75 operating condition with R134a as the RC working fluid. After successful thermodynamic and aerodynamic validation, the WHR system achieved fuel economy benefits ranging from 4-5%.

Also in 2014, Jin et al. explored the performance of a two-phase, finned-tube, counterflow evaporator with R245fa in an RC WHR system for a CI engine across different engine loads and speeds [79]. The overall heat transfer increased with greater engine power, with the R245fa mass flow rate additionally growing linearly. Furthermore, in cases where the pressures at the inlet and outlet of the turbine were constant, increasing the working fluid mass flow rate enhanced the turbine output. As the engine speed grew, the efficiency of the evaporator decreased. Finally, the area of the preheated and two-phase zone areas enlarged and shrank, respectively, with increasing speed or load.

As a slight deviation to traditional RC implementation in 2014, Han et al. studied the influence of cylinder clearance on the performance of an RC system with a free piston (FP) as the expander since FPs employ simpler structures, fewer moving parts, and lower mechanical losses than traditional rotational turbines [80]. Conversely, they experienced frictional losses between the cylinder and the piston, degrading their work output. Thus, in an effort to reduce frictional losses, the authors modeled the performance of a FP in an RC system with R245ca as a working fluid as shown in Figure 2.7. From a clearance of 0.00001 mm to 0.3 mm, the work

output gradually increased, and drastically decreased at clearances larger than 0.3 mm. As such, at a 0.3 mm clearance the net work output increased 10% presenting validation for performance improvements using FP expanders.

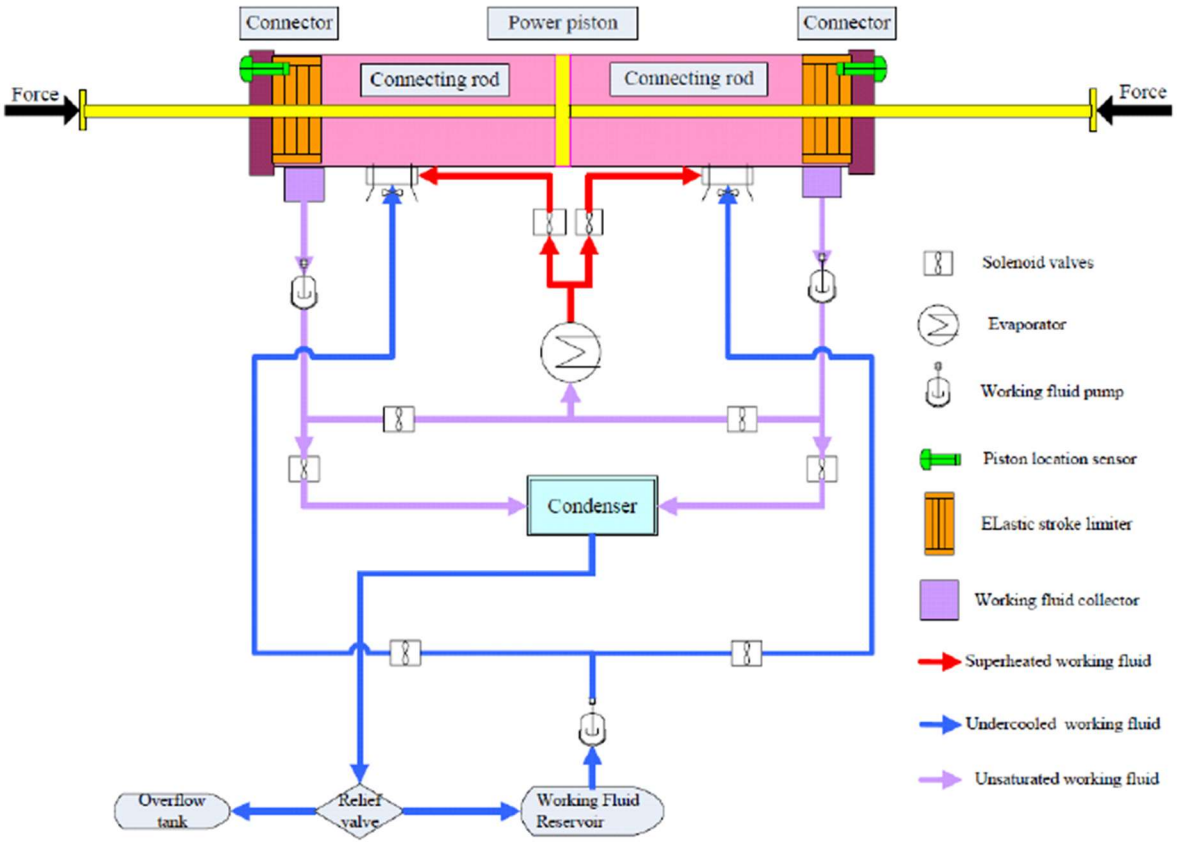

Figure 2.7: Configuration of an FP RC system [80].

In the same year, due to the importance of suitable HEX designs on the efficiency of WHR systems, Hatami et al. reviewed WHR from CI engine exhaust [81]. The different WHR techniques included in the review were RCs, TEGs, EGR systems, and turbocharging. To increase the level of heat transfer, fins performed better than porous materials or foams, yielding lower pressure drops, while shell-and-tube HEXs were most widely used in the literature. The identified design pathways for increasing heat transfer include working fluid and material selection, parallel HEXs, and installing TEGs downstream.

Also in 2014, Yue et al. modeled a CI engine and bottoming RC system with R123 as the working fluid based on experimental data using two modeling approaches [82]. Their cascaded model calculated RC performance based on the results of the ICE model; while their integrated model evaluated the performance of the RC system with the influence of the RC on the ICE included. The cascaded model achieved an overall thermal efficiency improvement of 13.4% when compared to the standalone ICE; whereas, the integrated model achieved an overall thermal efficiency improvement of 7.8%, more indicative of actual performance due to the included pressure drop. Although the RC provided an overall efficiency improvement, the ICE efficiency decreased by 2% because of the restriction in the exhaust.

Continuing a busy year, Long et al. inspected working fluid selection based on internal and external exergy of an RC WHR system using a set heat source [83]. The authors' analysis indicated that the evaporation temperature largely determines the internal exergy efficiency instead of the working fluid's thermo-physical properties. Conversely, the external exergy efficiency varied because of the evaporation temperature and thermo-physical properties, namely the Jacob number. As such, R600a achieved the greatest exergy efficiencies at larger heat source temperatures. Analysis of the overall exergy efficiency indicated the exergy and heat transfer processes (i.e., evaporator design and temperature) dictated the overall exergy transfer behavior in the RC system.

At the same time, Zhang et al. generated an experimental RC system using a single-screw expander, a spiral-tube evaporator, a multi-channel parallel condenser, and R123 as a working fluid for CI exhaust WHR [84]. At low to medium rotational speeds, the single-screw expander

achieved a maximum power output of 10.38 kW and a shaft efficiency of 57.88%; thus, indicating the applicability of the expander. Moreover, the authors found that RC performance was influenced by the engine power and the torque of the expander, achieving a maximum RC efficiency of 6.48% at 250 kW of output and 64.43 N·m of torque for an overall system efficiency of 43.8%.

Similar efforts by Yang et al. considered the performance of a DRC system for a six-cylinder CI engine using R245fa as the working fluid in 2014 [85]. The HT loop utilized the exhaust as the waste heat source; conversely, the LT loop employed the coolant and the intercooler as heat sources. At the engine rated condition, the effective thermal efficiency of the combined engine and RC system grew by 13% for an overall efficiency of 35%. Moreover, at medium to high loads, the BSFC decreased by 4%. Generally, the LT loop yielded a higher power output than the HT loop, but also a higher exergy destruction rate. Over the entire operating range modeled, the DRC achieved a WHR efficiency of 5.4%.

Concluding the studies in 2014, Hou et al. developed a generalized minimum variance (GMV) controller in order to regulate the operation of an RC WHR system with R245fa as the working fluid [86]. Two hallmark features of the proposed GMV controller were that it was data driven (i.e., no mathematical model) and it allowed for variations and disturbances in the tracked set-points. Applying the controller to a 100 kW RC system displayed that the multivariable RC system could handle variations in operating conditions while rejecting disturbances from noise. Furthermore, when compared to traditional proportional-integral-derivative controllers it displayed superior performance in tracking set-points and filtering out disturbances.

In 2015, Muhammad et al. designed, simulated, and then experimentally tested an RC WHR system consisting of a scroll-type expander coupled to an electric generator and a screw pump while utilizing the waste heat from steam and employing R245fa as the working fluid [87]. From the experimental setup, the authors obtained a maximum electric output of 1.016 kW and a net electric output of 0.838 kW, subsequently achieving a thermal efficiency of 5.64%, net efficiency of 4.66%, and isentropic expander efficiency of 58.3% at the maximum power output operating point. Overall, the largest losses in their system occurred in the pump and expander, as well as the in the piping systems.

Meanwhile, Galindo et al. experimentally validated an RC system with a swash-plate expander and ethanol as the working fluid for a turbocharged gasoline engine [88]. System energy balances yielded maximum ICE mechanical efficiency improvements of 3.7% at high loads and a cycle efficiency of 6%. Subsequently, maximum values of the isentropic and volumetric efficiencies of the expander were 38.5% and 38.2%, respectively.

Also in 2015, Yang conducted thermal and economic analyses of a transcritical RC (TRC) with R123yf as the working fluid for a marine CI engine [32]. Three different combinations of heat sources were compared: exhaust gas, exhaust gas and cylinder cooling water, and exhaust gas, cylinder cooling water, and scavenge air cooling water. The exhaust gas alone achieved the lowest total energy cost per kilowatt hour; conversely, all three sources combined exhibited the highest recovery efficiency, thermal efficiency, and specific work, but poor net power output and heat energy absorbed. However, the exhaust gas option exhibited the shortest payback period, the highest CO_2 reduction, and the largest savings of heavy CI oil. Thus, use of the exhaust

demonstrated optimal combined economic and thermal performance as a heat source for a TRC on a marine CI engine.

Feng et al., in the same year, addressed the thermo-economic, multi-objective optimization of an RC with a set heat source for WHR comparing pure and mixed R245fa and R227ea [89]. Consequently, the simulation results indicated that the performance of mixed or pure working fluids depended on the operational parameters, as well as the mixture mass fraction when present. Furthermore, maximum exergy efficiency and LEC were found for a mixture of 0.7 R245fa/0.3 R227ea. Moreover, mixtures perform better than pure working fluids for a majority of their models.

Also in 2015, Baldi et al. contrasted the optimization of an RC system on a chemical tanker with two CI engines installed at either 100% loading, 100% and 50% loading, over an operational profile from 50-100% loading in 5% intervals, or an operational profile over a variable range, as well as working fluids [90]. Consequently, the partial load conditions provided substantial improvements in the yearly fuel consumption savings estimates, growing from 7.0% to 9.0%. Furthermore, cyclopentane and benzene achieved the lowest yearly fuel consumption. When the interaction between the CI engines and the RC system were included in part load optimization efforts, the fuel consumption savings estimate increased further to 10.0%.

Concurrently, Esposito et al. established a nonlinear control model for WHR on engine exhaust that predicted mass and energy flows through system components to allow for transient control and response of the RC system [91]. Furthermore, after validation via a simulation of an SI engine accelerating on the highway, the new control model yielded comparable net power

output throughout the transient operating profile to a traditional feed forward control; thus, they state that this established an improved transient control model.

The same year, Song et al. evaluated the performance of a DRC for WHR from a turbocharged CI engine in which the HT loop utilized water as the working fluid and engine exhaust as a heat source; whereas, the LT loop used the jacket cooling water and residual HT heat as heat sources while testing three working fluids (R123, R236fa, and R245fa) [92]. By varying the dryness fraction of the water in the HT loop, the authors employed wet steam expansion via a screw expander. Consequently, a dryness fraction of 0.2 yielded the maximum HT loop net power output at 54.5 kW. Interestingly, for the LT loop, the variation of working fluid also led to variations in pinch point locations and evaporation temperatures; thus, R236fa yielded the maximum power output of the LT loop at 60.6 kW at an evaporation temperature of 368 K. The combined optimized HT and LT loops generated a net power output of 115.1 kW, an 11.6% increase from the standalone engine power.

Additionally in 2015, Yamaguchi et al. completed a comprehensive analytical study of RC WHR on a HD CI engine with either a single-stage or a two-stage turbocharging system [93]. Based on their analysis, the single-stage system yielded 40.0-74.8 kW of available waste heat energy at high engine loading conditions; similarly, the two-stage system yielded 43.0-76.3 kW at the same engine loads. With the implementation of a WHR system, the effective work of the engine only improved by 1.5% and 1.4%, for the single- and two-stage configurations, respectively, translating to fuel economy improvements at highway conditions of 2.7% and 2.9%, correspondingly.

Analogously, Allouache et al. assayed the effect of various operating parameters on the performance of an RC WHR system for a 15 L CI engine in 2015 with R245fa as the working fluid [94]. Following validation of the simulation, the authors determined that the use of two straight-finned HEXs in parallel reduced the pumping losses substantially compared to a single HEX. Across a range of speeds and loads, the RC achieved a 5% increase in power output and obtained peak thermal efficiencies of 11%. Additionally, peak power output occurred for working fluid flow rates between 70 and 145% of the exhaust mass flow rate.

Meanwhile, Pradhan et al. investigated heat sources and working fluids for RC WHR from a HD CI engine using experimentally obtained engine operating points [22]. Moreover, R123, R245fa, and R134a with three heat sources (CAC, EGR, and post-SCR exhaust) were considered in the study. For all configurations, R123 and R245fa exhibited the best working fluid performance. Moreover, for all working fluids, the combination of the post-SCR exhaust and EGR system displayed the best outcomes. Correspondingly, R123 obtained a maximum cycle output of 24.6 kW in this configuration, as compared to 19.9 kW for R245fa. Following system performance conclusions, the authors investigated the use of the WHR system to achieve SCR reaction temperatures during start-up operation. While the authors' thermal analysis indicates that the preferred configuration generates enough power to accommodate the thermal needs of the SCR, further work must be done to actualize the premise.

In the same year, Shen et al. focused their RC WHR research on the influence of two- and three-phase evaporators along with the impact of R245fa flow rate on expander power [95]. Subsequently, the two- and three-phase evaporators experienced 50-60% overall heat exchange

ratios with the two-phase outperforming the three-phase option at low loads. Thus, the mass flow rate of the working fluid and the enthalpy difference across the expander increased the power output of the expander. Conclusively, for CI engines at low temperatures, the two-phase evaporator was deemed ideal, while the three-phase evaporator was better for HD gasoline engines. Finally, both configurations had a total RC cost under $500, with a return on investment in 2.52 years.

Eichler et al., also in 2015, presented a holistic approach to designing and optimizing an RC for CI engines [96]. Upon comparison of ethanol, toluene, and R245fa based on safety, isentropic process efficiency, and saturation, the best working fluid was determined to be ethanol. Moreover, exhaust gas and EGR were found to be the ideal heat sources based on the heat quality and ease of implementation. Finally, heavy-duty and medium-duty engines were analyzed for WHR based on the comprehensive methodology, consequently obtaining the best overall performance from a heavy-duty SCR-only system (no EGR), yielding fuel consumption savings of 3% under real driving conditions.

Concurrently, Kulkarni et al. examined a DRC system for a HD ICE in which the LT loop with R245fa acts as the preheater for the HT loop with R236fa [97]. Consequently, the authors developed a MATLAB model of the RC system, achieving thermal efficiencies of 7.42% and 6.48% for the HT and LT loops, respectively, and a maximum work output of 14.16 kW at full load and speed, corresponding to a thermal efficiency improvement of 10.3%. Furthermore, increasing the evaporator pressure, decreasing the condenser pressure, or superheating the turbine inlet temperature all grew the RC system efficiency.

Meanwhile, Kölsch et al. assessed the performance of methanol, toluene, and SES36 as working fluids in an RC for WHR from CI engine exhaust [98]. While toluene exhibited higher net power output, methanol attained greater thermal efficiencies and smaller heat transfer areas, while SES36 performed the worst. Furthermore, by balancing between heat transfer area, thermal efficiency, and power, methanol with a pressure of 18 bar and a turbine inlet temperature of 320^{o}C yielded a desirable heat transfer performance.

Also in 2015, Amicabile et al. optimized the performance of an RC WHR system for a CI engine through the variation of heat source, working fluid, and thermodynamic cycle [99]. Upon evaluation of the available energy, the EGR cooler was the most appropriate waste heat source, with ethanol, pentane, and R245fa considered as working fluids in (1) a subcritical cycle with and without a recuperator and (2) a supercritical cycle with and without a recuperator. Of the twelve combinations, the subcritical cycle with a recuperator and ethanol as the working fluid yielded enhanced performance, improving the BSFC by 3.3%. Although the supercritical cycle with a recuperator and pentane as the working fluid displayed the highest power, the lower economic impact of the regenerative ethanol cycle was more attractive with a payback time of 3.43 years for a capital cost of $14,162.

Again in 2015, to mitigate the flammability concerns of hydrocarbons, Song et al. explored the performance of hydrocarbons mixed with retardants as working fluids in an RC WHR system employing the exhaust gas and cooling jacket water (preheat) for CI engines [100]. From the pure hydrocarbons, cyclohexane exhibited the maximum net power output of 78.3 kW. Then, cyclohexane was combined with two different retardants, R141b and R11, which, in addition to

reducing flammability, also reduced exergy losses subsequently improving exergy efficiency. Consequently, a 50% by volume mixture (50/50) of cyclohexane and R141b produced the highest net power output of 88.7 kW, a 13.3% increase over the pure cyclohexane.

Concurrently, Glover et al. researched the performance of several working fluids in various RC configurations for coolant and exhaust WHR in which regeneration took place before, after, or parallel to the evaporator [101]. The authors found that for all fluids, once the coolant temperature exceeded 110^{o}C, performance increased. Moreover, optimum system performance occurred for critical temperatures just below coolant temperatures at heat ratios greater than one, with a direct relation between enhancing RC performance and increasing critical temperature. Ultimately, cycle efficiencies were found between 5 and 23%, with fuel economy improvements between 10 and 30%.

Continuing in 2015, Yang et al. completed a multi-parameter, multi-objective optimization of an RC system for CI engine exhaust WHR to obtain maximum power at minimum investment cost from six working fluid options [33]. Growing the evaporation pressure improved the thermodynamic and economic performance of the RC system, while increasing the condensation and evaporator exhaust temperatures displayed the opposite effect, with the degree of superheating negligibly influencing performance. Subsequently, R601a and R245fa displayed optimal thermo-economic performance; however, with comparable power output, and slightly fewer investment costs, R245fa proved to be the ideal working fluid. Specifically, R245fa achieved optimized performance for evaporation pressures from 1.1 to 2.1 MPa, a condensation temperature of 298.15 K, superheat degree between 0.5 to 20 K, and temperatures in the range of

414 to 417 K for torque above 500 N·m. Finally, as indicated in many other studies, the RC achieved the greatest thermal efficiency of 12% in medium to high operating regimes.

Jacobs addressed the changes facing ICEs in 2015, conducting a study of the effects of several new ICE technologies on WHR efforts [19]. Specifically, the influence of typical engine parameters (i.e., increasing EGR levels, decreasing equivalence ratios, increasing compression ratio), alternative fuels (i.e., bioCI), and alternative combustion modes (i.e., low temperature combustion) were investigated based on their impact on exhaust heat flow and exhaust temperature. Subsequently, it was determined that increasing engine parameters typically resulted in a growth in engine efficiency while leading to a decreased WHR efficiency and power output as a result of reduced exhaust exergy. Conversely, the combustion of alternative fuels had minimal effect on WHR opportunities, excluding the need to optimize performance for operating characteristics unique to the fuel. Finally, alternative combustion modes resulted in lower WHR potential, because of the lower exhaust heat flow.

The following year, Shi et al. attempted to improve the efficiency of an RC WHR system on an ICE through the installation of an Exhaust Gas Mixture Recirculation system (EGMR-RC) in which, as shown in Figure 2.8, exhaust gas from the evaporator in the RC recirculated and mixed with real-time exhaust gas before re-entering the evaporator [102]. This recirculation, in conjunction with an energy storage module and a design control approach, reduced the fluctuations in exhaust temperature, enabling more consistent RC operation. Using R134a as a working fluid, the EGMR-RC achieved a net power output of 0.9 kW and an overall efficiency of 7%, higher and steadier than that of the standalone RC. Furthermore, Shi et al. indicated that

EGMR-RC approach with an integrated control strategy could potentially improve WHR performance, with further study of transient operation and parameterization required.

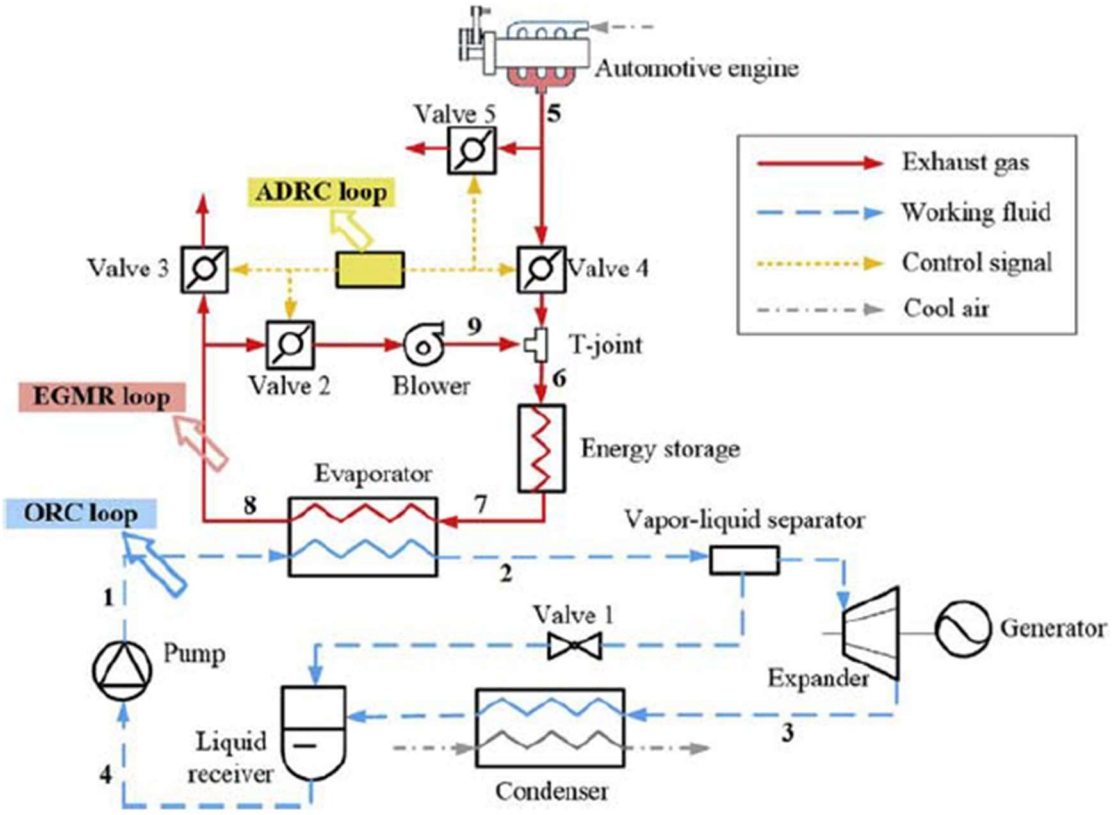

Figure 2.8: Schematic of the integrated EGMR-RC system implemented by Shi et al. [102].

Also in 2016, Ma et al. studied the utilization and configuration of a single loop CRC system for WHR from the exhaust and jacket cooling water of a natural gas generator [103]. The three working fluids compared were R123, R245fa, and R141b, and the three cascade heat source configurations contrasted were the exhaust gas only, full exhaust gas recovery with the jacket water as a preheat, and full jacket water and exhaust gas recovery. The thermal efficiency of the CRC depended on the working fluid; thus, R141b achieved the highest value of 21.82%. Conversely, WHR efficiency depended on the heat source utilized; thus, the full exhaust gas recovery with the jacket water preheat attained the greatest level. Furthermore, across three

loads, the configuration produced improvements in power output for the engine at 10.61% for 100% load, 12.09% for 75% load, and 14.23% for 50% load. However, the authors indicated the need for advancements in HEX sizing for growing evaporating pressures.

At the same time, Khaljani et al. proposed a DRC utilizing the exhaust gas and cooling water from a natural gas homogeneous charge compression ignition engine for WHR [104]. The RC system with the exhaust gas as a heat source used n-heptane as the working fluid, while the system with the cooling water employed R123. Although the addition of the combined cycle achieved 13.121 kW in additional power, maximizing the efficiency of the system through the evaporator temperature improved the total cost rate of the system. Furthermore, increasing turbine efficiency reduced exergy but grew the cost, while increasing the pinch point and condenser temperature reduced cost but enhanced exergy. Through a multi-objective optimization, the exergy efficiency increased 1.06% and the total cost rate decreased by $0.13/hr.

The same year, Shu et al. mathematically collated the performance of RC and DRC systems for WHR from a 1000 kW gas engine [105]. However, the operational intricacies of each type of cycle required different working fluids, configurations, and operating parameters. Specifically, the working fluids in the HT RC or DRC, LT RC or DRC, and RC were R245fa, toluene, and water, respectively. Subsequently, the DRC yielded the largest power output; however, the LT RC had the lowest system cost. Furthermore, the LT RC operated with the smallest electricity production cost, with trade-offs between cost and performance, in addition to condensing pressure and expander sizing.

Also in 2016, Shu et al. introduced the first of two studies on a RC system driven by multiple waste heat sources from a six-cylinder CI engine [106]. In the proposed CRC system, the HT loop recovered the engine exhaust and EGR, while the LT loop utilized the charge air and jacket water, in addition to the HT condensing heat, the residual exhaust heat, and residual EGR heat. Comparing the performance of working fluids for each loop, the combination of toluene (HT loop) and R143a (LT loop) obtained the greatest net power output, thermal efficiency, and exergy efficiency. Individual maximum available heat from the engine from the exhaust, EGR, charge air cooler, and jacket water were 156.0 kW, 9.1 kW, 37.5 kW, and 267.0 kW, respectively. Furthermore, the CRC obtained a maximum net power output of 38.2 kW, with thermal and exergy efficiencies of 11.3% and 38.7%, respectively, subsequently growing the original CI thermal efficiency by 16.0%.

Continuing the previous study by Shu et al., Yu et al. considered the thermo-economic performance of the same proposed CRC for WHR on a CI engine [107]. The thermo-economic indexes evaluated were component-to-system cost ratio (CSCR), EPC, DPP, and savings-to-investment ratio (SIR). The combination of toluene (HT loop) and R143a (LT loop) also obtained the best economic performance with the lowest EPC and DPP and highest SIR, 0.27 $/kWh, 7.8 years, and 1.6, respectively. The expanders and HEXs were ¾ of the total system cost, with the LT expander the single most costly piece of equipment. Evaluation of the CSCR indicated that increasing the engine speed lowered the EPC (0.48 to 0.27 $/kWh) and DPP (20.5 to 8.5 years) yet grew the SIR (0.85 to 1.65). Despite these trends, the cost of the system was not deemed advantageous for commercialization without further optimization.

Still in 2016, Yağli mathematically compared the performance of subcritical and supercritical RC systems using R245fa for exhaust gas WHR on a 12-cylinder biogas combined heat and power engine [108]. For the subcritical cycle, variations in turbine inlet pressure fluctuated trends in power and efficiencies, while increasing the turbine inlet temperature in the supercritical cycle at constant pressure enhanced performance. Moreover, the supercritical cycle outperformed the subcritical cycle in net power, thermal efficiency, and exergy efficiency, with maximum values of 81.52 kW, 15.93%, and 27.76%, respectively, at 38 bar and 163°C.

Meanwhile, Yang studied the economic influence of working fluid selection through the comparison of six different zero-ODP working fluids in an RC WHR system with four sources of waste heat for a 12-cylinder CI marine engine at 85% load [109]. Subsequently, R236fa yielded the lowest optimal LEC, as well as the shortest payback period. Conversely, R152a obtained the highest net power and thermal efficiency, while R1234yf achieved the greatest available efficiency with the lowest critical temperature. Finally, R152a had the largest heavy oil savings and CO_2 emission reduction. The results further elucidated the tradeoff in working fluid thermodynamic and economic performance as shown in Figure 2.9, with R152a displaying the best balance.

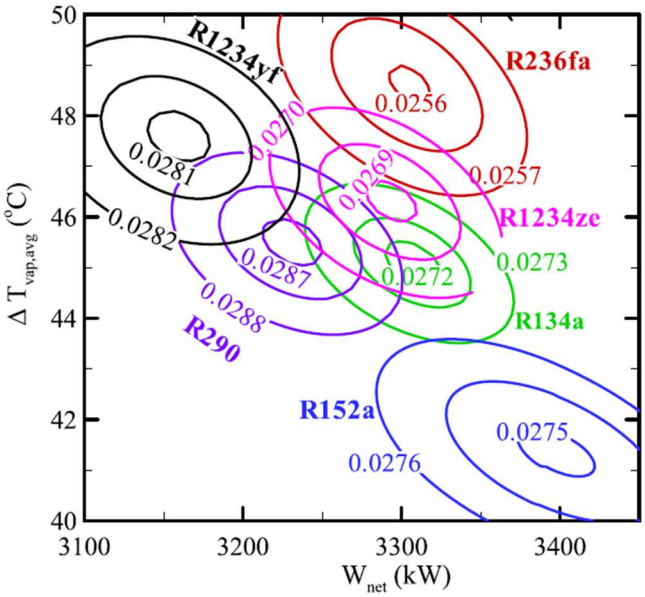

Figure 2.9: Various LEC values for working fluids based on varying vapor generator temperature difference and net work [109].

In another study published in 2016, Shu et al. experimentally surveyed R123 and R245fa as working fluids in an intermediate thermal-oil storage cycle and RC system (OS-RC) for WHR from HD CI engine exhaust [110]. Overall, R245fa performed better at light and medium loads across a range of expansion ratios, while the R123 could only match its performance at heavy loads with consistent expansion ratios. Based on the overall performance, the authors recommended the use of R123 for a HD truck and R245fa for a city bus.

Concurrently, Zhang et al. used a Monte Carlo simulation in conjunction with probability density functions to understand the interaction of various parameters in an RC WHR system from CI engine exhaust [111]. Furthermore, they included performance comparisons for ten different working fluids, subsequently determining that hydrocarbons produce a greater net power than refrigerants. Additionally, ICE load did not influence the mass flow rate for hydrocarbons, while increasing the mass flow rate of refrigerants grew the RC net power output.

Subsequently, ICE power and sink temperature (i.e., temperature of the cooling water in the condenser) influenced the RC net power output more than the pinch point temperature and the maximum RC net power output obtained was 21.1 kW with a thermal efficiency of 13.8% using R123.

Furthermore in 2016, Torregrosa et al. experimentally validated a bottoming RC WHR system on a gasoline engine in both steady-state and transient operating conditions using ethanol as a working fluid while developing a relatively simple control model for the system [112]. The results indicated that at lower expander speeds, in this case a swash-plate expander, heat transfer rates improved due to the increased residence time of the working fluid. However, under NEDC cold start conditions, the temperatures achieved were not high enough for expander operation. Ultimately, the new design controller considered high inertia (i.e., boiler, condenser) and low inertia (i.e., expander, pump) effects, subsequently yielding a potentially effective control methodology for realistic NEDC driving profiles.

At the same time, Galindo et al. completed an exergy analysis via conventional and advanced methods for an experimental RC for WHR from the exhaust of a CI engine using ethanol as the working fluid [113]. In the advanced analysis methodology, exergy was categorically studied as avoidable or unavoidable (i.e., due to design or manufacturing) and internal or external. The internal exergy was larger than the external, indicating that the majority of irreversibility occurred within an individual component. Furthermore, the components with the largest avoidable exergy destruction were the expander and the pump, necessitating design improvement

priority. Further analysis on the influence of the pinch point in the boiler and the expander improved the cycle efficiency by 21% and reduced the exergy destruction by 4 kW.

In their next work in 2016, Galindo et al. multi-objectively optimized an RC WHR system from the exhaust of a turbocharged gasoline engine, with ethanol as a working fluid and a swash-plate expander [114]. The initial results quickly indicated the negative linkage between the thermo-economic and sizing parameters; namely, reducing thermo-economic criteria required greater sizing, while reducing sizing criteria required increased thermo-economic parameters. Thus, the authors developed a weighted methodology to analyze three components of design, specific investment cost (SIC), area of the HEXs (A_{total}), and volume coefficient (VC), with weight factors of 0.5, 0.3, and 0.2, respectively, for optimized values of \$3075/kW, 0.48 m^2, and 2.62 MJ/m^3, respectively. Generalized trends of the individual components were that SIC increased with increasing expander isentropic efficiency, and higher superheating temperatures increased both A_{total} and VC, due to the reduced pinch point in the evaporator and the higher enthalpy drop across the expander, respectively.

Continuing work in 2016, Uusitalo et al. studied the influence of installing an RC WHR system on GHG emissions in two operating scenarios for electricity production from a biogas engine with toluene as a working fluid [115]. In the first operating situation, the electricity and waste heat from the engine were utilized in the plant, while in the second only the electricity was utilized. When the exhaust heat and the produced electricity were consumed by the plant, GHG emissions increased with the inclusion of the RC due to the greater waste heat production necessary to accommodate the lower waste heat temperatures following the RC. Conversely, in

the scenario where the waste heat was otherwise unused, the inclusion of an RC decreased GHG emissions. Ultimately, the results indicated that while an RC could reduce GHG emissions, the extent depends on the plant where the system will be operating.

Again in 2016, Xia et al. generated a model of a combined cooling and power system in which, the BC recovered waste heat from the ICE exhaust using CO_2, the RC recovered waste heat from the condenser of the BC using isobutane, while the refrigeration cycle recovered residual waste heat from the exhaust also using isobutane [116]. Subsequently, key operating parameters indicated that growing the BC turbine inlet temperature, RC turbine inlet pressure, and flow pressure of the refrigeration cycle increased exergy efficiency. Furthermore, performance degradation occurred when the compressor pressure ratio and inlet temperature were enhanced. Minimizing the average cost per unit of exergy product ($63.53/MWh) yielded an allowable exergy efficiency of 27.63%.

de Oliveira Neto et al. furthered the literature in 2016 by contrasting the installation of an RC WHR system in a power plant using the exhaust gas of a stationary CI engine with an urban water supply or a dedicated cooling tower as sources of the engine coolant water [34]. Of the working fluids compared, toluene exhibited the highest thermal and exergy efficiencies with a 20% power increase for both configurations. Furthermore, an economic analysis indicated that the shortest payback period was for toluene in the system without a cooling tower.

Additional work in 2016 finds Yu et al. building a cascaded steam RC and R123 ORC system (RC-ORC) for WHR from CI engine exhaust by modifying an OS-RC system [117]. Figure 2.10 shows the existing OS-RC system and the modifications Yu et al. made to create the

RC-ORC system. Operating at medium-high loads and speeds, 101.5 kW of waste heat was available from the six-cylinder test engine. Using expansion valves in place of expanders, an estimated 6.9-12.7 kW of mechanical power was obtained for the RC-ORC system, improving the power beyond the CI engine alone and the combined engine and OS-RC by 5.2% and 3.2%, respectively.

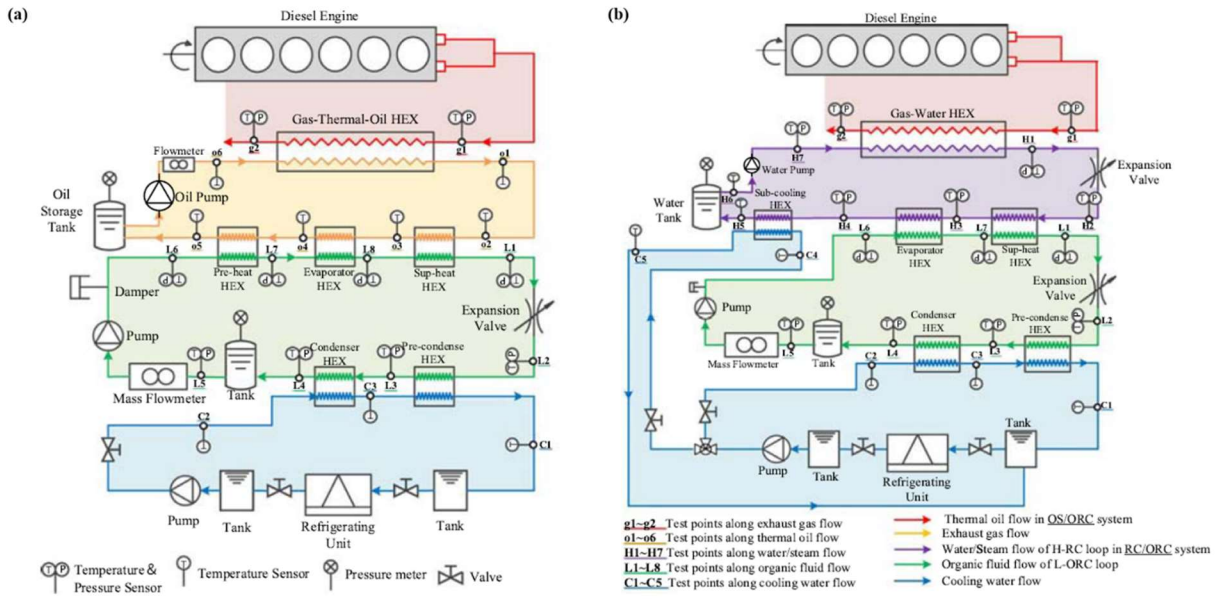

Figure 2.10: Diagrams of (a) the existing OS-RC system and (b) the modified cascade RC-ORC system used by Yu et al. [117].

Also in 2016, Grelet et al. assayed four RC heat source configurations for WHR in steady-state and transient operating profiles from a HD truck: exhaust gases, EGR, both exhaust gas and EGR in parallel, and exhaust gas and EGR in series [118]. Furthermore, a brief consideration of working fluids and cooling configurations yielded ethanol as the working fluid with a dedicated RC radiator. Subsequently, the EGR and exhaust gases in parallel yielded the best performance, followed by both sources in series. The authors noted that the same general trends were seen during transient and dynamic driving profiles, indicating that the simpler steady-state analysis could be used to develop a qualitative study.

That same year, Morgan et al. utilized an exhaust RC WHR system on a CI engine to evaluate the performance of a novel intra-cycle based WHR concept, in which an evaporator recovered waste heat from the intake air flow between separate compression and combustion chambers [119]. Modeling consequently revealed that the RC reached higher maximum working fluid (50/50 water/ethanol) temperatures and greater heat recuperating efficiencies; however, the split cycle experienced lower combustion temperatures and enhanced overall efficiencies. Comparatively, the split cycle achieved a thermal efficiency of 52.2% while the RC achieved 44.2%.

Moreover, in 2016 Shu et al. rigorously compared the performance of a CO_2-based transcritical Rankine cycle (CTRC) with preheat and regeneration (PR-CTRC) to that of a basic CTRC and a transcritical PRRC using R123 employing WHR from the exhaust gas and coolant (preheat) [120]. Subsequently, the PR-CTRC outperformed the basic CTRC with a net power output increase of 150%, a thermal efficiency growth of 184%, and an enhancement in exergy efficiency of 227%, while also outperforming the PRRC at high turbine inlet temperatures. However, although the basic CTRC required a smaller total heat transfer area than the basic RC, the PR-CTRC required a larger total heat transfer area than the PRRC, presenting design drawbacks.

Concurrently, Ziviani et al. tested the performance of a small-scale RC test rig using a single-screw expander and a simulated waste heat source while comparing R245fa and SES36 as working fluids [121]. Consequently, although R245fa yielded a 10% improvement in power output, SES36 allowed the expander to operate at a higher isentropic efficiency and achieve

greater pressure ratios. Thus, SES36 achieved a peak overall isentropic efficiency of 64.7% with improvements achievable through the reduction of mechanical and friction losses.

At this point, Zhou et al. compiled a comprehensive review of Rankine cycle designs, components, and working fluids used in literature over the past 20 years until 2016 for vehicle WHR [26]. Of the available energy sources, engine coolant and exhaust gas are the most popular; however, due to its higher temperature range, exhaust gas displays greater potential for energy recovery. Furthermore, the most critical component is the expander, of which there are four primary types and selection depends on design conditions. Similarly, working fluid selection is crucial to RC operation, but highly dependent on working conditions and expander selection. Generally, water is ideal for high temperature operations, but at lower temperatures organic fluids are preferred. Finally, hybrid vehicle systems provide an ideal integration scheme through conversion and storage of electricity in the existing hybrid system, while operating at relatively constant engine loads, making the optimization of RC performance easier.

Continuing in 2016, Xu et al. created a model of an RC for HD CI WHR using a finite volume method and a pressure drop model [122]. Of note, both the exhaust gases and EGR were utilized as waste heat sources through separate evaporators in parallel, with ethanol as the working fluid. For both steady-state and transient operating conditions, the results were validated from experimental results, within 10% error for the transient case. Upon this validation, the authors state that their model can be subsequently used for further optimization.

Also in 2016, De Rosa et al. numerically analyzed the performance of a DRC for five working fluids across a range of operational conditions [123]. In the DRC, the first loop utilized

the exhaust gas as a heat source, while the second loop utilized the coolant as a heat source before, after, or parallel to the regenerator. The five working fluids tested, but not directly compared, were R1234-yf, ipentane, R245fa, butane, and R134a. Consequently, it was determined that putting the coolant HEX after the regenerator yielded the best performance for all working fluids.

Furthermore in 2016, Cipollone et al. designed an experimental bottoming RC for WHR from a HD CI engine, utilizing a finned coil evaporator, a plate heat condenser, and an impulse axial turbine with R245fa as the working fluid [124]. Operating the engine at medium to high load conditions, the system achieved overall net efficiencies of 3-4% including conversion losses, with 2 kW of electrical power recovered. Moreover, they state that there exists the potential for improvements through technological developments and reductions in induced backpressure.

Moreover in 2016, Shu et al. again focused on the topic of RCs for WHR, this time using a rated 1,000 kW natural gas engine and water as a working fluid [125]. Through the variation of the exhaust mass flow rate and temperature at the inlet of the evaporator, the authors investigated the dynamic performance of the RC system. For a reduction in the exhaust mass flow rate or evaporator inlet exhaust temperature, the evaporating pressure correspondingly decreased, and the thermal efficiency and output power of the RC system decreased significantly. Moreover, the same diminutions in exhaust mass flow rate or inlet temperature directly result in diminished waste heat, but the subsequent cool exhaust final temperature led to improved waste heat

utilization. Notwithstanding, significant consideration must be given to the interaction of the aforementioned operating parameters for full optimization of the RC performance.

In a simulation of an RC for WHR from the exhaust of a CI engine in the same year, Wiedemann et al. achieved an average fuel savings of 3% through realistic, non-isentropic expansion efficiencies and a pinch point analysis over the engine's entire operating region [126]. The RC model utilized ethanol as the working fluid, a screw-type expander, and plate HEXs. In simulating the RC system for marine and rail applications, the marine environment outperformed rail operation. Specifically, marine had the highest fuel savings, an average of 3%, between 40-90% engine loads.

In continuation of a busy year, Kim et al. surveyed four different single-loop configurations of an RC for exhaust WHR from a six-cylinder gasoline engine, including a novel dual heat source configuration [127]. The specific configurations were: Case 1 using an engine coolant preheater and R245fa; Case 2 with an engine coolant preheater and a recuperator and R245fa; Case 3 with vaporization by the engine coolant and a recuperator using R245fa and R134a; and Case 4, the novel configuration including low and high temperature recuperators and vaporization by the engine coolant using R245fa and R134a. For Cases 3 and 4, R134a yielded higher system and thermal efficiencies, as well as a superior net power output. Furthermore, although Cases 1 and 2 achieved greater thermal efficiencies, Case 3 yielded an enhanced net power output and system efficiency due to full utilization of the waste heat of the coolant. However, Case 4 outperformed all three other cases in net power output and system efficiency, obtaining values of 5.63 kW and 10.8%, respectively, with R134a as a working fluid.

Hærvig et al. adapted general guidelines for working fluid selection according to heat source temperatures for a basic RC employing WHR in 2016 by optimizing their model over 26 pure working fluids and three mixtures for heat source temperatures varying between 50 and 280°C [128]. Generally, the ideal working fluid has a critical temperature that is 30-50 K below the heat source inlet temperature. Furthermore, if multiple potential working fluids have similar critical temperatures, the fluid with the lowest, positive, vapor saturation slope is preferred. For an ideal mixture, the temperature glide should be approximately equal to the cold source temperature change.

The following year, Lu et al. investigated the use of a scroll expander in an RC system for exhaust WHR from a 6.5 kW Yanmar engine using R245fa as a working fluid [129]. In the RC system, an intermediate oil loop passed the engine exhaust energy to the working fluid, preheated by the engine coolant. With a heat sink temperature of 20°C, the system produced 1 kW of power, with the scroll expander achieving speeds of 4000 RPM, stated as being suitable for coupling to a conventional generator.

In 2017, Li et al. experimentally examined the influence of condenser cooling water temperatures and working fluid superheat at the turbine inlet on the performance of an RC for low-grade WHR using R245fa, an oil boiler as the heat source with a plate evaporator, and a turboexpander with a generator [130]. When the heat source temperature and flow rate were constant, the power output and cycle efficiency increased as the cooling water temperature decreased. Conversely, at constant cooling water temperatures, condensing pressures were unaffected by the degree of superheat, while increasing the superheat at the turbine inlet

negatively affected cycle power output and efficiencies; thus, stressing the importance of utilizing the superheat as a cycle control parameter. Furthermore, the maximum power obtained from the turboexpander was 5.405 kW for a cooling water temperature of 23°C and a pressure ratio of 2.3.

Yu et al. in the same year established a model for the simultaneous optimization of heat integration and techno-economic factors for an RC from a refinery chemical process utilizing a hot water intermediate cycle via four working fluids for WHR [131]. In their work, R600a achieved the greatest power output of 1490 kW, with the highest total annual cost, while R227ea obtained the lowest total annual cost and a power output of 1098 kW. Overall, the results of simultaneous economic, thermodynamic, and heat integration optimization increased the net power output of the basic thermodynamic optimization by 24.3%.

Based on the RC system designed in [129] with a scroll-expander, Lu et al. continued their efforts in 2017 by evaluating the performance of six different working fluids [132]. Of the working fluids considered, R152a at an expander inlet temperature of 200°C achieved the highest power output of 1.2 kW, followed by R134a at 1.15 kW for expander inlet temperatures between 140-170°C. Furthermore, R152a obtained the highest overall thermal efficiency of 41%, with the lowest BSFC.

Also in 2017, Wang et al. inspected the transient performance of an RC system for exhaust gas WHR on a natural gas engine in Simulink using R245fa as the working fluid [133]. Of note, the RC system also included a hot water intermediate cycle with a finned tube HEX; whereas, the evaporator was a counterflow, straight tube HEX. While the condensing pressure remained

relatively unchanged for varying engine conditions and pump speed, the evaporating pressure increased linearly with decreasing pump speed and engine conditions. Conversely, the superheat degree and working fluid enthalpy change grew for decreasing engine operation. All three parameters responded more slowly as engine operating conditions (i.e., load and speed) fell, with the evaporation pressure responding the fastest. Improved control performance at lower load conditions through controller alterations indicated the importance of a properly designed control system.

Alternatively, Seyedkavoosi et al. proposed a novel two-step RC configuration in 2017 for WHR from a 12-cylinder gas-fired ICE using the exhaust gas in the first loop and the engine coolant in the second with a dual expander [134]. At the set engine operating condition, R123 performed better than water or R134a, achieving an exergy efficiency of 21.01% as compared to 13.16% and 8.80% for water and R134a, respectively. Furthermore, the pressure of exhaust heat recovery influenced the system performance more than the pressure of the coolant recovery. Moreover, the expander efficiency was the largest opportunity for improvement, such that a 30% increase in its efficiency improved the net output power by 53%.

Meanwhile, Lu et al. examined the performance of four different optimized RC configurations on the exhaust of a single cylinder CI engine for WHR using R245fa as the working fluid [25]. The baseline configuration utilized the engine's exhaust gas and coolant, and modifications included using a recuperator between the pump and the engine coolant HEX, a recuperator between the coolant and exhaust HEX, and a traditional PRC using the exhaust with the coolant as a preheater. Although, the PRC exhibited the highest efficiency, the placement of

the recuperator between the pump and engine coolant HEX yielded the greatest power output, as well as the maximum BSFC reduction and overall efficiency improvement across all engine loads, making it the superior configuration.

Furthermore in 2017, Tian et al. experimentally validated the concept of an FP coupled with a linear generator (FPLG) for future use in RC WHR systems using a test set-up with compressed air as the working fluid [135]. Although the piston displacement profile was similar to that of a sinusoidal wave, the motion symmetry improved as the intake pressure increased. A maximum power output of 96 W was achieved for an operational frequency of 1.0 Hz and an external load resistance of 20 Ω; however, the maximum energy conversion efficiency of 45.82% was achieved for 2.0 Hz and intake pressure of 2.6 bar. The power and conversion efficiency achieved validated the concept of using the FPLG in an RC system, with further work needed for actual implementation.

Kuboth et al. utilized an iterative approach in the same year to reduce the error between experimental data and simulation results for RC efforts [136]. The experimental set-up consisted of a scroll expander, a gear pump, and brazed plate HEXs for the evaporator, condenser, and internal recuperator, with R365mfc as the working fluid and a thermal oil circuit heat source. Two simulation models were created in Aspen Plus; the first calculated state points throughout the system, while the second used the results of the first simulation with experimental data to refine the findings and reduce deviations. From the original model, deviations of 8.4% and 4.1% existed between the model and the experiments for the state enthalpy and pressure values, respectively. However, using the semi-empirical second model, the deviations were reduced to

0.6% and 1.2% for the enthalpy and pressure values. Thus, the integration of experimental results into the simulation improved its overall accuracy.

Concurrently, Galindo et al. created and experimentally substantiated a 1-D RC model for WHR from the exhaust of a gasoline engine with ethanol as the working fluid over a portion of the NEDC [137]. Subsequently, the maximum power extracted by the swash-plate expander was 800 W, with a BSFC reduction of 23.5 g/kWh, yielding an improvement of 2.5% in fuel conversion efficiency. The best performance was achieved by the system at higher operating points, with the expander limiting performance improvements at low speeds.

In an effort to improve the efficiency and design of turbines used in RC WHR systems, in 2017 Alshammari et al. introduced a novel design methodology optimizing the rotor exit tip radius and the inlet blade angle of a radial expander through the total-to-static isentropic efficiency [138]. Subsequently, increasing the rotor tip by 9.5% raised the isentropic efficiency from 73% to 82%, and enlarging the inlet blade angle from 0^{o} to 54^{o} further grew the isentropic efficiency to 83.5%. Validation of the optimization using CFD analysis indicated an isentropic efficiency of 81.3%, an improvement that would still benefit eventual RC performance.

The same year, Kosuda et al. proposed a prototype RC configuration, which employed air cooling in the fin-and-tube condenser, HFC3654mfc as a working fluid, and a thermal oil bath as the heat source [139]. Furthermore, the expander was a volumetric scroll type, with a brazing plate HEX regenerator and a tube evaporator. For a condenser ambient temperature of 20^{o}C and an expander inlet temperature of 175^{o}C, the total power generated was 1.027 kW with gross and net power generation efficiencies of 10.5 and 9.0%, respectively. Furthermore, of the generated

power, the pump and fan accounted for only 12.7%, yielding a large ratio of effective generated power. Future improvements included reducing the piping pressure and the heat dissipation losses, as well as improving expander efficiency.

In 2017, Bufi et al. implemented a parametric optimization of an RC for exhaust WHR from a HD CI engine that included the uncertainty in various operating parameters, such as exhaust gas mass flow rate and temperature, turbine and pump efficiencies, and condensing temperatures [140]. From this optimization, R11 and R113 displayed the best performance, with thermal efficiencies of 20.8% and 19.2%, respectively. Furthermore, the expander efficiency and condensing temperature had the greatest influence on the thermal and exergy efficiencies. Subsequently, a robust optimization identified a necessary compromise between various operating parameters and system performance in order to minimize the variability of the RC system.

At the same time, Zhao et al. experimentally inspected the influence of varying recuperation rates on an RC system for exhaust gas WHR on a HD CI engine using R245fa as the working fluid [141]. Under steady-state conditions at the rated engine load, as the recuperative rate rose, the net output power increased, and the cooling heat decreased, at the cost of prolonged time to reach steady-state at start-up and increased working fluid mass required. Under transient operation, the recuperative cycles overshot the temperatures and power during the start-up phase, posing a threat to the expander. Finally, with the recuperator having minimal effect on the backpressure of the engine, the improved recuperative RC performance came with relatively few drawbacks.

Concurrently, Rijpkema assessed four different power cycles and four unique working fluids from four distinct waste heat sources for low speed, medium load operation on a HD CI engine [142]. The power cycles investigated were the RC, the TRC, the trilateral flash cycle (TFC), and the single flash cycle (SFC). Additionally, the working fluids considered were cyclopentane, ethanol, R245fa, and water, while the four waste heat sources were the CAC, coolant, EGR cooler, and exhaust. General trends in thermal efficiencies are shown in Figure 2.11. For the CAC as a heat source, both the TFC and SFC achieved the best efficiency and net power for all working fluids. Conversely, using the coolant as a heat source, the RC achieved significantly higher net power and thermal efficiencies for all working fluids. For the EGR cooler, ethanol was the preferred working fluid, obtaining similar performance parameters in the RC and TRC, while all cycles performed similarly with the exhaust as a heat source. Ultimately, the power cycle chosen influenced performance more than working fluid selection.

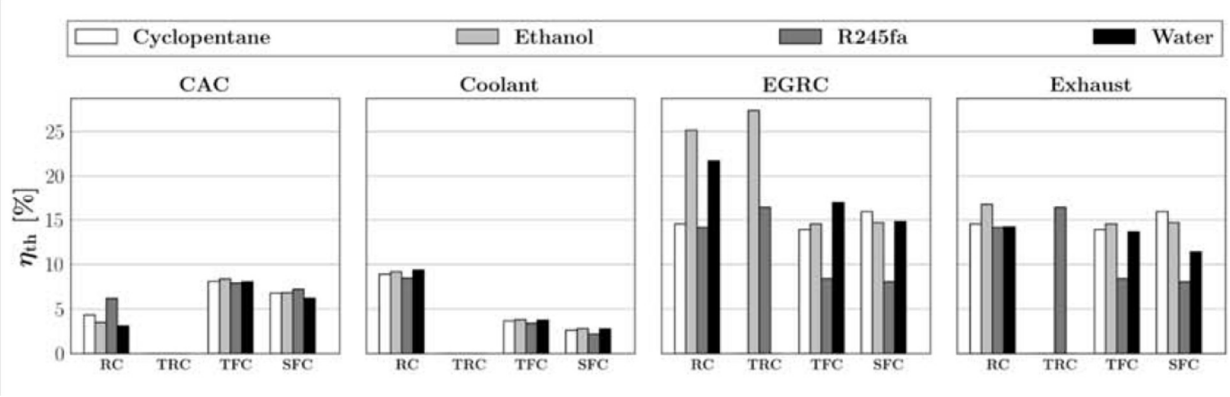

Figure 2.11: The variation in thermal efficiencies for working fluids in four different power cycles with different heat sources [142].

Lion et al. completed a combined first and second law analysis in 2017 to identify inefficiencies within a DRC system on the exhaust and coolant streams of a six-cylinder CI ship engine with a LP EGR system [143]. At 100% engine load, the combination of DRC and EGR improved the RC net power output by 77 kW over just the DRC system with steam as the

working fluid for exhaust heat recovery and R1233zd for coolant heat recovery. Furthermore, the largest system inefficiencies were in the evaporator at the high speed, high load condition.

Furthermore in 2017, Landelle et al. experimentally tested a transcritical RC (TRC) utilizing a scroll expander, plate HEXs, and R134a as the working fluid with an electrical boiler as the heat source [144]. Seventy different steady-state points were tested in the rig, yielding the highest power output of 1.5 kW and maximum thermal and exergetic efficiencies of 1.0% and 1.8%, respectively, with these results attributed to low pumping efficiencies. Individual analysis of the components indicated that the regenerative configuration increased the exergy efficiency of the HEXs, while the condenser accounted for the largest portion of exergy destruction.

Continuing their work in 2017, Shu et al. focused on the response time of 14 different working fluids in an RC for WHR from the exhaust of an eight-cylinder natural gas engine with counterflow, straight pipe HEXs and a nozzle as the expander [145]. Consequently, Figure 2.12 displays the enthalpy response times of various working fluids, with low temperature working fluids responding faster to system changes, while high temperature working fluids acted slower. The same general trends were seen for changes in evaporating pressure. Other working fluid parameters that yielded faster response times included small heat capacity, lower evaporating latent heat, high working fluid mass flow rate, reduced critical temperature, and low density. Although these properties cannot be manipulated or found in a working fluid, straight-chain alkanes specifically exhibited a direct relationship between an increase in critical temperature and a growth in response time.

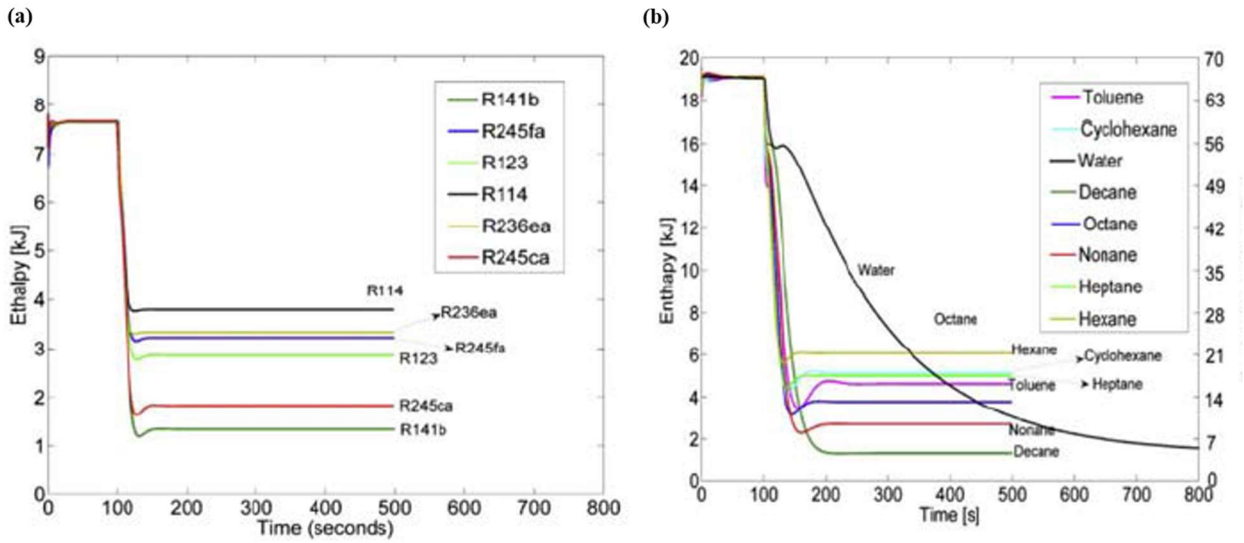

Figure 2.12: Response time of enthalpy changes for (a) LT and (b) HT working fluids [145].

Also in 2017, Pang et al. experimentally evaluated the performance of various mass fraction ratios of R245fa/R123 mixtures in an RC system for WHR using a scroll-type expander and a heating oil circuit as a low-temperature waste heat supply [146]. As the working fluid mass flow rate increased, heat input and pump power consumption rose, while the net power efficiency grew and then fell. A 2:1 mixture of R245fa/R123 yielded the highest maximum net power efficiency and net power of 4.4% and 1.66 kW, respectively, at the heat source temperature of 120ºC and a mass flow rate of 0.15 kg/s. Moreover, pure R123 achieved the same maximum power efficiency as the 2:1 R245fa/R123 blend, but with a net power output of only 1.52 kW at a heat source of 120ºC and a mass flow rate of 0.176 kg/s. However, mixtures provide a wider spectrum for waste heat applications, with the authors indicating the potential for a better thermal match to the applied system.

Concurrently, Chen et al. presented the use of a confluent cascade expansion RC (CCE-RC) for WHR from the engine coolant and exhaust gases on a six-cylinder CI engine, replacing the

conventional DRC system [147]. Compared to a DRC system, the CCE-RC negated the use of a second thermal reservoir and an intermediate HEX, resulting in an 18% decrease in total HEX volume. Six working fluids were considered, with cyclopentane achieving the highest net power; thus, it was selected as the primary working fluid. Subsequently, simulations indicated that the CCE-RC achieved a peak thermal efficiency of 49.5%, a 4.2% increase from the DRC. Furthermore, the minimum BSFC of the CCE-RC system decreased to 169.9 g/kWh, as compared to 185.6 g/kWh. Overall, the CCE-RC generated 7.94% more net power than the DRC, in addition to decreasing the system size due to the removal of the intermediate HEX.

Lemmens et al. completed a thorough economic analysis of a 375 kW basic, subcritical RC system using R245fa for flue gas heat recovery from an industrial kiln in Belgium in 2017, while considering policy impacts [148]. The authors examined applicable potential discount rates, initially yielding a positive net present value (NPV) for the system at varying discount rates; however, the specific system studied was not always in operation, lowering the NPV. The initial rate of return was heavily influenced by the taxes imposed, depending on system location and governmental subsidies. Furthermore, the capital investment was the largest determinant of the NPV, while the annual costs affected it minimally. Finally, the annual load hours of the system and the electricity price were the largest factors influencing the NPV.

Meanwhile, Yang et al. varied the mass fractions of R1234yf/R32 mixtures as working fluids in a TRC for 180ºC ICE exhaust gas WHR [149]. From the simulations, the optimal mass fractions were 0.8/0.2 R1234yf/R32 at an expander inlet temperature and pressure of 150ºC and 6 MPa, respectively, for an LEC of $0.205/kWh. This resulted in an improvement of 1.46% over

pure R1234yf and 4.88% over pure R32, while allowing for more variation in expander design. Furthermore, the mass fraction of R32 in the mixture was proportional to the optimal expander inlet temperature and pressure, yet inversely proportional to the condensation temperature.

Also in 2017, Budisulistyo et al. employed a comprehensive optimization methodology to improve the design of an existing RC WHR system on a gas turbine with an intermediate thermal oil circuit and 50% R245fa/50% R365mfc as the working fluid [150]. Subsequently, the model investigated the size of the three HEXs in the system (thermal-oil HEX, evaporator, and condenser) for optimal performance over three operating points of the gas turbine. A completely new design, in which all three HEXs were resized, achieved the highest power output and the greatest net power output to total HEX area ratio. Furthermore, the new design utilized 76.9% of the available waste heat, indicating that the new design strongly fit the waste heat profile of the studied gas turbine.

Feng et al. experimentally collated the performance of R245fa, R123 and their mixtures as working fluids in an RC WHR system with a scroll-type expander, a plunger pump, plate HEXs, and a constant electric heater source temperature of 120^{o}C in the same year [151]. A rooftop cooling tower was utilized; thus, the environment dictated the cooling temperatures. Subsequently, a mixture of 0.67 R245fa/0.33 R123 achieved the highest maximum thermal efficiency of 7.33% and net electricity output of 1.67 kW. However, such improvements in thermal performance came at the cost of consuming up to 0.108 kW more in pump power than the pure fluids

In their final publication in 2017, Shu et al. generated a model of an RC system using the operational profile of a cruise ship engine with seven working fluid candidates for extracting the waste heat from the engine's exhaust [152]. In their work, R123 and R365mfc achieved the highest maximum exergy efficiencies across all loading conditions, while exhibiting the lowest electricity production cost and depreciated payback period at the design evaporating pressure. Between the two, R123 yielded higher power output at heavy engine loadings, making it well suited for container ships. Conversely, R365mfc performed better at light engine loadings in which tankers operate.

Tian et al. optimized the configuration of a CO_2 transcritical power cycle (CTPC) using the waste heat of a six-cylinder, turbocharged CI engine in 2017 [153]. In addition to the basic CTPC, the addition of a preheater (P-CTPC), a regenerator (R-CTPC), or both (PR-CTPC) was considered. The CTPC and the P-CTPC displayed the worst thermodynamic performance, while both the R-CTPC and the PR-CTPC exhibited improvements in thermodynamic performance, indicative of the importance of a regenerator. Although the PR-CTPC displayed better thermodynamic performance than the R-CTPC, with 17.44% higher net power output and 4.98% greater exergy efficiency, it also achieved a 4.11% larger EPC. Regardless, the PR-CTPC was the optimal solution of all four configurations considered, achieving an optimum power output of 24.24 kW with an exergy efficiency of 36.88% and an EPC of $0.583/kWh.

Similarly that year, Shi et al. implemented a basic CTRC, a CTRC with regeneration, a CTRC with preheat, and a PR-CTRC for a WHR comparison using the exhaust gas and coolant of a six-cylinder CI engine [154]. Furthermore, the evaporator was a double-pipe HEX, while the

preheater and regenerator were brazed plate HEXs, in coordination with an expansion valve instead of an expander. Comparing the performance of all four cycles at a set pressure ratio of 1.65, the PR-CTRC yielded the highest net power output and efficiencies of 3.47 kW, 7.8% (thermal), and 17.1% (exergy). Additionally, the PR-CTRC, aside from power and efficiency improvements, also reduced the cooling load of the combined engine and PR-CTRC by 18.1% as compared to the basic CTRC.

Other work in 2017 finds that Liu et al. built a mathematical model using MATLAB to optimize the design and cost of a fin-and-tube evaporator in an RC WHR system to recover the waste heat of the exhaust of a CI engine using R245fa [155]. Simulations indicated that for an increase in the inlet radius on the tube side, the exhaust pressure drop and tube bundle volume grew, as the total annual cost diminished. Conversely, for a growth in the inlet radius on the shell side, the opposite phenomena occurred. Furthermore, raising the fin height increased the tube bundle volume, but diminished the pressure drop and total annual cost, while the fin thickness and spacing negligibly affected these items. From the optimized evaporator design, the tube bundle volume increased by 6.49% from the original design, decreasing the annual cost and exhaust pressure drop by 71.46% and 27.6%, respectively.

At the same time, Kyriakidis et al. considered two different configurations of a steam RC WHR system on a two-stroke marine CI engine with an integrated EGR system with two or three pressure levels [156]. A performance evaluation in MATLAB revealed that the configuration with three pressure levels generated 1641 kW of net power; whereas, the two pressure level

generated only 1577 kW at lower steam mass flow rates. Thus, the configuration with three pressure levels was better suited for marine CI engines.

Also in 2017, Yang assayed the performance of 50% by volume mixtures of R32, R161, R290, R1234yf, and R1234ze with CO_2 as working fluids in a TRC for low-grade waste heat recovery [157]. The mixture of CO_2/R161 exhibited the best economic performance, with a 21.52% improvement in LEC over pure CO_2. Furthermore, in addition to decreasing the LEC of the system, the CO_2 mixtures allowed for improved maximum thermal efficiencies at optimal expander inlet pressures and temperatures.

With benzene as a working fluid, Mondejar et al. used quasi-steady state modeling in 2017 to assess the applicability of a RRC for WHR from the exhaust of the four main CI engines and four auxiliary CI engines on-board a cruise ship [158]. The RRC system displayed optimal performance when the ship was cruising in the open sea with the main and auxiliary engines running, with poor performance at low mass flow rates when the ship was in port. However, the average net power production of the RRC over the four-week trip was 396 kW, or 22% of the total on-board power consumption and followed similar trends as the power demand of the ship.

Panesar devised a DRC system in 2017 to utilize direct engine block heat energy in addition to exhaust gas waste heat for WHR [159]. In this novel RC configuration, the low pressure and temperature loop extracted the engine block waste heat directly and subsequently validated its performance against a reference CRC. Furthermore, while water and R245fa were the working fluids in the HT and LT loops of the CRC, respectively, blends of water and 1-propanol and water and 3-ethyl-1-butanol were used in the DRC. The simulated DRC improved the system

power, power density, and brake thermal efficiency by 20%, 33%, and 5.3% respectively, while reducing the total heat transfer footprint by 50%. Replacing water and R245fa with a single water blend lessened the HEX performance in the HP loop; however, this could be compensated through condenser improvement in the LP loop.

Wang et al. analyzed the performance of a supercritical-subcritical DRC system with and without regeneration for WHR from the exhaust gas and coolant of a six-cylinder CNG engine in 2017 [160]. The primary working fluid pair studied was R1233zd in the HT loop with R1234yf in the LT loop. However, for further comparison R245fa/R134a, toluene/R134a, and water/ethanol were included as HT/LT working fluids. Although the thermal efficiency of the water/ethanol mixture was the largest, even without regeneration, the required size of the turbine and HEXs was undesirable. Furthermore, R1233zd/R1234yf achieved a higher thermal efficiency than R245fa/R134a with lower toxicity and GWP; thus, R1233zd/R1234yf was the most adequate working fluid pair, subsequently improving fuel efficiency by over 8%.

Additionally in 2017, Uusitalo et al. surveyed the performance of plate-and-shell HEXs in an RC system for WHR from the exhaust of a six-cylinder CI generator [161]. After analyzing several different working fluids, siloxane MDM was chosen as the working fluid and in lieu of an expander, the experimental setup contained an expansion valve. Subsequently, the evaporator achieved a maximum heat transfer rate of 59 kW while maintaining a pinch point temperature difference below 14^{o}C. Furthermore, using an expander efficiency of 75%, the system attained an estimated maximum power of 8.1 kW.

The same year, Xu et al. optimized the power of an RC exhaust and EGR WHR system on a HD CI engine under transient operating conditions using ethanol [162]. Moreover, system variation appeared in the form of the three mixed vapor temperature conditions entering the turbine: constant vapor temperature, constant superheat temperature, and a fuzzy logic vapor temperature that determined the vapor temperature from the waste power level. Following transient simulations and using constant vapor temperature as a baseline, the constant superheat improved RC net power by 1.1%; whereas, the fuzzy logic option improved the net power by 2.1%. Consequently, further recommendations for power improvements involved additional parameters for the fuzzy logic strategy and experimental validation.

For marine applications, Liu et al. investigated a cogeneration strategy in 2017 consisting of an RC for exhaust WHR and an absorption refrigeration cycle (ARC) for cooling [163]. Specifically, the RC generated electricity for on-board use, while the ARC recovered the heat from the RC condenser to provide further cooling capacity. Based on the high-temperature exhaust of a Wartsila low-speed CI engine, benzene, toluene, cyclohexane, and cyclopentane were compared as working fluids in the RC, with ammonia and water was the working fluid pair in the ARC. Subsequently, the best performing working fluids for cogeneration were toluene for high evaporation systems followed by benzene in low evaporation systems, with maximum exergy efficiencies of 50.8% and 48.3%, respectively. Moreover, at an RC condensation temperature of 135^{o}C, the highest energy ratios of the WHR system were achieved with benzene (63.9%) and toluene (64.9%).

At the same time, Merrett et al. employed two studies from 2011 to validate a simulation tool for RC WHR systems used on HD CI engines [164]. The previous studies by Teng et al. and Park et al. utilized the EGR and exhaust as heat sources, then experimentally tested the performance of the WHR system over 13 ESC operating conditions [165, 166]. Merrett et al. then validated their simulation, achieving errors less than 2% for temperatures and pressures and less than 5% for turbine power output, allowing for further system manipulation and development prior to the costly implementation of experimental setups.

Also in 2017, Yu et al. generated an RC model for WHR from the exhaust gases of a CI engine utilizing a reciprocating piston expander [167]. Choice of ESC 13-mode operating conditions provided exhaust gas conditions for simulation with R245ca as a working fluid. Increasing the evaporating pressure positively influenced the piston expander operation; thus, achieving a maximum recovery efficiency of 33.8% for an evaporating pressure of 1.1 MPa under the C25 operating condition. Parameters such as output power, expander efficiency, and total recovery efficiency increased with a growing expansion ratio between 2 and 6. Finally, enlarging the clearance volume negatively affects the RC system, decreasing output power and efficiencies.

In the first of two studies in 2017, Di Battista et al. implemented an axial single stage turbine and a finned coil HEX in an RC WHR system installed on the exhaust of an IVECO N67 engine operating at various loading conditions with water as a working fluid [168]. The turbine yielded an electrical power of 2.5 kW; however, transient operation and thermal states (i.e., level of superheating, turbine inlet conditions) caused concern regarding the turbine's performance.

Thus, centripetal radial turbines were recommended for further applications. Moreover, an overall conversion efficiency of 40% was achieved, with nearly 60% of the mechanical power lost, necessitating conversion efficiency improvements. Furthermore, regeneration increased the cycle efficiency on the order of 10-15%, while reducing exhausted heat by 15%, subsequently resulting in net unit efficiencies of 2.5-3.0%.

Next, Di Battista et al. explored evaporator and condenser sizing for an RC WHR system from exhaust gases of a CI engine [169]. Using a previously developed model, they added the heat transfer analysis of a shell-and-tube evaporator and a radiator condenser to minimize size and weight for an on-board application [170]. Ultimately, size and frontal area occupation were the primary design limitations for the condenser. However, the sizing of the evaporator incurred additional consideration due to the detrimental engine back pressure; thus, the maximum allowed pressure drop became the dominant constraint, generating a weight and power trade-off. Through the authors' design, the RC recovered 2-5% of engine brake power for a net power recovery of 1%.

Addressing the issue of sensitivity between working fluids and RC design variables, Cignitti et al. in 2017 developed a simultaneous working fluid and system design approach for RC WHR from the exhaust of a 37 MW marine CI engine [171]. Using this approach and a fixed pinch point, the optimal working fluid was 2,2,3,3,4,4,5,5-octafluorohexane, which has no ODP potential and a low GWP, with a net power output of 1.2 MW. Furthermore, by applying the simultaneous approach with an optimization strategy bound by the product of the overall heat transfer coefficient and heat transfer area (based on the positive correlation between UA and

W_{net}), the optimal working fluid was 5-chloro-4,5,5-trifluoro-2,3-dimethylpent-2-ene with a net power output of 1.25 MW.

The same year, Xu et al. devised detailed models capable of effectively simulating RC and engine performance under transient operating conditions for exhaust and EGR WHR via two parallel shell-and-tube evaporators with helically coiled tubes, an expander with an integrated generator, and ethanol as a working fluid [172]. Using Simulink, the RC was modeled through expressions for detailed heat transfer coefficients and the pressure drops across the HEXs, while the engine model for a HD CI engine was developed in GT-POWER. Subsequently, their models producing mean errors of 2% and 3% for vapor temperatures and pressures, respectively, for a constant speed, variable load RC. Moreover, they state that their predictive model can be used to aid in the development of transient RC WHR control systems.

In 2017, Preißinger et al. carried out a comprehensive sweep of working fluids and compared their performance in an RC WHR system for passenger cars and HD trucks [173]. Their simulation tool in MATLAB, in conjunction with thermodynamic working fluid data, enabled the authors to evaluate over 3,000 different working fluid candidates. By ranking them on their RC performance, and eliminating options due to toxicity and safety concerns, the top five working fluids were ethanol, hexamethyl-disiloxane, R152, 1,3-difluoro-benzene, and 1-propanol. While ethanol was the best overall working fluid, hexamethyl-disiloxane performed well at higher condensation temperatures, and R152 was well suited for lower condensation temperatures. Overall, RC configuration and the condensing temperature were the most influential parameters.

Similar to Tian et al. earlier in the year, Hou et al. researched the performance of a FPLG with different cam plates and valve timings for the application of an RC WHR system using compressed air as the working fluid [174]. For an intake pressure of 2.0 bar and an operating frequency of 2.5 Hz, a maximum power of 19 W was achieved. However, the maximum indicated efficiency of 92.8% was at 1.4 bar and 2.0 Hz. Thus, as intake pressure grew, the peak power output of the FPLG increased, while the indicated efficiency decreased.

Before proposing a novel RC system in 2017, Zhou et al. reviewed RC WHR systems for passenger vehicle applications [175]. Although the exhaust gas has a higher exergy potential than the engine coolant, many researchers utilized both sources with dual loops. For working fluid selection, at high-temperature conditions, water was better suited than organic fluids, which performed better under low-temperature conditions. Expander selection was crucial as well, with scroll expanders the ideal option due to their compactness and cost-effectiveness. Finally, Zhou proposed an RC system that utilized the power electronics of a hybrid vehicle as an additional heat source for WHR. Based on RC simulations using R245fa as a working fluid, the use of the electronics heat source improved the expander power output by 58% and the coefficient of performance (i.e., the ratio of expander work output to pump work input) by 20%.

After detailing other types of WHR systems and identifying RC as the most promising, Lion et al. provided a comprehensive review of the various aspects of RC design in 2017 such as working fluid selection, component selection, system architecture design, and system modeling [176]. In regards to heat sources, Lion et al. determined that exhaust gas and EGR were largely used, often in parallel configuration. Furthermore, larger engines, such as in marine applications,

also used the coolant as a heat source. Vehicle applications in literature included passenger vehicles, but focused on long-haul truckers utilizing water and ethanol as the working fluids. Additional working fluid options and system components were presented, with generalized guidelines for selection criteria. Ultimately, in all RC applications, the primary obstacles facing the technology include packaging issues, thermal management issues, safety, cost, and reliability.

The next year, based on a methodology that calculated equivalent temperatures for the evaporator and condenser of a basic RC system, Saloux et al. reconstructed and expanded their procedure to estimate the values of the actual temperatures at each state within the cycle and select potential working fluids through the variation of mass flow rates and isentropic efficiencies [177]. The reconstruction methodology first evaluated the RC performance without consideration of the working fluids, achieving RC cycle efficiencies of 9.9-10.5%. With the same RC performance for four working fluids compared, determining the best working fluid was difficult; however, the methodology proposed allowed for a more direct comparison of the feasibility of working fluids.

In 2018, Yang et al. used the experimental performance of a hydraulic diaphragm metering pump to estimate its influence on RC WHR behavior using R123 as a working fluid [178]. Subsequently, the mass flow rate of the pump was independent of pressure; whereas, the actual pump efficiency increased nonlinearly with outlet pressure. Furthermore, a maximum pump efficiency of 88.27% was obtained for an outlet pressure of 1.33 MPa and a mass flow rate of 2.06 ton/hr. As the outlet pressure increased, the power input of the pump also rose from 207.12 W to 523.91 W. Moreover, the RC system consistently achieved thermal efficiencies over 10%

for pump strokes from 25-100% and both the thermal efficiency and net power output grew as the evaporating temperature increased.

Sarkar in 2018 presented a design methodology for an RC WHR system that simultaneously predicts the location of the evaporator and condenser pinch points and optimizes the pressures [179]. Of the seven considered working fluids, R1233zd and isopentane achieved the highest working fluid mass flow rates, and subsequently the greatest net work output. However, ammonia yielded the largest thermal efficiency. Yet, due to its improved work output, as well as its better safety considerations when compared to ammonia and isopentane, R1233zd was chosen as the best working fluid considered.

The same year, Negash et al. attempted to experimentally optimize an RC system configuration for WHR from multiple heat sources from a construction equipment engine with R245fa and R123 [180]. In addition to exhaust gas, EGR, and engine coolant as waste heat sources, the addition of a recuperator and the use of the engine's hydraulic oil as a heat source with and without a recuperator were considered. The configuration utilizing the hydraulic oil as a heat source without a recuperator displayed the best performance, improving the net power output by 11.1% at half-load, while the use of a recuperator alone enhanced engine performance by 16.3% and 36.9% at half- and full-loads. However, the use of both a recuperator and the hydraulic oil significantly increased costs by 39% and 49%, respectively. R134a yielded a 4% net higher power output than R245fa, with the added benefit of smaller expanders and HEXs due to a greater operating pressure.

Using a bottoming RC configuration in 2018, Zhao et al. implemented a new control method for a modified engine and RC for better response to engine operation variation [181]. While the engine operation was modeled in GT-SUITE, MATLAB and Simulink were used to simulate the RC system with R245fa as a working fluid, a shell-and-tube evaporator, and a plate type condenser. Integrating the two models allowed for adjustment of the RC parameters according to changing engine operating parameters. Subsequently, 2.54 kW was obtained as the maximum net power output of the system, with a thermal efficiency of the engine and RC of 3.57%, while reducing the BSFC of the engine by 9.69 g/kWh.

Also in 2018, Chintala et al. compiled a review of RC for WHR from CI engines and their design challenges [18]. Engine exhaust and engine coolant are the two most utilized waste heat sources and with a CRC or DRC, both sources can be effectively harnessed simultaneously. Furthermore, the evaporators used in each loop should be designed for the appropriate heat source, especially in the case of the variable exhaust gas waste heat and on-board applications. Moreover, scroll expanders present the best performance and economic considerations of expander technologies. Although RCs achieved only 10-25% standalone efficiencies, they still present an opportunity for combined RC and engine efficiencies between 60-90%. Smaller engines may not be as ideal for RC applications due to their lower mass flow rates, while high capacity, multi-cylinder engines are ideal. In comparing working fluids, R245fa was selected as the most thermally and environmentally attractive working fluid, followed by R141b and R123.

Garcia et al. explored the different cycles used in low- and medium-grade WHR in 2018, including BRC, RRC, CRC, organic flash cycles, and trilateral cycles, subsequently comparing

them as a function of their efficiencies [182]. Based on efficiency values from the literature, the RC configurations achieved cycle efficiencies between 5-10%, while trilateral cycles achieved efficiencies between 30-50%. Furthermore, the topping and bottoming temperatures in the proposed trilateral cycles were significantly lower than the RCs, which further improved the thermodynamic performance of trilateral cycles over RCs.

Finally, in 2018 Imran et al. conducted a bibliometric quantification of the trends in RC technology research, primarily comparing authorship and originating countries, but including research technology trends as well [36]. Of the core research areas of RCs (i.e., applications, working fluids, expander technology, cycle configuration, design and optimization, and dynamics and control), 42.15% of RC publications are on RC applications, followed by design and optimization. Furthermore, of RC technology applications, 37.81% of the articles are about RC for waste heat applications. Transcritical cycles were the most studied cycles, followed by cycle configuration comparisons, and then regenerative cycles. Moreover, for the research articles on RC design and optimization, 67.88% of the articles were focused on optimization rather than design, and for those on working fluids, 27.57% were about working fluid selection. Finally, of the articles focused on expander selection, 63.6% discussed turbine expanders, followed by scroll expanders. Between 2009 and 2016, the number of papers published on RC has compounded significantly, showing increasing interest in the field. The bibliometric approach used by Imran et al. not only provides nominal information about the research focus trends in the field of RC technology, but also displays the increasing popularity of the subject in research.

2.2.3 Recent Literature Review Summary

Between 2012 and 2018, a tremendous number of researchers published work on RCs for WHR, building on the extensive research catalog for the decades prior, in response to progressively rigorous fuel economy and emissions regulations. However, the contemporary research did little to contradict the trends seen in previous reviews, but rather strengthened them, while adding specificity, volume, and weight. This shoring of RC WHR research is seen in the presented review of work on cycle configurations and comparisons, working fluid and component selection and sizing, applications, heat sources utilized, and performance and economic considerations.

Despite the predominance of RCs as the power cycle used in WHR efforts, RC WHR was still compared or coupled to other WHR technologies and cycles, such as TEGs, BCs, transcritical power cycles, and trilateral cycles. Furthermore, RCs were combined with refrigeration cycles to expand operational applications [66, 163]. Oftentimes, the performance elevation over standard RCs was not justifiable given the further costs and complexities incurred, as in the case of the combined TEG-RC and the Brayton air cycle with isothermal compression [24, 74].

More prevalent was the comparison of different configurations of an RC cycle. These modifications included regeneration, preheat, the use of intermediate thermal cycles, TRC, DRC, and CRC. Aside from single RC systems, DRC, CRC, or other combined cycles were the most frequent, allowing for the utilization and optimization of multiple waste heat sources for improved combined performance. Cycles employing both preheat and regeneration performed

better than standard cycles, regardless of the base configuration, yielding higher thermal and cycle efficiencies and net power output, by as much as 27% [25, 27, 99, 120, 128]. Nonetheless, as with more complex cycles, the inclusion of supplementary HEXs increased system size and cost. Thus, the consequences of the trade-off between system performance and cost are further emphasized.

By far the most commonly studied parameter in RC WHR literature was working fluid selection, often considered in addition to cycle types or configurations, as the appropriate working fluid depends on the cycle type and heat source. The main selection criteria for working fluids were thermodynamic performance, economic considerations, safety, and environmental factors. In assessing optimal working fluid performance, compromises must be made between thermodynamic performance and economic considerations, primarily due to the effect that the working fluid has on component sizing [33, 99, 109]. Furthermore, the most environmentally sound or the safest working fluid rarely exhibits the best performance, indicating yet another concession [18, 71, 179]. Additionally, selection of the appropriate working fluid depends on the working conditions and should be concurrently considered with expander options [26].

As in the literature prior to 2012, there was no single working fluid consistently exhibiting ideal performance. Nonetheless, there were several working fluids predominantly used in studies, consistently outperforming other working fluids. The most prevalently used working fluid was R245fa, with advantageous operation in low temperature systems. Conversely, with ideal performance exhibited in high temperature systems, water was the next predominant working fluid. Furthermore, R123, ethanol, R134a, and toluene also frequently appeared in the literature. Finally, working fluid mixtures were widely studied, indicating improved performance over pure working fluids while allowing for a wider spectrum of applications and working conditions [89,

100, 146]. However, mixtures are still subject to additional concerns, such as augmented thermodynamic performance bettering economic performance while negatively influencing pumping and component requirements [149, 151].

Regarding component selection, as before, the expander was the most crucial, as it was the largest source of losses and costs within a WHR system [26, 87, 107, 113, 140]. Nevertheless, the expander also presented one of the largest opportunities for advancing RC system performance, with drastic enhancements in net power output possible through comparatively minor growth in expander efficiency; thus, this indicates the need to focus on expander technology upgrades in the future [134]. Of the utilized expander types, scroll expanders were the most frequent due to their high efficiencies, followed by screw then swash-plate expanders. Notably, expansion valves or nozzles were often used in experimental set-ups to mimic the inclusion of an expander, with authors using available expander efficiencies from the literature to then calculate system performance. Furthermore, FP expanders were introduced as a novel technology, displaying comparable performance and elevated efficiencies, but requiring further study for actual RC WHR implementation [80, 135, 174].

Expanding the focus of component design and selection beyond just the expander, the literature between 2012 and 2018 also concentrated significantly on HEX design. HEX types, sizes, and flow orientation were all considered as pathways for improving RC WHR performance. Through the design and optimization of HEXs for the specific RC application and heat source, not only can system performance and waste heat utilization be improved, but system costs and induced backpressure (when using engine exhaust) can be reduced [70, 150, 155]. The most common types of HEXs were shell-and-tube and plate HEXs, appearing with the same frequency, although plate heat exchangers were often considered superior due to their more

compact design [59]. Conversely, although their selection is important due to the potential for high losses, pumps were not as acutely considered, with diaphragm pumps commonly deemed appropriate for RC WHR applications [59, 87, 113].

Also building on the historical literature, tremendous consideration was given to the comparison of heat sources for WHR. Engine exhaust was the most ubiquitous source of waste heat due to its high temperature and quality, ease of implementation, and reduced costs [26, 32, 96]. Other prevailing heat sources included coolant, EGR, and varying complexities of their combinations. Notably, in dual or cascaded cycles, the coolant and the exhaust together were the most common and effective heat sources. However, selection of the best heat source or combination of heat sources depended on the engine load, as well as the specific power cycle being utilized [57, 142]. Moreover, intermediate thermal cycles between the heat source and the RC working fluid were implemented to mitigate variations in the heat source temperature and improve control [110, 117, 131, 133].

The most common application for RC studies was automotive CI engines, such as heavy-duty trucks or buses, followed by marine CI engines on ships, both traditional and hybridized SI engines in passenger vehicles, and power plant applications. For automotive applications on both SI and CI engines, the aforementioned trade-offs between performance, working fluid selection, and component sizing became especially important for fitting the WHR system on-board a vehicle. Conversely, system cost and economic considerations were primarily more important for marine and power plant applications due to the lessened size restrictions. Consistent with previous conclusions, the use of a hybridized powertrain in automotive applications yielded an ideal conversion and storage mechanism for the recovered power, while also allowing for more consistent RC operation with engine variability [26, 55, 58, 62, 63, 67].

Additional attention was also given to transient operation, as well as operation over driving cycles, in order to assess more realistic performance parameters. However, the general trends between steady and transient analysis were similar; thus, this allows the simpler, steady analysis to be exploited as an initial assessment [118]. Furthermore, more concern was placed on control strategies for RC systems, in order to address variability in operation based on driving profiles and engine loads. Proposed strategies included dynamic, combined, minimized variance, and non-linear transient control [75, 86, 91].

With such a wide range of cycles, components, working fluids, and applications studied, the modeled or experimental performance parameters are difficult to compare. However, generalized thermal efficiencies for RCs between 5-51.27% were achieved, with system efficiencies (i.e., including the engine or waste heat source) between 3.63-43.8%. Moreover, power improvements between 2.1-23.7% were achieved, for fuel economy savings of 2.7-30% in automotive applications. These generalized performance values indicate a betterment over similar values achieved prior to 2012, suggesting a progression in technology and optimization in RC WHR. Unfortunately, economic parameters depend greatly on the application, and as such are even more complex to compare. However, the following trends were seen: escalating system complexity resulted in rising system costs, working fluid selection affected electricity production costs and the payback period, and growing component efficiencies elevated expenses.

2.3 Conclusion

Despite the introduction and comparison of many different types of WHR, RC remained the dominant method of WHR for various applications between 1973 and 2018. As the field

advanced, dual or cascaded RCs became prevalent, in addition to preheaters or regenerators to improve system efficiency and performance. However, the introduction of these complexities and additional system components comes at the expense of inflating system costs. Working fluid selection remains the prominent parameter of RC WHR. Water and R123 have consistently been selected as working fluids throughout the research due to their enhanced performance and safety, but since 2012, R245fa has become progressively prevalent due to its elevated environmental characteristics.

Expander selection continues to be a crucial component, with direct relationships between expander efficiency and RC thermal efficiency. In recent years, the design and sizing of the HEXs utilized within the cycle have become competitively essential in bettering thermal efficiencies, especially in on-board applications where sizing is paramount or in variable waste heat source applications where the heat transfer must be maximized. Also, more directly considered in recent years were waste heat sources. Although the exhaust alone is remarkably popular due to its high temperature and simplicity, for exceedingly complex systems the coolant and the exhaust is the preeminent heat source combination.

Holding true to the historical summary, automotive CI engines are the primary applications of RC WHR, with specific emphasis placed on heavy-duty trucks and passenger vehicles. A hybridized powertrain, specifically for SI engines, has become a widely accepted method of successfully converting and storing energy for on-board RC WHR systems. As the research in the field expanded, the achieved performance values from models and experiments also developed, outperforming previous studies. The biggest areas for advancement in RC WHR lie in the expander and HEXs, as well as in the working fluid selection. However, despite the progressions seen in the various aspects of RC design, the strongest trend seen is that the system

must be designed and optimized for its specific application in order to achieve maximum thermodynamic and economic performance, with literature trends providing a strong background and methodology.

Chapter 3: WHR & DPFHX Experiments

3.1 Introduction

The primary focus of this WHR research effort was a shell-and-tube HEX for experimental assessment as the evaporator in an RC WHR system with the exhaust of a single-cylinder CI engine as the waste heat source. In focusing on the HEX component, there were two concepts to be assessed: (1) the experimental performance of a combined DPFHX using an existing apparatus and (2) experimental working fluid performance comparisons in the HEX on hand. Thus, the experimental objectives were to determine if the combined DPFHX would allow for enhanced operation as a HEX evaporator in an RC WHR system and comparing the performance of multiple working fluids within the device with and without DPF cores installed. Parameters such as heat transfer rates (experimental parameters), HEX effectiveness and the overall HEX heat transfer coefficient (HEX parameters), in conjunction with the flows' Nusselt numbers and convection heat transfer coefficients (convective heat transfer parameters), were used to quantitatively assess apparatus and working fluid performance.

Consequently, this chapter describes the methodology and equipment for the WHR HEX and DPFHX experiments, the results obtained, and the associated analysis. With this in mind, the first round of experiments employed the HEX without DPF cores, exercising only water as the working fluid, as validation of the apparatus' performance after several years out of operation via direct comparison to its' previous performance. Next, several different heat recovery working fluids were investigated and compared via the aforementioned parameters. From these comparisons, the two working fluids providing the largest values for the experimental and

analytical parameters were then considered in the ensuing DPFHX experiments, with their resulting parameters being compared once again. Thus, based on experimental results and evaluation of experimental, HEX, and convective heat transfer parameters, comparisons and conclusions could be formed regarding the operation of the DPFHX apparatus compared to the WHR HEX, as well as regarding the performance of various working fluids within the devices.

3.2 WHR Apparatus, Data Collection/Processing, and Calculations

The equipment in the WHR experiments, shown in Figure 3.1, can be grouped in four categories: single-cylinder test engine, WHR apparatus, associated NI LabVIEW code for data collection, and working fluid. The specifications for the Yanmar L100V single-cylinder CI engine (Figure 3.1a) used for testing can be found in Langness et al. [183]. The remaining components will be discussed subsequently, followed by the procedure for post-testing data processing and the methodology for obtaining the required parameters that will be used to evaluate the performance of the apparatus. Then, the criteria and process for working fluid selection will be covered in detail.

The experiments were conducted as five-minute trials, with three trials per working fluid (aside from the first experiment in which only two trials were run). The data obtained for each trial were averaged over the five-minute trial time span in which the engine and WHR apparatus were both operating under steady-state conditions. This occurred when the change in oil and exhaust temperatures of the engine along with the change in working fluid and exhaust temperatures in the HEX were all less than one percent over the course of 60 seconds (i.e., the engine and the apparatus were both maintaining steady temperatures), determined via monitoring the temperatures of interest throughout the warm-up period. In order to ensure that these metrics

were achieved, the engine and WHR apparatus were run for approximately 30 minutes prior to capturing any experimental data, also allowing enough time for the apparatus itself to achieve steady-state (i.e., beyond the time frame indicated by the transient conduction calculations shown in Appendix A).

During testing, the Yanmar engine operated between -0.5 N·m to 0.3 N·m at a speed of 1800 RPM, with the injection of diesel fuel occurring from 0.060 g/s to 0.065 g/s. In order for the working fluids within the HEX to stay a liquid and prevent boiling, the engine had to remain at extremely low loads (i.e., 0.0 Nm ± 2.5%) to limit the temperature of the exhaust. However, since the dynamometer maintains the engine at a set speed, in conjunction with cyclic variation, the loading varies and becomes negative at times when the dynamometer prevents the engine from increasing speed. Nonetheless, the engine and exhaust temperatures remain steady, despite these cyclic variations. Moreover, although engine operation is pulsed flow, by averaging the data over the entire trial, the flow effectively becomes steady. Furthermore, the pump was operated using a 20 mA signal via the data acquisition (DAQ) program (described subsequently) for each trial, corresponding to the maximum rate of fluid circulation for the pump and the maximum flow rate for each working fluid.

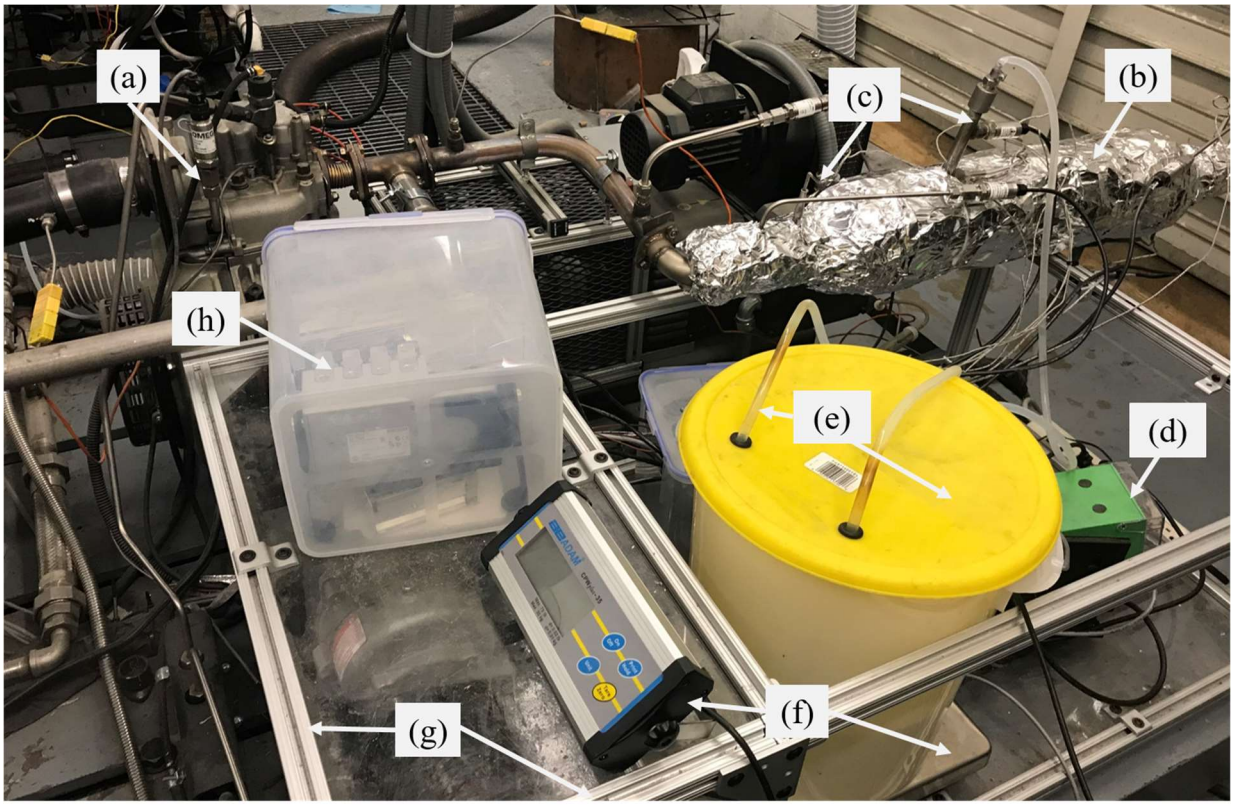

Figure 3.1: WHR apparatus components: (a) Yanmar single-cylinder engine; (b) shell-and-tube HEX wrapped in thermal insulation and tape; (c) thermocouples, pressure transducers, and their respective fixtures for the exhaust and working fluid; (d) Grundfos diaphragm pump; (e) polyethelene bucket and high temperature silicone tubing; (f) Adams bench scale and digital display; (g) aluminum T-slotted extrusions and polycarbonate sheeting; and (h) NI CompactDAQ.

The primary component of the WHR apparatus was the HEX connected to the exhaust of the engine, directly responsible for extracting the thermal energy. In this case, it was a single pass, shell-and-tube design provided by SEC Heat Exchangers (Figure 3.1b). This stainless steel HEX contains six 19.05 mm inner diameter and 22.23 mm outer diameter tubes within the shell, which was previously determined to provide an adequate heat transfer area for the Yanmar engine's exhaust energy [184]. For the DPFHX experiments, cordierite DPF cores were installed within

the tubes of the HEX.

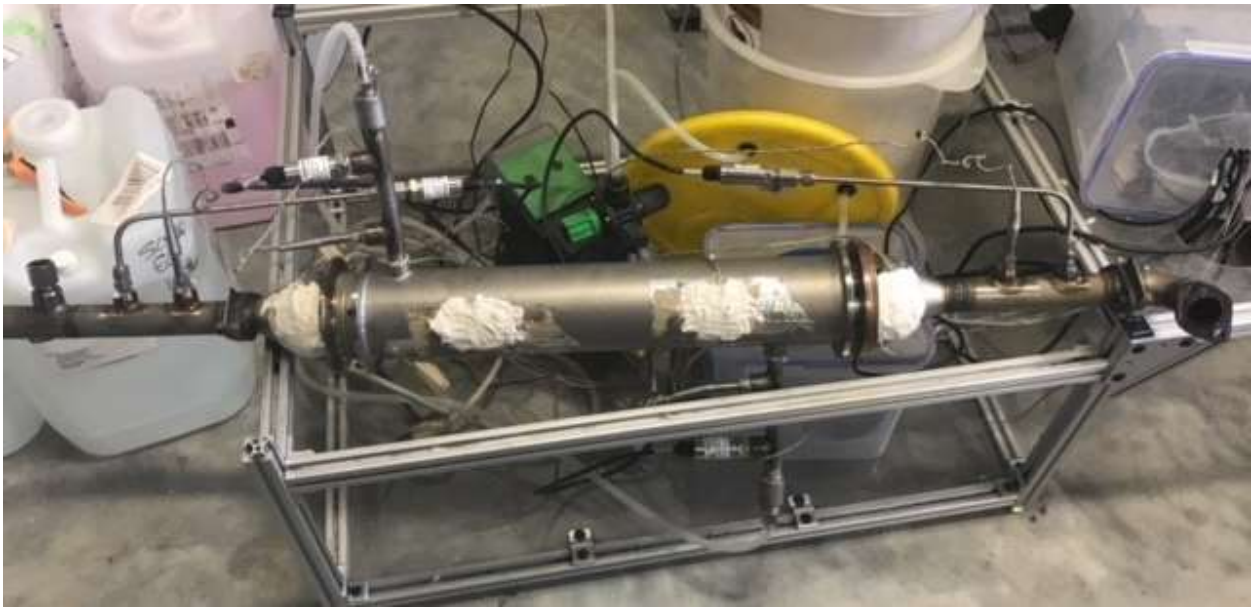

Figure 3.2: The uninsulated HEX with mounted thermocouples, pressure transducers, and Type-K thermocouples. Note that although the HEX is in a counterflow configuration in this photo, a parallel configuration was used for experimental testing.

Added to the inlet and outlet of the HEX tube bundle were 76.20 mm to 25.40 mm reducers, to which additional piping was secured for the mounting of thermocouples and pressure transducers in the exhaust gas stream. Moreover, fixtures placed at the top and bottom of the shell provided the mountings for thermocouples and pressure transducers for the inlet and outlet working fluid streams, all of which are shown in Figure 3.2. The thermocouples and pressure transducers were both from Omega, products TC-J-NPT-G-72 (accuracy ± 0.75% K) and PX309-030AV (accuracy ± 0.25% psi), respectively. Furthermore, four Omega type K thermocouples, product SAI-K-SRTC (accuracy ±0.75% K), were affixed to the shell exterior to monitor the external HEX temperature, secured underneath the white high temperature cement in Figure 3.2. Finally, based on findings from previous testing, to prevent the loss of thermal energy

to the surroundings the HEX was wrapped in 25.40 mm thick, ceramic fiber thermal insulation from Tao Fibre and an outer layer of thermal tape (Figure 3.1b) [20].

The next element of the apparatus was the pump, which transports the working fluid through the shell side of the HEX. A Grundfos positive displacement diaphragm digital dosing pump (Figure 3.1d), product DDA 30-4 AR-PP/E/C-F-31U7U7BG (accuracy ±1%), connected to the working fluid inlet via high temperature silicone tubing (Figure 3.1e), was controlled utilizing a 4-20 mA signal, corresponding to a maximum flow rate of 30 L/hr for pressures up to 4 bar. Moreover, the working fluid moved to and from two NSF-certified polyethylene buckets (Figure 3.1e), serving as reservoirs, with stainless steel as the material for any additional fittings or clamps.

The final two pieces were the weight scale and the modular mount for the apparatus. An Adam bench scale with a digital display (Figure 3.1f), product CPWplus 35 (accuracy ± 0.01 kg), provided data for the working fluid flow rate based on measurements of the inlet reservoir bucket weight. Furthermore, a mounting structure for the HEX was constructed out of 25.40 mm aluminum T-slotted extrusions and impact resistant polycarbonate sheeting (Figure 3.1g). This structure was designed to fit in the pad space available in the test cell while allowing slight modifications to align the HEX with the exhaust pipe.

Rivaling in importance to the physical machinery was the DAQ program responsible for reading and logging all experimental data; thus, a LabVIEW code was created specifically for the WHR apparatus. The WHR LabVIEW code ran a 4-slot National Instruments (NI) CompactDAQ (Figure 3.1h) connected via a USB cable to a computer outfitted with NI DAQmx.

Specifically, the modules in the CompactDAQ were: NI 9211, a thermocouple input module for the working fluid and exhaust temperatures; NI 9237, a simultaneous bridge module for working fluid and exhaust pressure measurements; NI 9265, for analog control of the pump via excitation from the power supply; and NI 9211, a thermocouple input module for the type K thermocouple data. Specific information regarding each module is available in [20].

Control and monitoring of the experiments were accomplished using a graphical user interface (GUI) accompanying the WHR LabVIEW code, seen in Figure 3.3. This GUI provided real-time graphical representations of the pressure and temperature measurements during the experiment. Moreover, the GUI contained controls for the excitation output to the pump, controlling the working fluid flow rate. Furthermore, this GUI continuously updated the scale reading to monitor the working fluid reservoir (via a direct VGA connector), while also providing a count of elapsed experimental time and cataloging the current time and date.

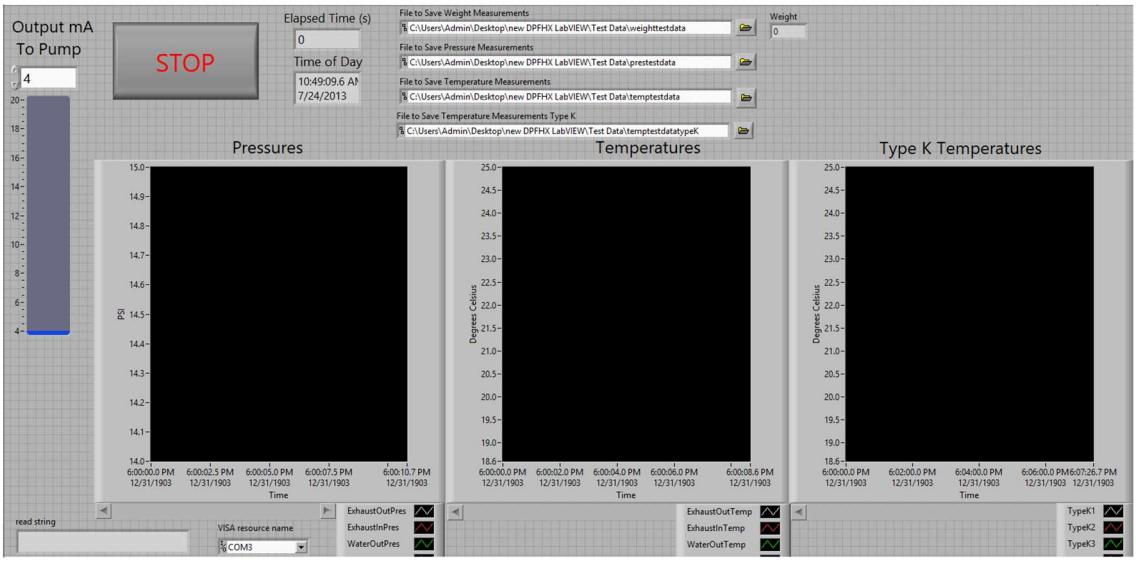

Figure 3.3: LabVIEW GUI for monitoring and running the WHR apparatus during experiments.

Additional data were recorded from the inherent DAQ program associated with the single-cylinder test engine, which runs for the entire duration of each individual experimental trial and compiles a single engine performance data file. Of this amassed data, the necessary parameters required were the air and fuel flow rates to the engine, which together equal the exhaust flow rate. Furthermore, pressure traces were taken multiple times throughout the testing to compare the influence of the HEX on engine performance with and without DPF cores installed. Extensive records of the entire instrumentation installed on the Yanmar engine can be found in [183].

During testing, the WHR LabVIEW program ran and recorded the entire time that the engine and apparatus are operating; thus, a significant amount of data processing was done post-testing in order to obtain relevant experimental data from the appropriate periods. When trials were executed, the starting time and weight of the reservoir were recorded, followed by the stopping time and weight, which were then used to filter the applicable trial data from the accumulated recorded information.

The thermocouple measurements, pressure transducer data, and weight values were output into individual technical data management solution (TDMS) files. However, only the measurement values were recorded in these files; hence, after testing, timestamps were allocated to each recorded measurement using the sampling rate of each different device to assign the data to the appropriate trial (i.e., temperature data collected every 0.333 s, pressure data every 0.6 s, weight scale data every second, and fuel and air mass flow rates every 0.1 s). Since steady state tests were conducted, the data were then simply averaged with a standard deviation calculated.

To determine the mass flow rate of the working fluid, the difference in the working fluid reservoir's weight for a trial was divided by the time of that trial (i.e., 300 s). Then, the final data needed for complete analysis was the exhaust flow rate, obtained by summing and averaging the air and fuel flow rates from the trial, with a standard deviation also calculated.

All pertinent data were then compiled into a single comprehensive Excel file, including the working fluid type, inlet and outlet temperatures and pressures for the exhaust and working fluid, and mass flow rates for the exhaust and working fluid. Subsequently, a MATLAB program, written by the author and available in Appendix B, conducted all of the necessary calculations to compute the heat transfer rate lost by the engine exhaust, the heat transfer rate to the working fluid, the effectiveness of the HEX, and the overall heat transfer coefficient.

First, the code extracted the experimental data from the Excel file, creating an input data matrix and indexing the separate trials' data into individual rows. Once the data was input into MATLAB, the first major calculation was finding the heat transfer lost from the exhaust (Q_{ex}) using the species molar flow rates ($\dot{n}_i$) and change in molar enthalpy ($\Delta\overline{h}_i$) via Eq. (3.1):

$$Q_{ex} = \sum_{i=1}^{NM} \dot{n}_i \Delta\overline{h}_i \tag{3.1}$$

with the number of species (*NM*) to be determined using a simplified combustion analysis.

Based on an assumed diesel fuel composition ($C_{14.20}H_{25.54}$), the molecular weights of the fuel and air were calculated [20]. These molecular weights, along with the experimental fuel and air

mass flow rates, provided the molar flow rates of the air and fuel accordingly. Furthermore, the fuel and air molar flow rates were used to calculate the number of air molecules needed (Z) to balance the lean combustion equation presented as follows:

$$C_{14.20}H_{25.54} + Z\left(O_2 + 3.76N_2\right) \rightarrow aCO_2 + bH_2O + cN_2 + dO_2 \tag{3.2}$$

The coefficients, *a*-*d*, on the products in Eq. (3.2) depended not only on the composition of the fuel, but also the amount of air entering the engine; thus, these values changed with varying engine operating parameters. Accordingly, the coefficients of the products multiplied by the fuel molar flow rate yielded the molar flow rates of the individual species ($\dot{n}_i$). While there were significantly more products of CI combustion, for simplification of the calculation, only the products of lean combustion presented in Eq. (3.2) were considered; hence, $NM = 4$.

Furthermore, the species' molar enthalpies ($\overline{h}_i$) were calculated via the addition of the species' heat of formation with the sensible enthalpy; i.e., the difference between the enthalpy at the species' temperature and the enthalpy at the standard reference temperature [23]. Then, the product of the change in each species' molar enthalpy and its respective molar flow rate generates the individual heat transfer values for each species, which when summed yield the overall exhaust heat transfer, as in Eq. (3.1). Notably, as discussed previously, the exhaust mas flow rate ($\dot{m}_{ex}$) was obtained by adding the fuel and air mass flow rates together via a conservation of mass balance on the engine itself.

Next, the MATLAB code calculated the heat transfer to the working fluid (Q_{wf}) by first determining the mass-based enthalpy change (Δh_{wf}) of the working fluid from its inlet and outlet temperatures. Subsequently, the heat transfer to the working fluid was obtained by multiplying the working fluid mass flow rate ($\dot{m}_{wf}$) by the enthalpy change, as such:

$$Q_{wf} = \dot{m}_{wf} \Delta h_{wf} = \dot{m}_{wf} \left(h_{wf,out} - h_{wf,in} \right) \tag{3.3}$$

For water, ethylene glycol, and propylene glycol, the enthalpy difference in Eq. (3.3) was found via interpolation of the inlet and outlet temperatures in matrices containing the enthalpy of each working fluid as a function of temperature [23, 185]. However, for the 50-50 mixture of ethylene glycol and water, the enthalpies were determined for each fluid alone as mentioned prior and then combined using mass fractions, resulting in a single enthalpy difference for the mixture, with the enthalpy of mixing considered negligible [186]. The selection procedure for these working fluids will be detailed subsequently. As indicated previously, the working fluid mass flow rate ($\dot{m}_{wf}$) was found from the measured weight difference of the working fluid reservoir over the span of a trial.

Examining the simplified energy balance equation for the HEX in Eq. (3.4), it can be seen that in an idealized situation, the heat transfer rate from the exhaust (i.e., the left hand side of the equation) would equal that gained by the working fluid (i.e., the right hand side of the equation). However, in reality there were losses in the system, thus decreasing the rate of heat transfer to the working fluid and transforming the energy balance into Eq. (3.5). This equation incorporated

Q_{loss}, a term quantifying the losses within the system, defined as the difference between the exhaust heat transfer rate and the working fluid heat transfer rate.

$$\dot{m}_{ex,in}h_{ex,in} - \dot{m}_{ex,out}h_{ex,out} = \dot{m}_{wf,out}h_{wf,out} - \dot{m}_{wf,in}h_{wf,in} \tag{3.4}$$

$$Q_{ex} = Q_{wf} + Q_{loss} \tag{3.5}$$

In addition to the heat transfer rates, an important parameter for evaluating the heat transfer through a HEX is the effectiveness (ε); i.e., how well the HEX captures the waste heat. The definition of the effectiveness is the ratio of the actual heat transfer to the maximum heat transfer possible, as such [29]:

$$\varepsilon = \frac{Q}{Q_{\max}} \tag{3.6}$$

Eq. (3.6) can be expanded to include the product of each of the respective average specific heats and mass flow rates (i.e., the average heat capacity, $\dot{m}\hat{c}_p$) and temperature differences. Thus, the effectiveness can be calculated based on the heat transfer gained by the working fluid, as in Eq. (3.7), or based on the heat transfer lost by the exhaust, as in Eq. (3.8). Applying the minimum heat capacity in the denominator of Eqs. (3.7) and (3.8) represents the maximum heat transfer possible in the HEX as indicated in Eq. (3.6).

$$\varepsilon = \frac{\dot{m}_{wf}\hat{c}_{wf}\left(T_{wf,out} - T_{wf,in}\right)}{\left(\dot{m}\hat{c}_p\right)_{\min}\left(T_{ex,in} - T_{wf,in}\right)} \tag{3.7}$$

$$\varepsilon = \frac{\dot{m}_{ex}\hat{c}_{p,ex}\left(T_{ex,in} - T_{ex,out}\right)}{\left(\dot{m}\hat{c}_p\right)_{\min}\left(T_{ex,in} - T_{wf,in}\right)} \tag{3.8}$$

Although both Eq. (3.7) and Eq. (3.8) provide valid quantifications of HEX performance, to focus the assessment on the rate of heat transfer to the working fluid, Eq. (3.7) served as the effectiveness value compared. Additionally, Eq. (3.7) presents the minimum value since, in order to balance the energy equation as indicated before, the heat transfer to the working fluid must be less than that from the exhaust. Overall, the minimum heat capacity, $\left(\dot{m}\hat{c}_p\right)_{\min}$, was that of the exhaust gas flow for all trials (i.e., $(\dot{m}\hat{c}_p)_{ex} < (\dot{m}\hat{c})_{wf}$).

Similar to the exhaust heat transfer methodology, to find the exhaust specific heat ($c_{p,ex}$), the individual exhaust species' specific heats ($c_{p,i}$) were found first, using a curve fit for the variation of the specific heat with temperature, with the assumption that the gas species behave as ideal gases, as follows [23]:

$$c_{p,i} = \frac{R_u}{M_i}\left(\alpha_i + \beta_i T + \gamma_i T^2 + \delta_i T^3 + \phi_i T^4\right) \tag{3.9}$$

The Greek coefficients are constants associated with different gas species, M_i is the molecular weight of each species, R_u is the universal gas constant, and T is the temperature of the gas in kelvin. Therefore, the inlet and outlet exhaust gas temperatures ($T_{ex,in}, T_{ex,out}$), as well as the mass fractions (Y_i) of each species, provided the basis to calculate an average specific heat

for the exhaust gas ($\hat{c}_{p,ex}$). Direct interpolation of the working fluid's specific heats at the inlet and outlet temperatures subsequently allowed for the computation of an average working fluid specific heat ($\hat{c}_{wf}$) [23, 29, 187]. Of note, specific heat data for the 50% EG and water mixture by volume was employed, as opposed to combining individual fluid data [188].

For an additional quantitative comparison between experimental results, the final calculation in the MATLAB code was the overall heat transfer coefficient (U). This value was determined based on the working fluid flow rate, average specific heat, and temperature difference, as well as the heat transfer area (A_{HT}) and the log mean temperature difference ($LMTD$) of the HEX:

$$U = \frac{\dot{m}_{wf}\hat{c}_{wf}\left(T_{wf,out} - T_{wf,in}\right)}{A_{HT}LMTD} \tag{3.10}$$

where

$$LMTD = F\left[\frac{\Delta T_a - \Delta T_b}{\ln\left(\frac{\Delta T_a}{\Delta T_b}\right)}\right] \tag{3.11}$$

The term F in Eq. (3.11) is a correction factor to account for internal flow disturbances within a HEX, used with ΔT_a and ΔT_b, temperature differences across a HEX, traditionally defined for counterflow. However, for this analysis, the HEX was idealized and treated as a concentric tube HEX in parallel flow, meaning that F is equal to 1. Thus, for this idealized HEX, the $LMTD$ was calculated for parallel flow according to:

$$\Delta T_a = T_{ex,in} - T_{wf,in} \tag{3.12}$$

$$\Delta T_b = T_{ex,out} - T_{wf,out} \tag{3.13}$$

Notably, a constant heat transfer area of 0.1915 m^2 was utilized in Eq. (3.10), calculated from the tubes' outer diameter and length. By defining the overall heat transfer coefficient in terms of the rate of heat transfer to the working fluid (i.e., the numerator of Eq. (3.10)), the resulting value provided a minimum evaluation of *U*, since the working fluid heat transfer rate was less than that of the exhaust from the discussion of Eq. (3.5). Moreover, the overall heat transfer coefficient provided an evaluation of the resistances between the exhaust and the working fluid; thus, the overall heat transfer coefficient yielded a quantitative measurement of the effect various working fluids had on the heat transfer within the HEX (i.e., which fluids provided larger resistances thus deterring heat transfer), since the exhaust flow remained generally the same across the working fluid experiments. Finally, the MATLAB code exported the heat transfer values, as well as the effectiveness and the overall heat transfer coefficient, to the original Excel spreadsheet containing the input data to provide a comprehensive table of the experimental results.

Upon completion of the data analysis, the results were evaluated and compared, allowing conclusions to be drawn about the WHR apparatus' performance. Thus, the heat transfer from the exhaust and to the working fluid, with the effectiveness and overall heat transfer coefficients, indicated the efficacy of the HEX. Furthermore, these quantitative parameters were employed to relate the ability of the working fluids and subsequently the behavior of the combined DPFHX.

3.3 Working Fluid Selection

Aside from the HEX design, working fluid selection is one of the most significant aspects influencing RC performance, as indicated in the literature review. As such, four different working fluids were experimentally tested in the WHR apparatus: water, ethylene glycol (EG), propylene glycol (PG), and a 50/50 mixture of ethylene glycol and water. However, prior to the selection of these working fluids, an extensive search and comparison of available working fluids was completed, identifying the primary criteria preferred, evaluating such criteria for an array of common working fluids, and ultimately narrowing the options down to those utilized experimentally.

While the initial criteria considered was more broadly applicable to working fluids for use within an entire RC system, the final limiting factors in the selection of working fluids arose from the given experimental setup. Due to laboratory limitations, it is not currently possible to implement a complete RC system. Additionally, the HEX is the main component to be merged with traditional aftertreatment systems for on-board WHR. As a result, the focus of the final working fluid selection criteria and subsequent experimental efforts was the optimization of only the HEX portion of the RC system. Hence, the trends and results from these experimental tests provide a direct indication of the influence of working fluid behavior regarding the entrance of thermal energy into an RC system, a vital first step for WHR operation and optimization in the future.

Thermal properties were the customary starting point for finding viable working fluids, significantly motivated by the perceived shortcomings of water as a working fluid based on the

experimental efforts of Sprouse [20]. Primarily, the relatively low boiling point of water meant that at moderately high engine loads, the water in the HEX experienced boiling due to the temperature of the exhaust gas [20]. While boiling is ideal for actual RC operation (i.e., enhancing heat transfer while preventing expander damage due to liquid droplets), this phase change significantly confounds the heat transfer analysis of the HEX as it cannot be experimentally validated easily, an unwanted complication (i.e., the quality of the working fluid exiting the HEX cannot be experimentally determined if boiling occurs). Furthermore, fluids with higher boiling points generally have greater efficiencies given the same pressure conditions [47, 49]. Thus, although in traditional WHR systems, a lower boiling point would be advantageous, since boiling could be achieved more easily, experimental limitations of the apparatus require a higher boiling point, providing some potential benefits within the HEX. Subsequently, the primary considered thermal property of a working fluid was to have a boiling point higher than that of water, as a precaution to prevent the working fluids from boiling in the HEX.

After the boiling point, additional deliberation stemmed from an understanding of the preferred attributes of working fluids for a HEX evaporator in an RC. Specific thermal criteria for this application are as follows [17, 46]: low specific heat, low viscosity, high latent heat of vaporization, high thermal conductivity, and low specific volume. With a low specific heat and high thermal conductivity, the thermal diffusivity of the working fluid is larger, subsequently allowing the fluid to respond more quickly to thermal changes, which, although less important for steady state operation, can carry considerable weight for transient operation; while a reduced specific volume (i.e., greater density) minimizes the required size of the components.

Furthermore, a small viscosity, in conjunction with a high latent heat of vaporization and large thermal conductivity, minimizes the pressure drop of the fluid across the HEX while maximizing heat transfer [29, 35, 46]. However, the latent heat of vaporization was not strongly considered since the fluids will not be experiencing boiling; nonetheless, it is included here for completeness regarding the ultimate application of this HEX. Hence, these thermal attributes were secondary standards for potential working fluids, with the intention of improving HEX performance through the appropriate selection. Moreover, safety considerations were used to exclude several working fluids, such as hydrocarbons, even if they possessed the necessary thermal traits.

Beyond thermal and safety considerations, other miscellaneous topics also required attention, the first being limitations of other components in the WHR apparatus, primarily the pump. Per the pump's mechanical data sheet, the maximum viscosity the pump is capable of handling is 150 cP; thereby, eliminating fluids with higher viscosities (e.g., glycerin). Moreover, in order to obtain a diverse spread of data without running an excessive amount of testing, working fluids with a diverse range of properties, such as the Prandtl number, were desired. The Prandtl number was specifically targeted since it is calculated using several thermal properties of focus (i.e., specific heat, thermal conductivity, viscosity, and thermal diffusivity). Furthermore, concerns regarding corrosiveness and compatibility between the working fluid and the apparatus materials were addressed. The WHR apparatus is an open system, making the use of a gaseous working fluid nearly impossible. Finally, commercial availability was considered in order to minimize purchasing costs. Such practical considerations, in conjunction with previously declared criteria, were subsequently applied to further narrow the scope of working fluids.

The initial survey of working fluids considered 43 different options: ethylene glycol, propylene glycol, water, fluorine, acetone, propyl alcohol, R-114, isobutane, n-pentane, HFE301, R-123, propane, R-11, R-113, R227ea, benzene, toluene, p-xylene, octamethyltrisiloxane, ethylbenzene, propylbenzne, butylbenzene, butane, hexane, cyclopentane, R245fa, R32, R245, R152a, ammonia, R236ea, R22, R143a, R124, R142b, R236fa, R290, R600a, butane, and isobutene. A review of prior working fluids for WHR, primarily via an RC, as well as working fluids for general application in HEXs, generated this list of potential working fluids. A few of these were eliminated due to low boiling points. The remaining 30 were then compared based on their Prandtl number, boiling point, and viscosity. A direct comparison of these three key properties allowed for the exclusion of some working fluids while ensuring that each property fell within the desired range. Table 3.1 displays the seven remaining options for the WHR experiments and their respective properties at 300 K, representative of their properties near room temperature, and at 350 K, indicative of the direction their properties will be altered during operation as a WHR working fluid.

Table 3.1: Working fluids considered for WHR experimentation and their considered parameters (evaluated at 300 K and 350 K where applicable) [29, 185].

Working Fluid	Evaluated Temperature [K]	Boiling Point [K]	Density [kg/m^3]	Viscosity [$Ns/m^2 \cdot 10^2$]	Specific Heat [kJ/kgK]	Thermal Conductivity [W/mK]	Prandtl Number [-]
Ethanol	300	351.39	782.83	0.105	2.596	0.165	16.50
	350	-	737.80	0.045	3.169	0.154	9.29
Ethylbenzene	300	409.32	861.77	0.061	1.756	0.127	8.48
	350	-	817.94	0.037	1.925	0.116	6.20
Ethylene Glycol	300	470.59	1108.50	1.571	2.415	0.259	146.60
	350	-	1073.05	0.335	2.637	0.255	34.56
Propyl Alcohol	300	370.19	798.13	0.186	2.412	0.154	29.07
	350	-	755.07	0.065	2.999	0.142	13.75
Propylene Glycol	300	460.41	1031.29	3.590	2.513	0.203	445.01
	350	-	992.26	0.385	2.820	0.195	55.74
Toluene	300	383.75	860.44	0.054	1.707	0.130	7.09
	350	-	812.90	0.033	1.878	0.116	5.29
Water	300	373.15	996.51	0.085	4.180	0.610	5.85
	350	-	973.70	0.037	4.197	0.668	2.31

Water was the principal working fluid of Sprouse [20]; thus, for consistency, it was maintained as one of the working fluids. Moreover, this provided a benchmark to compare the performance of other fluids; hence, the other options were related to water. Both propyl alcohol and ethanol have boiling points that are lower than that of water, precluding them from consideration. In other words, choosing propyl alcohol or ethanol as the working fluid would require the engine to be run at a lower load to prevent exhaust temperatures from reaching the boiling points of these species; thus, eliminating similarities in testing conditions. All of the

working fluids possess higher Prandtl numbers than water while displaying an appropriate spread of values. Notably, toluene and ethylbenzene have Prandtl numbers relatively similar to that of water at room temperature and propylene glycol has the highest for both temperatures. In addition to a vast range of viscosities, all remaining working fluid options have viscosities well within the maximum limit of 150 cP (i.e., 0.15 Ns/m^2) specified by the pump manufacturer. However, as a hydrocarbon, toluene is extremely unattractive and unsafe as a working fluid. Furthermore, ethylbenzene, aside from being highly flammable as well as a hydrocarbon, is also expensive to purchase. Thus, ethylbenzene and toluene were both eliminated from consideration.

Now, with a majority of the working fluids rejected, the remaining options in consideration, ethylene glycol and propylene glycol, were directly compared to water on a thermal property basis ensuring that they would maintain their appeal even with a temperature increase. Specifically:

- Ethylene glycol and propylene glycol both have lower specific heats than water.
- Ethylene glycol and propylene glycol both have higher viscosities than water, but they do allow for a wider range of Prandtl numbers as desired.
- For the criteria of high thermal conductivity, both have values lower than that of water, but they also have higher boiling points.
- Both fluids have greater densities than water, meaning they have lower specific volumes.

Thus, with lower specific heats and higher boiling points, while also expanding the Prandtl number range and minimizing the specific volume, both ethylene and propylene glycol present

competitive thermal traits to those of water. It is also important to note that ethylene glycol is identified as a hazardous substance with a Category 4 acute oral toxicity, while propylene glycol is not classified as hazardous [189, 190]. This difference in categorization simply means that additional caution must be taken when handling the ethylene glycol to avoid ingestion, but does not warrant concern regarding its implementation as a working fluid.

Ultimately, ethylene glycol and propylene glycol are both attractive working fluids considering their safety and WHR apparatus compatibility while being generally thermally favorable in comparison to water, making them prime candidates for experimental testing. Furthermore, in order to expand the data collected, additional consideration was given to the two selected working fluids in order to determine which would be more appropriate for a 50% by volume mixture with water, as mixtures display increasing popularity and enhanced performance in RC applications. Hence, as apparent in Table 3.2, ethylene glycol possessed better thermal characteristics when combined with water (i.e., lower viscosity and higher thermal conductivity) for the temperature range from 300-350 K. As a result, the working fluids selected for experimentation were water, propylene glycol, ethylene glycol, and a 50% by volume mixture of ethylene glycol and water. Thus, performance analysis of the HEX with multiple working fluids will allow for the hierarchical classification of the working fluids as heat recovery fluids within the WHR apparatus.

Table 3.2: Properties of 50% by volume mixtures of ethylene glycol and propylene glycol with water and associated thermal properties (evaluated at 300 K and 350 K where applicable) [188, 191].

Working Fluid	Evaluated Temperature [K]	Boiling Point [K]	Density [kg/m^3]	Viscosity [$Ns/m^2 \cdot 10^2$]	Specific Heat [kJ/kgK]	Thermal Conductivity [W/mK]	Prandtl Number [-]
50/50 EG & Water	300	380.93	1081.28	0.323	3.273	0.386	27.41
	350	-	1048.80	0.105	3.472	0.410	8.85
50/50 PG & Water	300	378.71	1039.20	0.504	3.558	0.365	49.13
	350	-	1003.84	0.122	3.753	0.399	11.43

3.4 WHR Experiments and Analysis

In the initial rounds of testing, experimental trials using the WHR apparatus (i.e., the standard HEX with no DPF cores installed) were conducted. The first round of testing was completed to verify that the apparatus was still operational after several years out of service. This was done by directly comparing the heat transfer rates, effectiveness, and overall heat transfer coefficients to values obtained by Sprouse [20]. After this initial validation, the objective of the second (primary) round of testing was to directly compare the performance parameters of the apparatus with various working fluids. That is, the heat transfer rates, effectiveness, and overall heat transfer coefficients were directly compared for each of the working fluids to discern which working fluid allowed for the largest heat transfer rate to the working fluid, while also maximizing the HEX parameters. Following this, convective heat transfer parameters in the form of the Nusselt number and convective heat transfer coefficient were calculated and compared for each working fluid. A fluid obtaining higher values indicated improved convection within the HEX over the other fluids, subsequently making it a more attractive working fluid.

In the initial validation test, water was used as a working fluid in order to reproduce previous results, while the second utilized water, propylene glycol, ethylene glycol, and a 50% by volume mixture of ethylene glycol and water. The results of both rounds are presented in this section. In the second round of testing, a lack of agreement in the trends of the heat transfer rates and the HEX parameters (i.e., the effectiveness and overall heat transfer coefficient), a convective heat transfer analysis was conducted to provide additional values to compare the working fluids (i.e., the convection heat transfer coefficient and the Nusselt number). Therefore, the methodology for the convective heat transfer analysis and the subsequent results are also presented, to allow for the sought conclusions to be drawn from their comparative parameters. Finally, the results of both the experiments and convective analysis provide the backdrop for a complete discussion of the performance of the working fluids, allowing for their subsequent ranking and heat transfer fluids within the HEX.

3.4.1 Experimental Results

Table 3.3 presents the experimental results of the two trials completed in the initial round of testing, the objective of which was to directly compare these results to previous results using the heat transfer rates, effectiveness, and overall heat transfer coefficient. The first trial experienced an exhaust temperature difference of 53.22 K, a working fluid temperature difference of 9.97 K, and a rate of heat transfer loss (Q_{loss}, defined as the difference between Q_{ex} and Q_{wf}), of 10.22 W. For the second trial, these values were 52.50 K, 8.60 K, and 52.98 W, respectively. Between the two trials, the largest discrepancy was in Q_{loss}, correlating to differences in the working fluid heat transfer rates and related temperature changes, as the exhaust heat transfer rates were similar.

Although the working fluid temperature difference of the second trial was only 1.37 K less than the first, this translated into a decrease in enthalpy change of 5.78 kJ/kgK. This, when multiplied by the working fluid mass flow rate, explains the 47.36 W difference in the working fluid heat transfer; thus, indicating the sensitivity of the apparatus to temperature differences. Furthermore, since the water entering the system was generally the ambient temperature of the test cell, as the engine runs for a longer period the ambient temperature in the test cell may also increase slightly; hence, growing the temperature of the working fluid as well.

Table 3.3: Experimental results from initial WHR testing with water as the working fluid and associated errors.

Fluid	$\dot{m}_{ex}$ [g/s]	$\dot{m}_{wf}$ [g/s]	$T_{ex,in}$ [K]	$T_{ex,out}$ [K]	$T_{wf,in}$ [K]	$T_{wf,out}$ [K]	Q_{ex} [W]	Q_{wf} [W]	Q_{loss} [W]	ε [-]	U [W/m^{2}K]
Water	6.47 ± 0.33	8.20 ± 0.05	369.34 ± 0.60	316.12 ± 0.07	294.35 ± 0.15	304.32 ± 0.04	352.40 ± 18.02	342.18 ± 5.83	10.22 ± 18.94	0.689 ± 0.037	52.30 ± 1.15
Water	6.47 ± 0.33	8.20 ± 0.05	368.46 ± 0.11	315.96 ± 0.18	297.69 ± 0.09	306.29 ± 0.04	347.80 ± 17.78	294.82 ± 3.82	52.98 ± 18.19	0.629 ± 0.033	50.15 ± 0.84

Particularly, the effectiveness and the overall heat transfer coefficients presented in Table 3.3 are the minimum values, calculated for both trials via the working fluid heat transfer rate. Here, standard deviations for the appropriate averaged values are also provided. For the measured values, this is a standard population deviation across the trials combined with the associated instrument accuracy. While for the calculated values the error is determined using the sequential perturbation technique, which estimates the propagating errors for a calculated value by determining and then combining the influence that the error of each measured parameter has on the calculated value [192]. This same methodology is applied for all subsequent standard deviations presented. Regarding the resulting errors, it is apparent for the first trial that the

deviation in Q_{loss} is larger than the value itself, indicating that this specific trial is questionable, but is included for transparency.

Then, the results were compared with the efforts of Sprouse [20] to address the experiment's goal. The results presented in Table 3.4 are the experimental results using the same device, engine, and experimental techniques, but conducted by Sprouse several years prior [20]. In Table 3.4, averaged mass flow rates and temperatures are presented, as well as the calculated heat transfer rates, effectiveness, and overall heat transfer coefficients, to allow for direct comparison to the results in Table 3.3.

Table 3.4: Experimental results from Sprouse using the WHR apparatus [20].

Working Fluid	$\dot{m}_{ex}$ [g/s]	$\dot{m}_{wf}$ [g/s]	$T_{ex,in}$ [K]	$T_{ex,out}$ [K]	$T_{wf,in}$ [K]	$T_{wf,out}$ [K]	Q_{ex} [W]	Q_{wf} [W]	Q_{loss} [W]	ε [-]	U [W/m^{2}K]
Water	6.413	5.667	375.57	320.58	296.36	309.83	361.34	318.98	42.36	0.623	48.63
Water	6.360	4.833	376.91	321.92	297.19	312.63	358.45	312.02	46.43	0.610	49.73

The current results yielded averaged heat transfer rates of the exhaust and working fluid of 350.10 ± 12.66 W and 318.50 ± 3.48 W, respectively, values for which Sprouse obtained averages of 359.90 ± 1.45 W and 315.50 ± 3.48 W, respectively, resulting in percent differences of 2.76% for the exhaust heat transfer rate and 0.95% for the working fluid heat transfer rate. Additionally, Sprouse had an average heat transfer rate loss between the working fluid and exhaust (Q_{loss}) of 44.39 ± 2.04 W and an average overall heat transfer coefficient of 49.17 ± 0.56 W/m^{2}K, as compared to 31.60 ± 13.13 W and 51.22 ± 0.71 W/m^{2}K for the current results, respectively, yielding a 33.66% difference in the average Q_{loss} but only a 4.08% difference in the

average U. The large difference in the heat transfer loss rate may be due to reinsulating the HEX since Sprouse's testing.

Furthermore, the average effectiveness achieved in this research was 0.659, while the average effectiveness for Sprouse was 0.617, a 6.58% difference, strongly influenced by the difference in working fluid mass flow rates. These variances can be attributed to the indicated dissimilarities in operating conditions (i.e., working fluid mass flow rates, exhaust temperatures, reinsulating the apparatus) and normal working deviations; thus, these similarities validate the current performance of the WHR apparatus against its past performance, achieving the objective of the initial round of testing.

The goal of the second round of experimental testing was to compare the performance of the different working fluids in the WHR apparatus. Of note, water was run before and after the alternate working fluids in order to serve as a control. Table 3.5 presents the experimental results from all trials completed. As in the previous experimental trials, the minimum HEX effectiveness and the overall heat transfer coefficient were calculated for each trial with error values provided. It should be noted that for all but two trials, the minimum effectiveness was that associated with the working fluid heat transfer, as discussed. However, for Trial 2.7 and Trial 2.13, the minimum effectiveness was for the exhaust heat transfer. Furthermore, for Trial 2.13, the calculated heat transfer to the working fluid exceeds that lost by the exhaust, disrupting the energy balance for the HEX; while the deviation on the heat transfer rate loss for Trial 2.14 is nearly zero, also discrediting the energy balance. Thus, these data sets were removed from further consideration, but included in this table for lucidity. Although the deviation on Q_{loss} for

Trial 2.1 is close to the size of the value, making it questionable, it is included in subsequent analysis.

Table 3.5: Experimental results from WHR testing with various working fluid and associated errors. Note: Trials 2.13 and 2.14 were removed from further consideration, as discussed.

Trial	Working Fluid	$\dot{m}_{ex}$ [g/s]	$\dot{m}_{wf}$ [g/s]	$T_{ex,in}$ [K]	$T_{ex,out}$ [K]	$T_{wf,in}$ [K]	$T_{wf,out}$ [K]	Q_{ex} [W]	Q_{wf} [W]	Q_{loss} [W]	ε [-]	U [W/m^{2}K]
2.1	Water	6.50 ± 0.31	8.23 ± 0.05	369.36 ± 0.23	315.61 ± 0.02	290.82 ± 0.04	300.51 ± 0.24	357.24 ± 17.04	333.97 ± 8.73	23.27 ± 19.15	0.639 ± 0.035	45.32 ± 1.45
2.2	Water	6.47 ± 0.31	8.20 ± 0.05	370.27 ± 0.20	315.63 ± 0.03	290.87 ± 0.05	299.63 ± 0.23	362.02 ± 17.02	300.84 ± 8.14	61.18 ± 18.86	0.572 ± 0.031	39.69 ± 1.27
2.3	Water	6.46 ± 0.31	8.20 ± 0.05	371.03 ± 0.22	315.76 ± 0.06	291.12 ± 0.05	299.78 ± 0.25	365.05 ± 17.37	297.15 ± 8.97	67.90 ± 19.55	0.563 ± 0.032	39.06 ± 1.40
2.4	EG	6.44 ± 0.31	8.80 ± 0.05	370.14 ± 0.70	318.70 ± 0.42	295.51 ± 0.03	309.19 ± 0.27	338.99 ± 17.15	248.43 ± 5.15	90.56 ± 17.90	0.593 ± 0.032	48.21 ± 1.64
2.5	EG	6.44 ± 0.31	8.80 ± 0.05	372.17 ± 0.29	319.87 ± 0.21	295.66 ± 0.05	309.93 ± 0.14	344.42 ± 16.50	259.53 ± 3.06	84.89 ± 16.79	0.605 ± 0.030	48.80 ± 0.86
2.6	EG	6.43 ± 0.31	8.83 ± 0.05	372.84 ± 0.11	320.48 ± 0.12	295.96 ± 0.10	310.36 ± 0.08	344.41 ± 16.46	263.01 ± 2.74	81.40 ± 16.69	0.611 ± 0.30	49.02 ± 0.61
2.7	50/50 (EG/H_2O)	6.45 ± 0.31	8.57 ± 0.05	368.82 ± 1.03	320.40 ± 0.69	301.79 ± 0.02	313.56 ± 0.52	319.61 ± 17.35	257.46 ± 11.60	62.15 ± 20.87	0.722 ± 0.056	65.88 ± 5.13
2.8	50/50 (EG/H_2O)	6.43 ± 0.30	8.53 ± 0.05	371.87 ± 0.49	322.19 ± 0.26	301.68 ± 0.03	311.69 ± 0.27	326.96 ± 15.49	217.96 ± 6.17	109.00 ± 16.68	0.610 ± 0.033	46.82 ± 1.80
2.9	50/50 (EG/H_2O)	6.42 ± 0.31	8.43 ± 0.05	373.12 ± 0.16	322.82 ± 0.07	301.54 ± 0.02	310.98 ± 0.15	330.31 ± 15.83	202.93 ± 3.37	127.38 ± 16.18	0.558 ± 0.028	41.26 ± 0.87
2.10	PG	6.42 ± 0.30	7.83 ± 0.05	370.87 ± 0.88	321.74 ± 0.69	296.51 ± 0.02	311.31 ± 0.29	322.92 ± 16.76	195.73 ± 4.08	127.19 ± 17.28	0.604 ± 0.032	47.41 ± 1.83

2.11	PG	6.41 ± 0.29	7.83 ± 0.05	373.28 ± 0.42	323.69 ± 0.33	296.59 ± 0.04	312.23 ± 0.19	325.65 ± 15.21	207.00 ± 2.82	118.66 ± 15.47	0.621 ± 0.030	47.58 ± 1.03
2.12	PG	6.41 ± 0.29	7.83 ± 0.05	374.65 ± 0.25	324.68 ± 0.19	296.77 ± 0.06	312.83 ± 0.13	327.95 ± 15.24	212.58 ± 2.28	115.37 ± 15.41	0.628 ± 0.030	47.82 ± 0.71
2.13	Water	6.41 ± 0.29	8.03 ± 0.05	374.41 ± 0.30	320.40 ± 0.16	290.90 ± 0.02	302.34 ± 0.31	354.47 ± 16.30	384.43 ± 10.66	-29.96 ± 19.48	0.647 ± 0.046	46.97 ± 1.61
2.14	Water	6.41 ± 0.29	8.00 ± 0.05	375.40 ± 0.23	319.88 ± 0.07	290.92 ± 0.02	301.78 ± 0.31	364.30 ± 16.65	363.74 ± 10.47	0.56 ± 19.67	0.656 ± 0.035	44.08 ± 1.55
2.15	Water	6.40 ± 0.30	8.00 ± 0.05	375.84 ± 0.06	318.63 ± 0.06	291.08 ± 0.05	301.02 ± 0.32	368.18 ± 17.03	332.92 ± 11.14	35.26 ± 20.35	0.599 ± 0.034	39.84 ± 1.59

Comprehensive average results for each working fluid are presented in Table 3.6 to provide general trends for each working fluid, along with their specific heat and thermal conductivity (at 300 K) for reference. Markedly, the averages for water now include the two trials from the first round of testing, while excluding the trials previously removed. The working fluid with the highest effectiveness is 50/50 EG/water followed by PG, with values of 0.630 and 0.618, respectively. Furthermore, 50/50 EG/water followed by ethylene glycol exhibited the highest average overall heat transfer coefficients of 51.32 W/m^2K and 48.68 W/m^2K, correspondingly. Water consistently exhibited the highest heat transfer rates for the working fluid and exhaust, resulting in the lowest losses of 41.80 W, while 50/50 EG/water and propylene glycol displayed the highest rate of heat transfer losses of 99.51 W and 120.41 W, respectively.

Table 3.6: Averaged experimental results of the first two rounds of experiments for each working fluid, associated errors, and associated parameters (300 K).

Working Fluid	$\hat{Q}_{ex}$ [W]	$\hat{Q}_{wf}$ [W]	$\hat{Q}_{diff}$ [W]	$\hat{\varepsilon}$ [-]	$\hat{U}$ [W/m^{2}K]	Specific Heat [kJ/kgK]	Thermal Conductivity [W/mK]
50/50 EG/Water	325.63 ± 9.38	226.12 ± 4.52	99.51 ± 10.41	**0.630 ± 0.035**	**51.32 ± 1.84**	3.273	0.386
EG	342.61 ± 9.65	256.99 ± 2.20	85.62 ± 9.89	0.603 ± 0.018	48.68 ± 0.65	2.415	0.259
PG	325.51 ± 9.10	205.10 ± 1.82	120.41 ± 9.28	0.618 ± 0.018	47.60 ± 0.74	2.513	0.203
Water	**358.78 ± 8.22**	**316.98 ± 3.23**	**41.80 ± 8.94**	0.615 ± 0.013	44.39 ± 0.52	**4.180**	**0.610**

Based strictly on the experimental results, several general comparisons can be made. Notably, the 50/50 EG/water presents the highest values of the HEX parameters (i.e., overall heat transfer coefficient, effectiveness), at the expense of lower heat transfer rates. Water obtains greater experimental parameters in the form of the largest heat transfer rate magnitudes for the exhaust and working fluid, while minimizing the loss rate. Furthermore, the averages for the water consist of additional trials, lending more weight to their validity, as opposed to the others with only three trials. Thus, 50/50 and water present promising results over propylene glycol and ethylene glycol based on HEX and experimental parameters, respectively. However, without one working fluid providing both larger heat transfer rates and higher HEX parameters, an additional metric is needed to be able to further compare their performance. As such, convective heat transfer parameters for the various fluids and the exhaust will be compared, to provide further comparative criteria to the working fluids' performance.

3.4.2 Heat Transfer Analysis

To provide another tier of comparative parameters for the working fluids within the HEX, an analysis of the heat transfer occurring within the device, exhaust, and working fluids was conducted. With conduction within the device easy to define (i.e., steady-state conditions, known material thermal conductivity and geometry), the focus was placed on the convection occurring within the various fluid streams, with emphasis on the working fluids to compare their efficacy as heat transfer fluids in providing improve convection over the other working fluid options. Thus, the Nusselt number and the convection heat transfer coefficient were the targeted convection parameters.

The initial methodology adopted to evaluate the convection within the HEX was through the utilization of the thermal resistance network. Conceptually, the thermal resistance network links the convection occurring in the exhaust to that occurring in the working fluid via conduction through the tubes of the HEX. Each of these heat transfer modes are then described as resistances and connected in a network according to the heat transfer pathways available. Within the resistances used to describe the convection in the working fluid and exhaust lies the convective heat transfer coefficients desired to compare specifically working fluid performance. Moreover, the convective heat transfer coefficient can be used to calculate the Nusselt number (Nu) and vice versa, as seen in Eq. (3.14) in which h is the convection heat transfer coefficient, L_c is the characteristic length, and k is the thermal conductivity, in this case of the fluid, ultimately providing the ratio of convection to conduction in a fluid [29].

$$Nu = \frac{hL_c}{k} \tag{3.14}$$

The convection coefficient depends greatly on flow conditions, surface geometry, and other thermodynamic properties. For common geometries, correlations for the Nusselt number, and subsequently the heat transfer coefficient, are developed generally in the form of Eq. (3.15), where a, b, and d are constants. However, the working fluid flow conditions are unique to the surface geometry of the apparatus, without a known literature correlation. Similarly, an exact correlation is unknown for the exhaust flow conditions, despite its simplicity. Thus, the results of the experiments were used to attempt to generate such correlations via the thermal resistance network, with the objective of utilizing these correlations to then calculate the convection heat transfer coefficient and compare the working fluids' convective performance in the HEX.

$$Nu = a\,\mathrm{Re}^{b}\,\mathrm{Pr}^{d} \tag{3.15}$$

As seen in Figure 3.4a, there are three primary heat transfer pathways within the HEX, which together form the thermal resistance network for the HEX. The first is convection from the exhaust gases to the inner diameter of the tubes (R_1); the second is conduction through the tube wall (R_2); the third is convection from the outer diameter of the tubes to the working fluid (R_3).

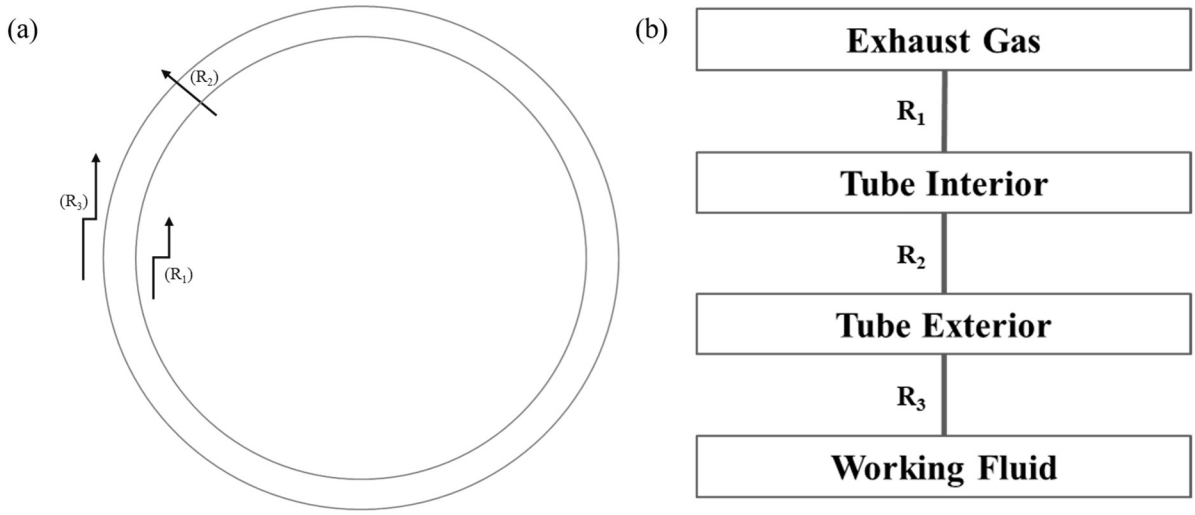

Figure 3.4: (a) Diagram of resistances in HEX tube; (b) Thermal resistance network diagram.

These three resistances can be defined for a radial system as follows:

$$R_1 = \frac{1}{6\left(2\pi r_{inner} L h_{ex}\right)} \tag{3.16}$$

$$R_2 = \frac{\ln\left(\frac{r_{outer}}{r_{inner}}\right)}{6\left(2\pi L k_{tube}\right)} \tag{3.17}$$

$$R_3 = \frac{1}{6\left(2\pi r_{outer} L h_{wf}\right)} \tag{3.18}$$

where r_{outer} and r_{inner} are the outer and inner radii of the tubes, L is the length of the tubes, h_{ex} and h_{wf} are the convection coefficients for the exhaust gas and working fluid, respectively, and k_{tube} is the thermal conductivity of the tubes. The factor of six is the number of tubes in the HEX.

The resistances act in series within the system, as in Figure 3.4b, allowing a total thermal resistance (R_{total}) to be calculated as the sum of the three resistances. From R_{total}, the heat transfer

from the exhaust to the working fluid can be defined using the log mean temperature difference (*LMTD*) calculated as in Eq. (3.11), as [29]:

$$Q = U \cdot A \cdot LMTD = \frac{1}{R_1 + R_2 + R_3} LMTD = \frac{1}{R_{total}} LMTD \tag{3.19}$$

The following assumptions were used in the thermal resistance analysis:

- Steady-state operation of the engine and the HEX.
- Negligible heat loss to the surroundings, kinetic and potential energy changes, radiation effects, and fouling.
- The exhaust gas has the properties of air.
- Properties of the exhaust gas and the working fluid are constant and evaluated at the average of their respective inlet and outlet temperatures.
- Fully developed flow conditions for the exhaust and working fluid.
- The Nusselt numbers of the working fluid and exhaust gas are constant and can be approximated by Eq. (3.15).
- HEX idealized as a concentric tube, parallel flow HEX (i.e., $F = 1$ in the calculation of *LMTD*).

To do this, the total thermal resistance was determined from the calculated *LMTD* and working fluid heat transfer via Eq. (3.19), with h_{ex} in Eq. (3.16) calculated as follows:

$$h_{ex} = \frac{Nu_{ex} k_{ex}}{2r_{inner}} \tag{3.20}$$

In Eqns. (3.16) though (3.18), the geometry parameters were directly measured and the thermal conductivity of the tube was found from literature for stainless steel, a value of 17

W/mK [29]. After calculating R_1 and R_2 from Eqns. (3.16) and (3.17), R_3 was found from R_{total}, and h_{wf} was calculated from Eq. (3.18), as shown below:

$$h_{wf} = \frac{1}{6R_3\left(2\pi r_{outer} L\right)} \tag{3.21}$$

such that the working fluid Nusselt number can be calculated via the following equation:

$$Nu_{wf} = \frac{h_{wf}\left(2r_{outer}\right)}{k_{wf}} \tag{3.22}$$

However, a correlation for Nu_{ex} in Eq. (3.20) is required to obtain h_{wf}. Furthermore, to validate the values of h_{wf} obtained, a relationship in the general form for Nu_{wf} must be generated as a theoretical comparison. As such, prevalent literature relationships for both the exhaust gas and the working fluid Nusselt numbers were researched. These correlations were then used in conjunction with the experimental results to determine Nu_{ex} and Nu_{wf} correlations for the WHR apparatus. The general methodology for developing the Nusselt number correlations is shown in the flowchart in Figure 3.5.

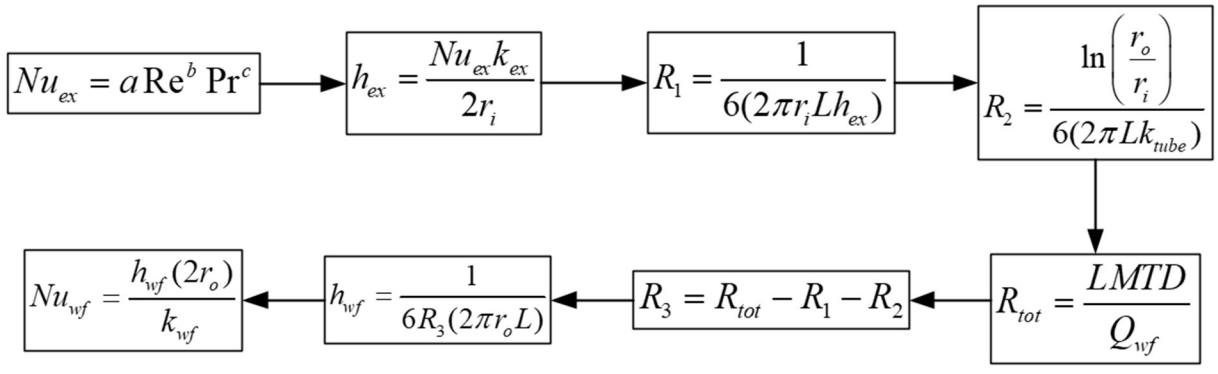

Figure 3.5: Flow chart describing the general methodology for calculating the working fluid Nusselt number.

As seen in Figure 3.5, the process to ultimately calculate the working fluid Nusselt number first begins with the exhaust Nusselt number. Thus, based on the flow conditions of the exhaust (i.e., internal, turbulent flow as determined in Appendix F) literature correlations for flow in similar conditions were found. Note that with the aim of developing a strict correlation for the experimental data, the literature correlations need not strictly apply to the exhaust flow conditions.

Depcik & Assanis presented a comprehensive review of literature correlations for Nu_{ex} and was used as the primary reference for the relationships considered, listed in Table 3.7 [193]. In addition to the equations derived specifically for exhaust gas pipe flow (Nu_{ex}) from Depcik & Assanis, generalizations for fully developed turbulent flow inside circular tubes (Nu_{fd}), as well as simultaneously thermally and hydrodynamically developing flow ($Nu_{th,bl}$), were studied. Moreover, for many ICE applications, the Prandtl number component of the Nusselt number is often ignored since its value is nearly one, as seen in the correlations of Malchow found in [193].

Table 3.7: The exhaust Nusselt correlations considered for internal, turbulent convective flow [193, 194].

Author	Correlation
Colburn	$Nu_{fd} = 0.023\,\mathrm{Re}^{\frac{4}{5}}\,\mathrm{Pr}^{\frac{1}{3}}$
Depcik (exhaust)	$Nu_{ex} = 0.0718\,\mathrm{Re}^{\frac{3}{4}}$
Depcik (universal)	$Nu = 0.07\,\mathrm{Re}^{\frac{3}{4}}$
Dittus-Boelter	$Nu_{fd} = 0.023\,\mathrm{Re}^{\frac{4}{5}}\,\mathrm{Pr}^{0.4}$
Gnielinksi simplification	$Nu_{fd} = 0.016\,\mathrm{Re}^{0.875}\,\mathrm{Pr}^{\frac{1}{3}}$

Gnielinski	$Nu_{fd} = \frac{\frac{f}{8}\mathrm{Re}\,\mathrm{Pr}}{1.07 + 12.7\sqrt{\frac{f}{8}}\left(\mathrm{Pr}^{\frac{2}{3}} - 1\right)}$ where $f = \frac{0.3164}{\mathrm{Re}^{\frac{1}{4}}}$
Kakaç	$Nu_{th,bl} = 0.023\,\mathrm{Re}^{\frac{4}{5}}\,\mathrm{Pr}^{0.4}\left[1 + \left(\frac{2.4254}{\frac{L}{d_i}}\right)^{0.676}\right]$
Malchow	$Nu_{ex} = 0.0483\,\mathrm{Re}^{0.783}$
Sachdev with Meiser & Sorenson	$Nu_{ex} = 0.0774\,\mathrm{Re}^{0.769}$
Shayler	$Nu_{ex} = 0.14\,\mathrm{Re}^{0.68}$

The exhaust gas Nusselt number correlations were then used to calculate the working fluid heat transfer coefficient via the thermal resistance network, the results of which can be seen in Appendix C. From this, the Dittus-Boelter, Colburn, Gnielinski, Gnielinski simplification, Malchow, and Kakaç correlations were not chosen since they yielded principally or completely negative values for the heat transfer coefficients, indicating that the literature correlations were not accurately predicting the exhaust side behavior. Shayler, Depcik (exhaust), and Depcik (universal) attained primarily positive values, but several negative values as well. Thus, only the Sachdev correlation achieved positive values for all working fluids.

To further fit the data, and to achieve a correlation in the form of Eq. (3.15) with customary values of *b* and *c* equal to ¾ and 1/3, respectively, the Sachdev Nusselt number was used to calculate *a* for the exhaust Nusselt number in the following manner [193]:

$$a = \frac{Nu_{Sachdev}}{\mathrm{Re}^{\frac{3}{4}}\,\mathrm{Pr}^{\frac{1}{3}}} = \frac{0.0774\,\mathrm{Re}^{0.769}}{\mathrm{Re}^{\frac{3}{4}}\,\mathrm{Pr}^{\frac{1}{3}}} \tag{3.23}$$

For the experimental results, Eq. (3.23) yielded an average *a* value of 0.102, thus yielding the following initial correlation for Nu_{ex}:

$$Nu_{ex,opt,initial} = 0.102\,\mathrm{Re}_{ex}^{\frac{3}{4}}\,\mathrm{Pr}_{ex}^{\frac{1}{3}} \tag{3.24}$$

In evaluating this correlation, comparisons can be made to the universal correlation developed and verified by Depcik & Assanis [193], in which, the value of the leading coefficient *a* is 0.078, smaller than the value achieved for Eq. (3.24). However, both correlations used the universal values of ¾ and 1/3 for *b* and *d* from Eq. (3.15), respectively. As such, the value for *a* the comes from fitting the model to the experimental data, in keeping with the methodology of Depcik & Assanis.

The next step was the generation of a Nusselt number correlation for the working fluid passing through the shell of the HEX. In corroborating the results of the thermal resistance analysis with the experimental results, an optimization was conducted to fit a Nusselt number correlation in the form of Eq. (3.15) to the values of h_{wf}. As with the exhaust, this process began with identifying various literature correlations for similar, albeit varying, conditions, such as general external flow, flow over staggered tubes, and flow into shell-and-tube HEXs. Thus, twelve related Nusselt number correlations for similar fluid flow were found in the literature and are listed in Table 3.8.

Table 3.8: The correlations considered for the Nusselt number of a working fluid for similar conditions as the HEX [29, 195-202].

Author	Correlation
Zukauskas	$Nu = 0.9\,\mathrm{Re}^{0.4}\,\mathrm{Pr}^{0.36}$
Hausen	$Nu = 0.87572\,\mathrm{Re}^{0.57}\,\mathrm{Pr}^{0.31}$
Short	$Nu = 1.16\,\mathrm{Re}^{0.6}\,\mathrm{Pr}^{\frac{1}{3}}$
Dittus-Boelter	$Nu = 0.023\,\mathrm{Re}^{0.8}\,\mathrm{Pr}^{0.4}$
Kern	$Nu = 0.36\,\mathrm{Re}^{0.55}\,\mathrm{Pr}^{\frac{1}{3}}$
Kays	$Nu = 0.332\,\mathrm{Re}^{0.5}\,\mathrm{Pr}^{\frac{1}{3}}$
Miller	$Nu = 0.032\,\mathrm{Re}^{0.8}\,\mathrm{Pr}^{\frac{1}{3}}$
Weisman	$Nu = 0.00514\,\mathrm{Re}^{0.8}\,\mathrm{Pr}^{\frac{1}{3}}$
Rieger	$Nu = 0.01467\,\mathrm{Re}^{0.86}\,\mathrm{Pr}^{0.4}$
Dingee	$Nu = 0.023\,\mathrm{Re}^{0.8}\,\mathrm{Pr}^{\frac{1}{3}}$
Staggered Tubes	$Nu = a\,\mathrm{Re}^{b}\,\mathrm{Pr}^{0.36}$ where $a = 0.9$; $b = 0.4$ based on the Reynolds number range
Bell-Delaware	$Nu = \frac{c(2r_{outer})\left(\frac{1}{\mathrm{Pr}}\right)^{\frac{2}{3}} J}{k_{wf}}$ where J is the product of correction factors accounting for tube arrangement, recirculation flow, and temperature gradient.

The working fluid optimization (the code and results for which can be found in Appendix D) utilized the various Nusselt number equations, to determine which correlation most strongly correlated to the Nusselt number calculated from the thermal analysis (i.e., h_{wf} calculated from h_{ex} via Nu_{ex}), according to a least-squares difference (LSQ) analysis. The working fluid Nusselt number coefficients (i.e., *a, b*, *c* in Eq. (3.15)) and the leading coefficient for the exhaust Nusselt number in Eq. (3.24) were varied to minimize the LSQ, as seen in the flow chart in Figure 3.6. Notably, for the Bell-Delaware correlation, 53 constants affecting the calculation of *J* were optimized instead of *a*, *b*, and *c*.

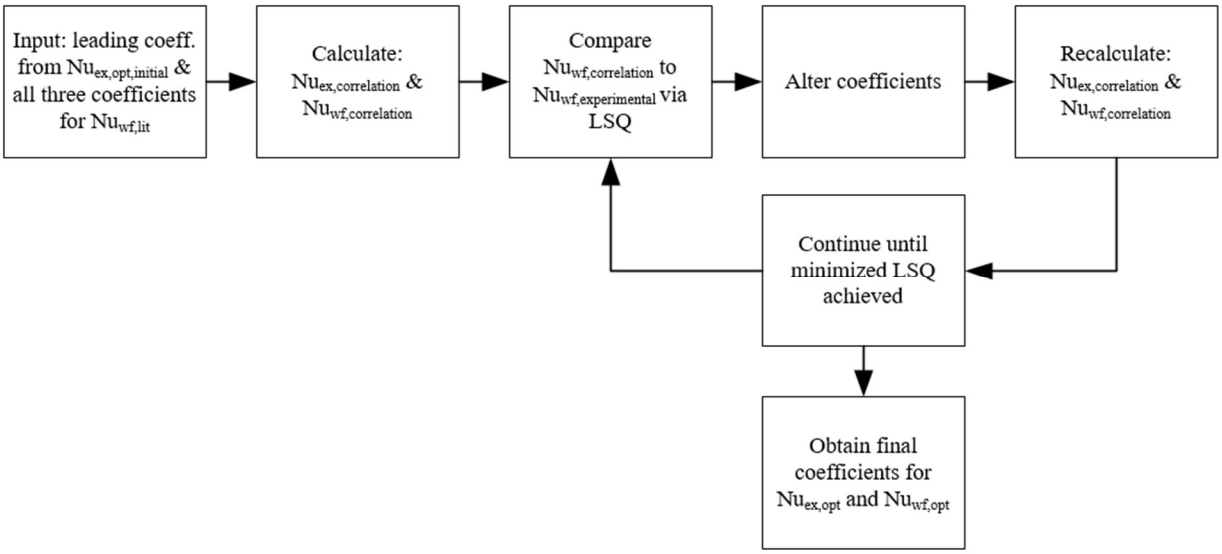

Figure 3.6: Flow chart describing the process to optimize the exhaust and working fluid Nusselt number coefficients.

Of the potential working fluid correlations, Short and Kern were the correlations with the lowest LSQ values of 0.6271 and 0.6273, respectively. However, the leading coefficients for the exhaust Nusselt number correlation in Eq. (3.24) were 500.46 for Short and 496.31 for Kern, resulting in Nusselt numbers of 1.992-2.038 x 10^5 and corresponding convective heat transfer coefficients between 3.133-3.151 x 10^5 W/m^{2}K. Expected values of the convective heat transfer coefficient for gases in forced convection reside in the range of 25-250 W/m^{2}K, a range that the calculated values are exceeding by more than three orders of magnitude [29]. As such, the optimizations were deemed inappropriate.

Thus, the temperature data were further assessed as a means to locate disparities in the thermal resistance analysis causing the failure of the attempted optimizations. From this, it was apparent that the assumption of perfect insulation for parts of the HEX was incorrect, seen in the difference between exhaust inlet and outlet surface temperatures (from the Type K thermocouples) and stream temperatures, labelled in Figure 3.7. As seen in Table 3.9, for the

exhaust inlet, the surface temperature of the inlet reducer (T_{S1}) was on average 11.17 ± 1.67 K lower than $T_{ex,in}$, indicative of heat loss through the inlet piping to the reducer. For the outlet, T_{S4}, the surface temperature of the outlet reducer, was on average 2.29 ± 1.02 K higher than $T_{ex,out}$, indicative of a smaller, but similar, loss as the exhaust gas passed from the outlet reducer to the tubing. However, aside from several exceptions towards the end of the trials, the average surface temperature of the shell (i.e., the average of T_{S2} & T_{S3} or $\hat{T}_{S,shell}$), was generally equal to that of the average working fluid temperature ($\hat{T}_{wf}$), such that the assumption of negligible shell side ambient losses holds. In the cases where the average surface temperature was larger than the ambient test cell temperature, it is likely that heat transfer losses were occurring. However, to find the correlation coefficients *a*, *b*, and *d*, these losses were not considered.

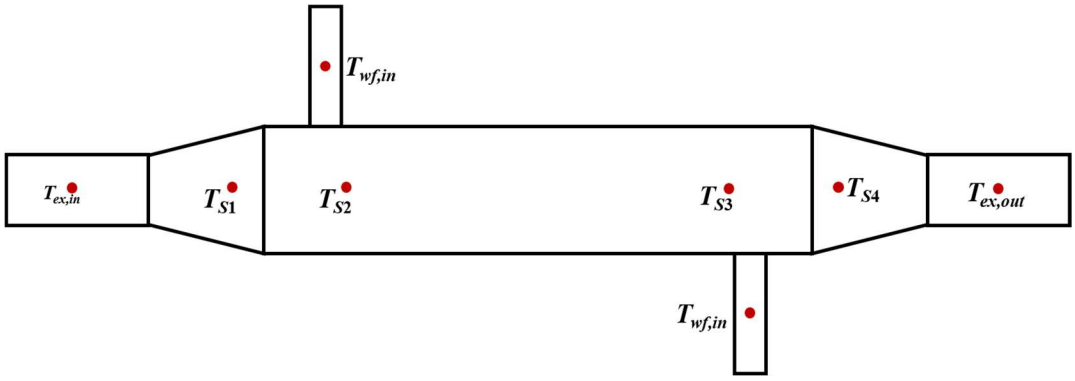

Figure 3.7: Locations of thermocouples on the HEX.

Table 3.9: Exhaust, working fluid, surface, and ambient temperatures for all WHR apparatus experimental trials.

Trial	Working Fluid	$T_{ex,in}$ [K]	T_{S1} [K]	$T_{ex,out}$ [K]	T_{S4} [K]	$T_{wf,in}$ [K]	$T_{wf,out}$ [K]	$\hat{T}_{S,shell}$ [K]	T_{amb} [K]
1.1	Water	369.34	357.58	316.12	318.22	294.35	304.32	299.64	300.14
1.2	Water	368.46	355.65	315.96	318.37	297.69	306.29	302.23	300.05
2.1	Water	369.36	357.03	315.61	316.64	290.82	300.51	296.73	301.38
2.2	Water	370.27	357.98	315.63	316.42	290.87	299.63	296.04	301.53
2.3	Water	371.03	358.62	315.76	316.48	291.12	299.78	296.13	301.68
2.4	EG	370.14	358.34	318.70	320.91	295.51	309.19	301.03	302.10
2.5	EG	372.17	361.18	319.87	322.39	295.66	309.93	301.46	302.19
2.6	EG	372.84	362.32	320.48	323.12	295.96	310.36	301.83	302.27
2.7	50/50	368.82	357.46	320.40	323.61	301.79	313.56	313.34	302.27
2.8	50/50	371.87	357.46	322.19	323.61	301.68	311.69	314.89	302.34
2.9	50/50	373.12	364.06	322.82	326.19	301.54	310.98	315.28	302.40
2.10	PG	370.87	360.52	321.74	324.99	296.51	311.31	315.17	302.34
2.11	PG	373.28	364.71	323.69	327.31	296.59	312.23	316.89	302.34
2.12	PG	374.65	366.85	324.68	328.50	296.77	312.83	317.29	302.34
2.15	Water	375.84	364.79	319.63	320.83	291.08	301.02	304.26	302.57

Employing the difference between exhaust and working fluid heat transfer values as an initial value of Q_{loss}, h_{loss} for the exhaust tubing can be approximated via Eq. (3.25), where A_{S1} and A_{S4} are the surface areas corresponding to the inlet and outlet reducers and tubing.

$$h_{loss} = \frac{Q_{loss}}{A_{S1} + A_{S4}} \tag{3.25}$$

Then, the surface temperatures at the exhaust's inlet and outlet reducers were used to estimate an actual value of Q_{loss} via h_{loss}, from which one can calculate the exhaust temperature inside the reducers with the ambient losses considered, T_{α} and T_{β}, for the inlet and outlet, respectively. Notably, it was assumed that only half of the calculated lost heat transfer truly escaped. Without this assumption, the exhaust heat transfer values were below that of the working fluid, which, as discussed before, cannot occur (i.e., heat transfer occurs from high to low temperature regions). Upon calculation of these temperatures, new values for the exhaust heat transfer were calculated via the alpha and beta temperatures. The new Q_{ex} was anticipated to provide a more appropriate metric of the exhaust heat transfer rate while also considering losses within the shell of the HEX, but neglecting further ambient losses. A full schematic of this process can be seen in Figure 3.8.

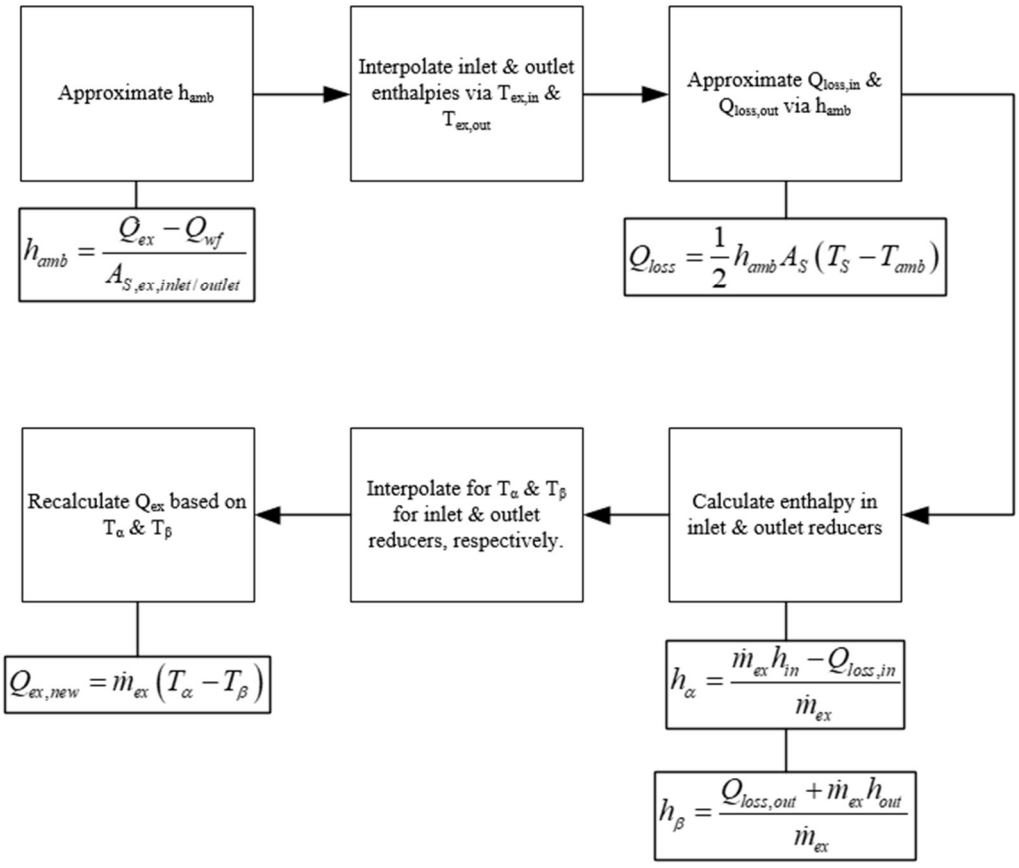

Figure 3.8: Flow chart of the methodology for calculating the exhaust temperature in the HEX reducers.

With the new data computed, the same methodology for calculating h_{wf} and the subsequent optimization of the coefficients was carried out once more as in Figure 3.6. However, the resulting h_{ex} and Nu_{ex} values were still orders of magnitude larger the typical values, even with precautions taken to limit the coefficient in the Nu_{ex} expression (results are located in Appendix E). Thus, despite the precautions taken to account for many of the losses, the use of the thermal resistance network still did not yield suitable results.

Therefore, without knowing the surface temperatures of the tubes, there was no other methodology to directly calculate the heat transfer coefficients without unsubstantiated assumptions to concretely define losses. Furthermore, the repeated attempts to use the resistance

network did not produce any useful results. Although the analysis carried out was informative for the researcher and identified several areas of improvement in the experimental apparatus for future iterations, it did not yield workable correlations for the Nusselt numbers of the exhaust or working fluid.

However, in order to compare the convective behavior of the working fluids, the exhaust and the working fluid conditions were examined once again to assign the most appropriate literature correlations. Primarily, the fluid flows were exactly defined through their Reynolds' numbers. This, in addition to calculations for thermal and hydrodynamic boundary layers for the exhaust (Appendix F), allowed for the exclusion of several literature correlations previously considered.

For example, the working fluid is in laminar flow, excluding the following for turbulent or fully developed flow: Short, Dittus-Boelter, Miller, Weisman, Rieger, and Dingee. Due to the complicated nature of its calculation, the Bell-Delaware correlation was also excluded. Subsequently, the Zukauskas, Hausen, Kern, Kays, and Staggered Tubes correlations were used to calculate the Nusselt number and heat transfer coefficient for the working fluid. In order to remain conservative, the correlation providing the minimum values was selected as the estimate of the working fluid heat transfer: the Kays correlation.

A similar approach was taken in determining the most applicable literature correlation for the exhaust heat transfer in turbulent, fully developed flow. As such, the unsuitable Colburn and Dittus-Boelter correlations were removed. Instead of utilizing the most conservative correlation, the Depcik (universal) correlation was chosen. Not only did this correlation provide heat transfer

coefficient values within the expected range for gases in forced convection, but also it is a widely utilized correlation for exhaust flow, cited over 75 times in Google Scholar [203].

Thus, the average heat transfer coefficient and Nusselt number based on the assigned correlations, in addition to the Reynolds and Prandtl numbers, are presented in Table 3.10, with the associated standard deviations. In calculating the exhaust Reynolds number, the inner diameter of a single tube was used as the characteristic length; in calculating the working fluid Reynolds number, the characteristic length used is the hydraulic diameter of the shell. Water had the highest average heat transfer coefficient and Nusselt number, followed by the 50/50 mixture of EG and water. Although the exhaust Nusselt number and heat transfer coefficient should be the same across working fluids, and are in fact all similar, separate average values and standard deviations are presented in Table 3.10, yielding an overall average Nusselt number of 31.73 ± 0.02 and an average heat transfer coefficient of 49.41 ± 3.88 W/m^{2}K.

Table 3.10: Average heat transfer coefficients and Nusselt numbers for each working fluid and the exhaust, calculated using the Kays (working fluid) and Depcik universal (exhaust) correlations, and associated errors.

Working Fluid	$\hat{\mathrm{Re}}_{ex}$ [-]	$\hat{\mathrm{Pr}}_{ex}$ [-]	$\hat{Nu}_{ex}$ [-]	$\hat{h}_{ex}$ [W/m^{2}K]	$\hat{\mathrm{Re}}_{wf}$ [-]	$\hat{\mathrm{Pr}}_{wf}$ [-]	$\hat{Nu}_{wf}$ [-]	$\hat{h}_{wf}$ [W/m^{2}K]
50/50	3468.89 ± 95.49	0.701 ± 0.000	31.64 ± 0.65	49.40 ± 1.02	18.87 ± 0.08	22.38 ± 0.05	4.06 ± 0.01	71.34 ± 0.12
EG	3476.57 ± 95.63	0.701 ± 0.000	31.69 ± 0.66	49.38 ± 1.03	3.69 ± 0.01	131.97 ± 0.27	3.25 ± 0.01	37.80 ± 0.06
PG	3446.75 ± 92.48	0.700 ± 0.000	31.49 ± 0.63	49.36 ± 0.99	1.66 ± 0.01	352.48 ± 1.19	3.02 ± 0.01	27.42 ± 0.05
Water	3508.90 ± 69.61	0.701 ± 0.000	31.91 ± 0.47	49.46 ± 0.74	52.96 ± 0.14	6.27 ± 0.01	**4.45 ± 0.01**	**121.94 ± 0.15**

In response to the difficulties encountered in determining correlations for the Nusselt numbers, additional consideration was given to the assumption of a correction factor equal to one in the *LMTD* calculation. Specifically, the calculations were repeated using a calculated correction factor for a shell-and-tube HEX with a single shell and a multiple of two tube passes, incorporating more realistic flow complexities within the HEX [29]. Additionally, for this computational methodology, the HEX was assumed to be under counterflow conditions, changing the temperature differences used to calculate *LMTD* to:

$$\Delta T_1 = T_{ex,in} - T_{wf,out} \tag{3.26}$$

$$\Delta T_2 = T_{ex,out} - T_{wf,in} \tag{3.27}$$

The average correction factor determined for the HEX experimental trials was 0.94, thus affecting the calculation of the overall heat transfer coefficient and any calculations involving R_{total} from the thermal resistance network. Table 3.11 displays the averaged overall heat transfer coefficients for each working fluid for the idealized case where F is one, and for for the case where F was considered, via calculation and interpolation of the equations and chart in Figure 3.9, respectively, with MATLAB. Table 3.1 also includes a worst scenario case where F is 0.75, to quantify the effect inclusion of the correction factor can have on the analysis. As expected, the inclusion of the correction factor deceased the overall heat transfer coefficient. However, slight variations in the experimental temperatures for the various working fluids resulted in varying correction factors, altering the trends seen (i.e., PG had a larger correction factor, leading to a corrected U larger than that of EG, despite being smaller than EG when uncorrected). Since the worst-case correction factor is equal across the board, the same trends are seen as in the

uncorrected *U*. Nevertheless, the impact of the correction factor becomes apparent in the alterations it makes to the rank of the working fluids according to the magnitude of the achieved overall heat transfer coefficient.

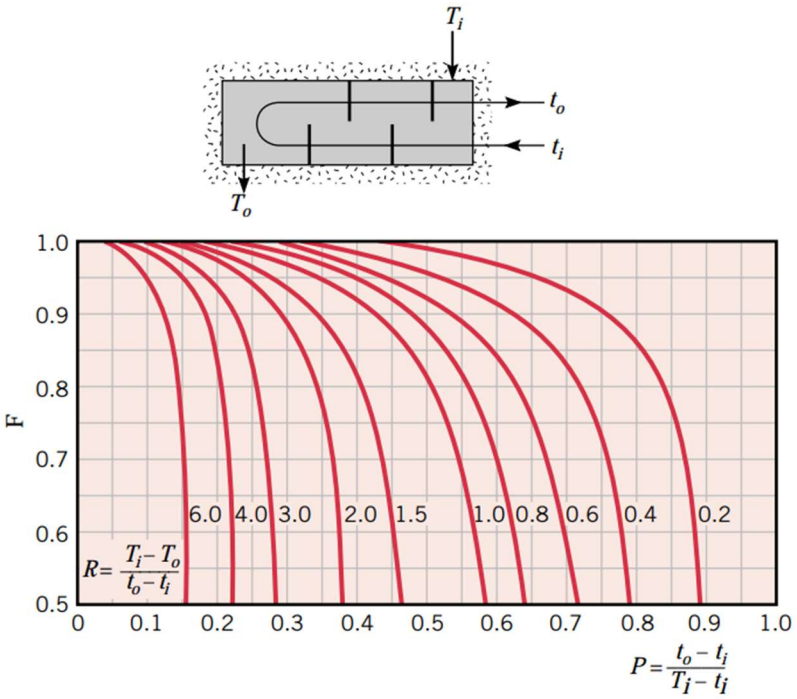

Figure 3.9: Chart to calculate the HEX correction factor for a shell-and-tube HEX with a single shell and a multiple of two shell passes, along with the associated temperatures *T* (shell-side) and *t* (tube-side) [29].

Table 3.11: Average correction factors and associated average overall heat transfer coefficients for the WHR experiments.

Working Fluid	$\hat{F}_{ideal}$ [-]	$\hat{U}_{ideal}$ [W/m²K]	$\hat{F}_{calculated}$ [-]	$\hat{U}_{calculated}$ [W/m²K]	$\hat{F}_{worst}$ [-]	$\hat{U}_{worst}$ [W/m²K]
50/50	1	51.32	0.93	39.48	0.75	31.86
EG	1	48.68	0.94	37.15	0.75	29.57
PG	1	47.60	0.96	37.27	0.75	29.25
Water	1	44.39	0.94	36.79	0.75	29.50

Further, the methodology using the thermal resistance network was repeated with the inclusion of the correction factor when calculating the total thermal resistance, to determine if Nusselt number correlations could be developed that would yield more realistic results (i.e., convection heat transfer coefficients within the expected ranges for forced convection). Similar to the calculation of the overall heat transfer coefficient, this was done for both the calculated F, as well as the worst-case F, to again assess the implication this correction factor carried. Once again, many of the exhaust correlations evaluated initially provided negative values of the convection heat transfer coefficient of the working fluid, indicating that even with the correction factor, flow conditions were not being accurately approximated via these correlations. However, as before the Sachdev correlation did provide positive values, allowing for the determination of specific Nusselt number correlations via the same methodology explained previously.

Table 3.12 displays the average convection heat transfer coefficients from this analysis, with the average results from the literature correlations previously indicated, as well as the average results for each working fluid for the best correlations obtained. For the calculated $\hat{F}$, the LSQ value on the obtained correlations was 0.54, while an LSQ of 0.49 was attained for the worst-case correlations.

Table 3.12: Convection heat transfer coefficients for the exhaust and working fluids calculated using various correction factors.

Working Fluid	$\hat{F}_{ideal} = 1$		$\hat{F}_{calculated} = 0.94$		$\hat{F}_{worst} = 0.75$	
	$\hat{h}_{ex}$ [W/m^{2}K]	$\hat{h}_{wf}$ [W/m^{2}K]	$\hat{h}_{ex}$ [W/m^{2}K]	$\hat{h}_{wf}$ [W/m^{2}K]	$\hat{h}_{ex}$ [W/m^{2}K]	$\hat{h}_{wf}$ [W/m^{2}K]
50/50	49.40	71.33	450.01	39.79	825.45	48.32
EG	49.38	37.80	449.85	32.16	825.15	40.98
PG	49.38	27.42	449.61	31.55	824.71	39.92
Water	49.46	121.94	450.65	45.63	826.60	56.33

The inclusion of a correction factor, as well as the alteration of the correction factor used, had drastic effects on the resulting convection heat transfer coefficients. First, the exhaust heat transfer coefficients are still over twice the range for gases in forced convection (i.e., greater than two times the range of 25-250 W/m^{2}K [29]), indicating that these correlations are still not appropriate, despite having lower LSQ values than those obtained with a correction factor of unity and despite being more realistically representative of the flow conditions within the HEX. Moreover, the resulting working fluid convection coefficients are dramatically different for water and the 50/50 mixture across the range of *F* values, yet more similar for EG and PG. Although the trends across the working fluids are the same for each of the correction factors, the fact that such varying results are obtained from this methodology through the alteration of a single factor makes it extremely difficult to identify a single solution that is more accurate than the others without the use of an additional, external methodology, such as 3-D heat transfer modeling, with which to corroborate the results. As such, the inclusion of the correction factor, while shedding light on the effects from including complex flow conditions, did not yield a more concrete

examination or description of the convection heat transfer coefficients and associated Nusselt number correlations.

Thus, without a concrete way to validate the correct methodology, the literature correlations used for the correction factor of unity were the convective parameters ultimately utilized to compare working fluid performance, allowing for general trends of the working fluids' behaviors to be observed. Based on these convective parameters alone, the most promising working fluids were water and 50/50, since they have the largest heat transfer coefficients and Nusselt numbers. However, strictly categorizing the working fluids on the literature thermal analysis excludes considerations of the experimental performance.

3.4.3 Discussion

The trends of the heat transfer analysis can be combined with the experimental results to provide a general basis for comparing the working fluids. Based on the experimental results alone (i.e., the working fluids' average effectiveness, overall heat transfer coefficient, and general heat transfer results); water and the 50/50 mixture were the best performing working fluids. Similarly, based on the results of the heat transfer analysis (i.e., working fluid Nusselt number and convective heat transfer coefficient), water and 50/50 performed superiorly. Thus, propylene glycol and ethylene glycol were excluded from further consideration.

Water produced higher heat transfer rates than the other working fluids, indicating larger quantities of heat transfer for a given time. However, the overall heat transfer coefficient and the HEX effectiveness allow for comparison of performance despite experimental variations and can be combined with the thermal properties (see Table 3.6). The effectiveness and overall heat

transfer coefficient are proportional to the working fluid specific heat, for which water followed by 50/50 have the largest values. Furthermore, water and 50/50 possesses the highest thermal conductivity over the other working fluids. Thus, the superior performance of 50/50 and water over the other working fluids, seen in the effectiveness and overall heat transfer coefficient, is likely due to their combinations of specific heats and thermal conductivities.

Additionally, the convective heat transfer coefficients and Nusselt numbers can be used to indicate the magnitude of the convective heat transfer occurring in each working fluid. In the case of both h_{wf} and Nu_{wf}, water had larger values. For the convective heat transfer coefficient, this indicates that, for the same change in temperature from tubes to the fluid with surface area held constant, the water will produce greater heat transfer rates than the 50/50 (an increase of 46.56 W/m^{2}K from 50/50 to water, resulting in a 65.26% growth in the heat transfer rate). For the Nusselt number, this means more effective convection is occurring, dominating over conduction within the flow. However, it must be reiterated that the correlations were not specifically developed for this HEX; nonetheless, they provided general trends from which these conclusions were drawn.

Ultimately, water and 50/50 both present themselves as attractive working fluids for use in the current apparatus, and as such, were selected for the DPFHX experiments. Based on the results of the WHR experiments, water presents itself overall as a working fluid that will produce greater rates of heat transfer within the system, while minimizing losses, in conjunction with more effective convection within the working fluid itself. However, 50/50 appears more effective in the apparatus based strictly on its HEX parameters. Once more, the continued use of water

will allow for tracking the apparatus' performance with and without the DPF cores, while also allowing for its comparison to the 50/50 mixture. Moreover, the hope is that the DPFHX experimental results will provide an additional criterion with which to compare the performance of the two working fluids.

3.5 DPFHX Experiments and Analysis

The final experimental effort involved testing the apparatus with DPF cores installed to compare the performance of the combined DPFHX to that of the WHR apparatus via the experimental, HEX, and convective parameters. The aim was to ascertain if the DPFHX had higher values than the WHR device, indicating improved performance. Furthermore, the two working fluids achieving the highest operational parameters in the WHR apparatus (i.e., water and 50/50 water/EG) were tested within the DPFHX device to further compare their performance to each other, in an effort to determine a singular working fluid that functions optimally in the HEX with or without DPF cores installed.

It is important to address that the DPF cores obtained by Sprouse [20] were not adequately sized for the HEX and required adjustments. Specifically, instead of being 0.4572 m in length (i.e., tubes' lengths in the HEX) the cores came in 0.3048 m lengths. Moreover, instead of being just under 22.23 mm in diameter (i.e., the tubes' diameters), the cores were near 25.4 mm in diameter. To resolve the length issue, the cores were cut with a wet tile saw and taped together using Nashua 322 multi-purpose foil thermal tape, as shown in Figure 3.10. In order to resolve the diameter sizing issue, the outer diameter was sanded down until the cores would fit within the inner diameter of the tubes. When taping the cores together, great care was taken to properly

align the DPF channels such that every-other channel was blocked (a characteristic of DPFs). Furthermore, after sanding the outer radius initially, the cores had to be further sanded to allow the cores to fit within the tubes after the application of the thermal tape.

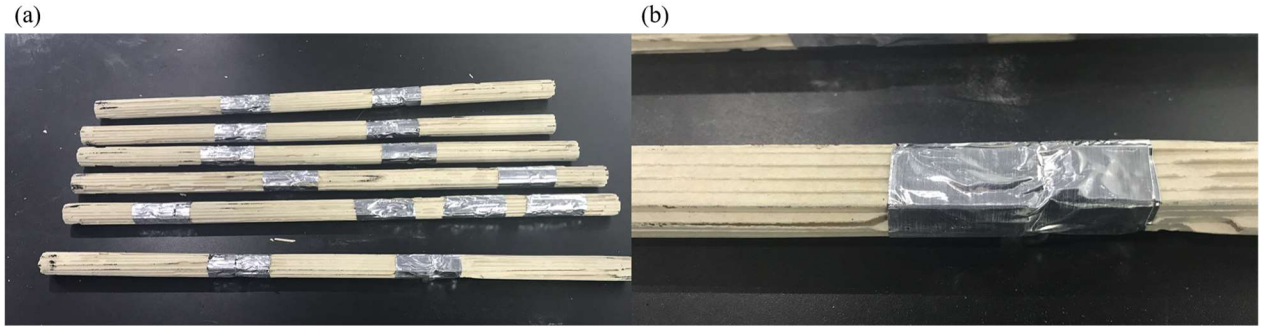

Figure 3.10: (a) The six DPF cores with the applied thermal tape; (b) A close up of the thermal tape used to join the cores together.

Although the mere presence of the cores alters heat transfer and convection within the HEX, these modifications cause the potential for deterioration of the heat transfer rates within the HEX, presenting themselves as additional thermal resistances to be overcome. One such resistance may be due to the bands of thermal tape preventing conduction to the inner radius of the tubes, as it may act as an insulator to the length of core it is covering. An additional resistance may be due to the presence of the thermal tape around the outer radius of the cores blocking exhaust gases and impeding flow in the outer channels of the cores. Furthermore, the under sizing of the cores, seen in Figure 3.11, could have created a gap for the exhaust gases to pass along the outer radius of the core without entering the channels. Thus, these changes have the potential to vary the heat transfer pathways in the DPFHX apparatus.

Figure 3.11: DPF cores installed in the six tubes of the HEX.

The final step in modifying the apparatus was to reinsulate the HEX and reconstruct the apparatus, including thermocouples and pressure transducers. All instrumentation was checked after being reassembled in order to ensure that it was operating correctly. However, in reattaching the Type K thermocouples, one of the thermocouples was damaged; thus, only three Type K thermocouples were present during the DPFHX experimental testing. While two of the thermocouples were placed on the exterior of the shell of the HEX, providing important monitoring temperatures (i.e., maintaining the working fluid below its boiling point), the other two were placed on the inlet and outlet reducers of the exhaust gas, very near to the location of the thermocouples measuring the exhaust stream temperature. Thus, with similar measurements being taken there, the loss of one thermocouple was deemed inconsequential, provided two thermocouples were still placed on the shell exterior.

The details of such modifications are presented to provide the context for the subsequent results and will be further addressed in the discussion of the DPFHX thermal resistance network. Moreover, it must be indicated that due to laboratory constraints and the direction of future work, it was not endeavored to rebuild the device in avoidance of the alterations. Regardless, the performance of the two working fluids in the DPFHX were compared to each other and ultimately compared to the results of the water and 50/50 in the WHR device. Then, the combined results of the experiments provided conclusions and recommendations for moving forward with the DPFHX.

3.5.1 Experimental Results

The goal of these experiments was to evaluate the concept of the DPFHX by assessing whether the presence of the DPF cores improves or degrades the various performance parameters (i.e., heat transfer rates, effectiveness, etc.) occurring within the apparatus. Based on the work of Sprouse, an increase in the overall heat transfer coefficient of the HEX specifically is expected with the cores inserted, as indicated by the results of a simulation of the DPFHX and WHR devices [20, 184]. A secondary goal was to compare the performance of two different working fluids, as selected from the WHR experiments (i.e., water and 50/50 EG/water) according to the same comparison criteria. The experimental results of the DPFHX tests are presented in Table 3.13 for three trials each of water and the 50/50 mixture.

Table 3.13: Experimental results from DPFHX testing with various working fluids and associated errors.

Working Fluid	$\dot{m}_{ex}$ [g/s]	$\dot{m}_{wf}$ [g/s]	$T_{ex,in}$ [K]	$T_{ex,out}$ [K]	$T_{wf,in}$ [K]	$T_{wf,out}$ [K]	Q_{ex} [W]	Q_{wf} [W]	Q_{loss} [W]	ε [-]	U [W/m^{2}K]
Water	6.67 ± 0.35	8.33 ± 0.05	372.04 ± 0.14	338.02 ± 0.04	290.44 ± 0.03	295.65 ± 0.05	232.36 ± 12.02	181.62 ± 2.32	50.74 ± 12.02	0.326 ± 0.017	15.84 ± 0.21
Water	6.66 ± 0.35	8.33 ± 0.05	372.04 ± 0.15	338.19 ± 0.05	290.50 ± 0.02	295.67 ± 0.04	231.00 ± 11.91	180.54 ± 1.95	50.46 ± 11.93	0.324 ± 0.017	15.73 ± 0.17
Water	6.66 ± 0.33	8.27 ± 0.05	372.72 ± 0.07	338.65 ± 0.09	290.67 ± 0.05	295.84 ± 0.05	232.43 ± 11.47	178.92 ± 2.62	53.51 ± 11.56	0.320 ± 0.016	15.48 ± 0.23
50/50	6.62 ± 0.32	8.80 ± 0.05	371.64 ± 0.16	341.11 ± 0.17	295.15 ± 0.04	299.32 ± 0.06	207.26 ± 10.17	93.02 ± 1.67	114.24 ± 10.15	0.231 ± 0.012	10.90 ± 0.20
50/50	6.62 ± 0.33	8.77 ± 0.05	371.91 ± 0.07	340.75 ± 0.12	295.21 ± 0.04	299.53 ± 0.05	211.25 ± 10.63	95.76 ± 1.45	115.48 ± 10.63	0.237 ± 0.012	11.28 ± 0.17
50/50	6.60 ± 0.34	8.73 ± 0.05	371.83 ± 0.11	340.75 ± 0.08	295.31 ± 0.03	299.60 ± 0.08	212.33 ± 10.75	95.04 ± 1.91	117.29 ± 10.71	0.237 ± 0.013	11.25 ± 0.23

The average results and associated thermal properties are presented in Table 3.14. Water exhibited the highest effectiveness and overall heat transfer coefficients of 0.323 and 15.68, respectively. Furthermore, water had average higher values of heat transfer rates from the exhaust and to the working fluid, while also achieving the lowest rate of loss between the two. However, when compared to the average results of water and 50/50 from the WHR experiments in Table 3.6, both working fluids performed significantly worse. For water, the effectiveness and overall heat transfer coefficient decreased by 0.298 (-47.99%) and 28.67 W/m^{2}K (-64.64%),

respectively. For 50/50, these values declined by 0.395 (-62.70%) and 40.18 W/m^{2}K (-78.29%), respectively.

Table 3.14: Average experimental results for the DPFHX experiments with associated errors and associated properties (300K).

Working Fluid	$\hat{Q}_{ex}$ [W]	$\hat{Q}_{wf}$ [W]	$\hat{Q}_{loss}$ [W]	$\hat{\varepsilon}$ [-]	$\hat{U}$ [W/m^{2}K]	Specific Heat [kJ/kgK]	Thermal Conductivity [W/mK]
Water	231.93 ± 6.81	180.36 ± 1.34	51.57 ± 6.84	**0.323 ± 0.010**	**15.68 ± 0.12**	**4.180**	**0.610**
50/50	210.28 ± 6.07	94.61 ± 0.87	115.67 ± 6.06	0.235 ± 0.007	11.14 ± 0.12	3.273	0.386

Both fluids experienced larger losses between the exhaust and the working fluid heat transfer rates, increasing from the WHR experiment by 15.66 W (+43.61%) and 16.16 W (+16.16%) for the water and 50/50, respectively. This outcome likely stems from the process of reinsulating the HEX after installing the DPF cores, indicating that better methodology is prudent for future iterations. Additionally, they exhibited lower heat transfer rates; for water, the heat transfer rate from the exhaust decreased by 127.64 W (-35.50%) and for the working fluid by 143.30 W (-44.27%) values of 115.35 W (-35.42%) and 131.51 W (-58.16%), respectively, for the 50/50. These differences in heat transfer rate are directly related to the following reductions in temperature changes for the exhaust and the working fluid: 20.30 K (-37.41%) and 4.76 K (-47.89%) for the water and 18.43 K (-37.26%) and 6.15 K (-59.08%) for the 50/50. Overall, with similar temperatures, these losses indicate worsening heat transfer rates occurring within the DPFHX compared to the WHR apparatus.

Based on the experimental results, water outperformed the 50/50 mixture with improved heat transfer rates and HEX parameters. Despite this, they both performed quantitatively worse than in the WHR apparatus. However, these results will be considered alongside the thermal analysis to allow for additional discussion

3.5.2 Heat Transfer Analysis

A heat transfer analysis of the DPFHX was completed following the procedure in the WHR analysis. Although water was clearly the optimal working fluid within the DPFHX from the experimental results, the determination of the convection parameters allowed for comparison of the performance of the DPFHX to the WHR device through the convective heat transfer coefficients and the Nusselt numbers of the exhaust and the working fluid. Ideally the same methodology would have been utilized to develop convection parameters (i.e., the thermal resistance network), but due to the errors encountered previously, literature correlations ultimately provided the convective heat transfer coefficients and Nusselt numbers. However, for thoroughness, the thermal resistance network of the DPFHX is examined subsequently. While the presence of the cores alone changed the thermal pathways, the adjustments to the DPF cores introduced additional thermal resistances with implications on heat transfer within the DPFHX apparatus. Thus, the thermal resistance network expanded.

In addition to the assumptions of the WHR thermal resistance network, the DPF cores are assumed fresh, with no soot loading. Moreover, for exhaust gases flowing through the core walls, the temperature of the wall is assumed to instantaneously become the temperature of the gas during porous wall convection [204]. Furthermore, conduction through the DPF core is assumed

to begin in one central empty channel and propagate outwards. Finally, contact resistances involved were assumed approximately that of similar materials or interfaces.

Examining the heat transfer pathways of the DPFHX apparatus, there are nine different thermal resistances that can be identified in Figure 3.12, six more than the WHR apparatus. The general thermal resistances for convection and conduction in radial systems are as follows, similar to Eqs. (3.16) and (3.17):

$$R_{conv} = \frac{1}{2\pi r_{outer} L h} \tag{3.28}$$

$$R_{cond} = \frac{\ln\left(\frac{r_{outer}}{r_{inner}}\right)}{2\pi L k} \tag{3.29}$$

where r_{outer} and r_{inner} are the outer and inner radii [m], L is the applied length [m], h is the convection coefficient [W/m^{2}K], and k is the thermal conductivity [W/mK].

The first four resistances are standard for DPF cores; starting at the center of the DPF core, the first thermal resistance encountered is for convection in the channels of the DPF cores (R_1). This resistance is a result of the forced convection from the gas to the DPF channel walls acting upon the entire length across the radius of the cores.

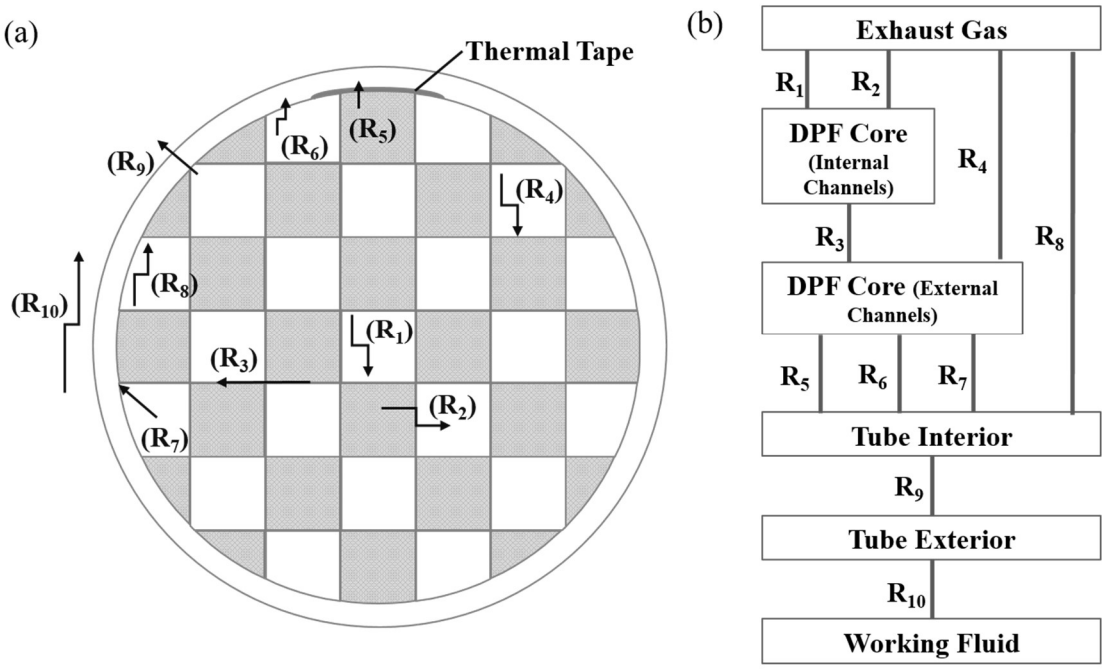

Figure 3.12: (a) Diagram of the thermal resistances presence in the tubes of the HEX with the DPF cores installed; (b) Thermal resistance network of the HEX with the DPF cores.

The second thermal resistance is convection in the porous walls of the DPF cores (R_2) acting in parallel to R_1, occurring via forced convection as the blocked DPF channels force the exhaust gas through the DPF walls. Moreover, R_2 also acts along the entire length of the DPF cores and across the entire radius. However, the convection coefficient appearing in the thermal resistance network is that of exhaust gas flowing through the wall, different from R_1. Additionally, the temperature of the exhaust gases changes radially within the core, altering this resistance as the gas moves outward. However, in most DPF analysis, the cores are assumed to be the temperature of the exhaust gas passing through them, making this resistance negligible, but is included here for completeness [204]. Acting in series with R_1 and R_2 is R_3, conduction from the interior cells to the perimeter cells of the DPF core, occurring from a central empty channel outward to the outer radius along the entire lengths of the cores. Finally, there is also R_4, which similarly to R_1 is convection in the DPF channels; however, with the radial temperature

change of the exhaust gas, this convection resistance varies greatly from the inner DPF channels to the outer channels.

Following the four DPF core induced resistances, there exist three thermal resistances acting together in parallel due to the modifications made to the cores. The first of these is R_5, conduction through the thermal tape applied to the DPF cores, applied over the approximate length of the tape on each core. The presence of the thermal tape on the cores also created R_6, convection through the gaps between the DPF core and the tube wall interior. The thermal tape essentially created a resistance fit for the cores within the tubes, meaning that the portions without the thermal tape experienced a gap between the edge of the core and the tube wall. This gap could create a convection heat transfer pathway with the convection coefficient of the exhaust gas in the channel acting along the length of the DPF core without thermal tape. The final thermal resistance due to the modifications is the contact resistance between the DPF cores, the thermal tape, and the tube wall interior (R_7), applied along the length of the tape on the cores.

The remaining three resistances (i.e., R_8, R_9, and R_{10}) are the fundamental thermal resistances in the apparatus. Specifically, R_8 is the thermal resistance for the convection from the exhaust gases to the tube wall interior in the outer channels of the DPF core that open to the tube wall, R_9 is conduction through the tube wall, and R_{10} is convection from the tube wall exterior to the working fluid in the HEX shell. Hence, R_8 acts in parallel with the DPF resistances, which then act in series with R_9 and R_{10}.

As before, all geometry-related parameters were measured directly from the apparatus, and the working fluid and exhaust properties were calculated based on an average temperature. The

values for the thermal conductivities (i.e., for the tube wall, the thermal tape, and the cores) and contact resistances (i.e., between the core to the tube wall via the thermal tape) were obtained from literature. Thus, the remaining parameters were the convection coefficients of the working fluid in the tube, the exhaust gas in the channel, and the exhaust gas in the core wall.

Traditionally, the procedure would then follow analogously to that outlined in the WHR thermal resistance network, with the *LMTD* and all known resistances now used to calculate R_9 related to the working fluid convection from the tubes' exterior. However, due to the previous struggles encountered with the simpler network of the WHR apparatus and *F*, literature correlations were again adopted to estimate the heat transfer parameters during DPFHX operation.

To account for the presence of the cores and the alterations they create for the exhaust flow, a constant Nusselt number of 2.71 for exhaust flow in DPF cores with square channels was adopted [204]. Traditionally, the correlation chosen also involves the Peclet number; however, Depcik & Assanis showed that 2.71 was an appropriate average value [204]. For the working fluid, the Kays correlation was again used to calculate the convective heat transfer coefficient and Nusselt number, for simplicity and for direct comparison between the experiments. Thus, the average results are presented in Table 3.15. In calculation of the Reynolds numbers, the same characteristic lengths are used for the exhaust tube and the working fluid, but for the exhaust channel, the height of a single DPF channel was used as the characteristic length.

Table 3.15: Average heat transfer coefficients and Nusselt numbers for each working fluid and the exhaust, calculated using the Kays correlation (working fluid) and DPF cores with square channels (exhaust), and associated errors.

Working Fluid	$\hat{\mathrm{Re}}_{ex,tube}$ [-]	$\hat{\mathrm{Re}}_{ex,channel}$ [-]	$\hat{\mathrm{Pr}}_{ex}$ [-]	$\hat{\mathrm{Nu}}_{ex}$ [-]	$\hat{h}_{ex}$ [W/m^{2}K]	$\hat{\mathrm{Re}}_{wf}$ [-]	$\hat{\mathrm{Pr}}_{wf}$ [-]	$\hat{\mathrm{Nu}}_{wf}$ [-]	$\hat{h}_{wf}$ [W/m^{2}K]
50/50	3492.89 ± 101.06	1524.06 ± 44.10	0.699 ± 0.000	2.71	36.13 ± 0.00	14.82 ± 0.05	29.68 ± 0.02	3.96 ± 0.01	68.28 ± 0.11
Water	3525.67 ± 104.14	1538.36 ± 45.44	0.699 ± 0.000	2.71	36.04 ± 0.00	48.78 ± 0.16	6.97 ± 0.00	**4.43 ± 0.01**	**120.19 ± 0.20**

Water achieved a higher average Nusselt number and average convective heat transfer coefficient than the 50/50 mixture. Specifically, the average Nusselt number of water was 0.47 larger (an 11.21% difference) and the average convective heat transfer coefficient of water was 51.91 W/m^{2}K greater (a 55.09% difference). The higher Reynolds number of the water, based on density and viscosity, outweighed the larger Prandtl number of 50/50, subsequently yielding more favorable heat transfer parameters.

Accordingly, the averaged exhaust results were similar in both cases. Notably, the Reynolds number for flow in the DPF channels was smaller than the Reynolds number through the tubes. Although the exhaust flow was turbulent prior to the insertion of the cores, the flow becomes laminar through the DPF channels. This becomes increasingly important when comparing the WHR and DPFHX experiments.

Based on the theoretical heat transfer results, water displays larger promise as a working fluid within a DPFHX, due to its improved convective heat transfer coefficient and Nusselt number. However, as with the WHR experiments, the heat transfer analysis results will be used

in accordance with the experimental results. Furthermore, the DPFHX results will be compared with the WHR outcomes to examine the working fluid trends along with the influence of the DPF cores within the HEX tubes.

3.5.3 Discussion

Selected results from the WHR and DPFHX experiments are collated in Table 3.16. For both working fluids, the effectiveness and overall heat transfer coefficient decreased by over half from the WHR to DPFHX experiments, opposite of the trend expected based on the efforts of Sprouse who achieved higher overall heat transfer coefficients in a simulation of this DPFHX than the WHR apparatus [20]. Furthermore, the average Reynolds number, Nusselt number, and convective heat transfer coefficients all decreased. For the exhaust, the Reynolds number decreased due to laminar flow, as mentioned; thus, the Nusselt number and exhaust heat transfer coefficient fell correspondingly.

Table 3.16: Averaged HEX and heat transfer parameters for water and 50/50 EG/water from the WHR and DPFHX experiments and associated errors.

Experiment	Working Fluid	$\hat{\varepsilon}$ [-]	$\hat{U}$ [W/m^{2}K]	$\hat{\mathrm{Re}}_{ex}$ [-]	$\hat{Nu}_{ex}$ [-]	$\hat{h}_{ex}$ [W/m^{2}K]	$\hat{\mathrm{Re}}_{wf}$ [-]	$\hat{Nu}_{wf}$ [-]	$\hat{h}_{wf}$ [W/m^{2}K]
WHR	50/50	0.630 ± 0.035	51.32 ± 1.84	3468.89 ± 95.50	31.64 ± 0.65	49.40 ± 1.02	18.87 ± 0.08	4.06 ± 0.01	71.34 ± 0.12
DPFHX	50/50	0.235 ± 0.007	11.14 ± 0.12	1524.06 ± 44.10	2.71	36.13 ± 0.00	14.82 ± 0.05	3.96 ± 0.01	68.28 ± 0.11
WHR	Water	0.615 ± 0.013	44.35 ± 0.52	3508.90 ± 69.61	31.91 ± 0.48	49.46 ± 0.74	52.96 ± 0.14	4.45 ± 0.01	121.94 ± 0.15
DPFHX	Water	0.323 ± 0.010	15.68 ± 0.12	1538.36 ± 45.44	2.71	36.04 ± 0.00	48.78 ± 0.16	4.43 ± 0.01	120.19 ± 0.20

The expected outcome of the DPF core installation was to improve the overall heat transfer coefficient; thus, enhancing the quality and quantity of heat transfer occurring from the exhaust to the working fluid. In the heat transfer parameters, this is most directly seen in the reduced Reynolds number. Specifically, the presence of the cores slows down the exhaust flow, providing an increased residence time of the exhaust gas, allowing for more time for heat transfer to occur. However, the limited number of core channels present only cut the Reynolds number in half. Therefore, the reduction in heat transfer transitioning from turbulent to laminar flow was not overcome sufficiently by increasing the time for heat transfer or the additional heat transfer pathways provided by the cores. A simple estimate indicates that the residence time should be further increased by (~49.46/36.13) another 1.5-2× to make up for the loss in turbulence.

Another significant detriment to the heat transfer is likely a result of the modifications required for core installation. Specifically, although the cores are meant to promote enhanced heat transfer, the gaps on the outside of the cores, as well as the added resistances from the thermal tape and the potential for channels to be misaligned, all impede heat transfer from actually occurring. Thus, a decrease in Nu_{ex} and h_{ex} was not completely unexpected. To reiterate this thought, the HEX was dismantled after conducting the experiments with Figure 3.13 displaying the condition of the cores. As can be seen, four of the six cores remained in their initial, installed location and show a darker color associated with soot loading. However, two of the cores were forced down the length of the tube. This movement suggests that the cores were blocking a good portion of the flow, likely due to the misalignment of channels. Therefore, the cores are not able to operate in their designated function (i.e., filtering PM out of the exhaust by passing through the core walls) and they are preventing the anticipated heat transfer

improvements. Although blocked channels present the opportunity for increasing the residence time of the exhaust gas in the tubes, as it becomes stuck in the multiple blocked channels, it would also then increase the flow rate through other non-blocked portions of the cores. This would consequently increase the Reynolds number in the remaining clear core channels and further reduce the residence time of the exhaust gas, contrary to the initial expectation for the cores.

Figure 3.13: DPF cores installed in the HEX after DPFHX testing, showing the slippage of the blocked cores.

It was previously noted that the cores had to be undersized in order for the thermal tape connecting sections to fit within the tubes, which is most appropriately seen the top left and bottom left cores in Figure 3.13. Such gaps present the potential for the exhaust gas to pass along the outside of the cores, without flowing through the porous material at all. This outside passage

could increase the speed of the exhaust gas as it passes along the length of the cores without thermal tape, again reducing the exhaust gas' residence time, while removing the additional pathways, and presenting another source for the depressed heat transfer results.

Overall, the effects of these heat transfer impediments are seen in the degradation of the effectiveness and overall heat transfer coefficients for both working fluids between the WHR and DPFHX experiments. However, water appears to be a better medium for heat transfer, including a slightly higher coefficient for the DPFHX experiments over the WHR tests. This indicates that even with a lower effectiveness and smaller overall heat transfer rates, improved convective heat transfer is still occurring in the water over the 50/50 mixture.

3.6 Influence of WHR and DPFHX Devices on Engine Performance

Aside from the performance of the WHR and DPFHX equipment, another important parameter is their effect on engine performance. To this end, the in-cylinder pressure traces present a relatively simple way of examining the influence of their installation. Figure 3.14 presents four in-cylinder pressure traces from the engine: motoring (i.e., not injecting fuel), standard injection with the muffler installed (i.e., normal firing operation), standard injection with the WHR apparatus included (i.e., normal WHR apparatus operation), and standard injection with the DPFHX apparatus connected (i.e., normal DPFHX operation). These data for the WHR and DPFHX pressure traces represent a single trial from their respective experiments with water as a working fluid. Specifically, the WHR data are from Trial 2.15 at 0.2 N·m and the DPFHX data are from Trial 3.3 at 0.6 N·m, while the engine firing data and motoring trace are from a comparable engine loading point (i.e., 0.5 N·m).

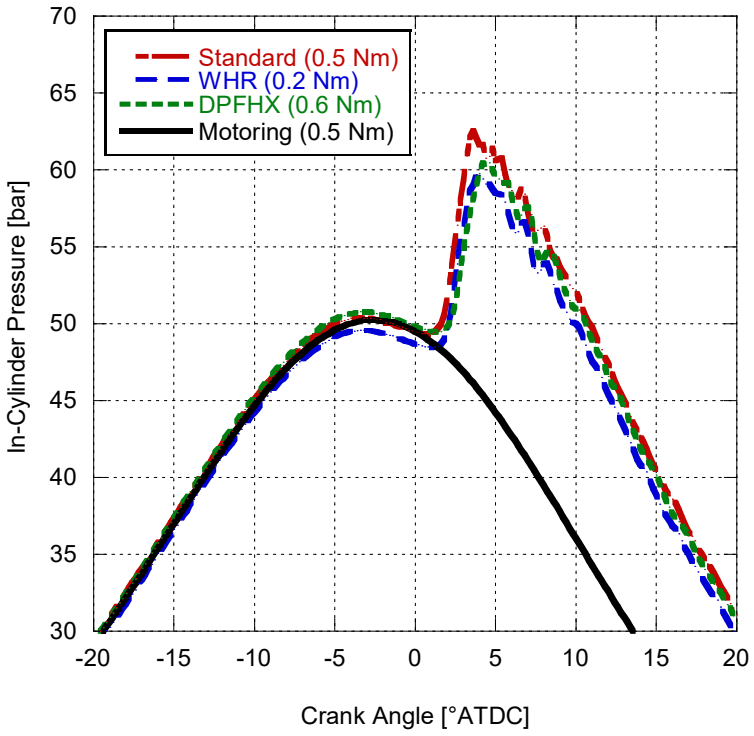

Figure 3.14: In-cylinder pressure traces for the single-cylinder test engine when motoring, when firing in standard operating conditions and with the WHR and DPFHX apparatuses installed graphed against crank angle in degrees after top-dead center [ATDC].

Based on the general pressure trends displayed in Figure 3.14, it can be concluded that both the WHR and DPFHX devices affect the performance of the single-cylinder test engine. Both induce a lower in-cylinder pressure, which would result in increased fuel consumption of the engine to meet the same operating points. Although the DPFHX reaches a higher peak pressure than the WHR (60.45 bar versus 59.66 bar, respectively), the differences in engine loading points must be noted. Since the DPFHX trial was at a higher loading point that the standard trace, it can be concluded that at 0.5 N·m, the DPFHX would reach a slightly lower peak pressure, despite the backpressure it induces. Conversely, the WHR trial is at a lower loading point than the standard trace, indicating that at 0.5 N·m it would reach a slightly higher peak pressure. However, the traces shown in Figure 3.14 display generally that both the WHR and DPFHX apparatuses negatively affect engine performance.

The pressure traces hint at the added complexity of including a WHR or a DPFHX device in the exhaust stream. As such, precautions must be taken to minimize their potential impact on engine performance. Moreover, the true influence of the DPF cores on the in-cylinder pressure, whether it is the standard added backpressure from the cores or an exaggerated backpressure due to blocked channels, cannot be discerned without further experimentation. For reference, the pressure drop in the exhaust across the HEX for the experimental trials was 0.004 psi (0.0003 bar) for the WHR trial and 0.158 psi (0.0109 bar) for the DPFHX trial.

For the single-cylinder engine, it can be concluded that this WHR device with or without DPF cores had a detrimental effect on the performance of the engine at hand. This indicates that a WHR rig needs to be optimized for the engine it is coupled with or it may negatively affect engine performance. By tailoring the WHR apparatus to the engine, the fuel consumption benefits through the eventual installation of an RC system can be further improved. Additional design considerations must also be taken for the combined DPFHX to specifically augment its performance before use within an RC system.

3.7 Experimental and Apparatus Comments for Future Work

As apparent from the analysis presented, there are a number of opportunities for improving the testing apparatus. The rig was designed and built by Sprouse [20], and moving beyond this work, the HEX will no longer be utilized. Instead, the researcher will design and implement a completely new device, designed specifically for the test engine. However, in this endeavor, the issues and subsequent lessons learned from this initial experimental exertion provide numerous

metrics upon which to improve. Moreover, additional work can be done to further clarify the analysis conducted in this effort.

To this end, the author will complete 3-D heat transfer modeling of the WHR and DPFHX devices. Not only will this aid in the investigation of the DPFHX concept, specifically regarding whether the modified cores were the source of the detrimental performance, but the modeling will provide an external assessment of the convective heat transfer of each of the working fluids. The results of such an analysis could then be used as validation against the various methods examined in this chapter for evaluating the convective heat transfer coefficient and the Nusselt number. Through such validation, as well as the modeling itself, the flow conditions within the HEX can be more realistically described. Additionally, upon the successful creation of 3-D heat transfer models according to the experimental state parameters (i.e., temperatures, flow rates, etc.), the model can then be extrapolated to allow for the working fluid to boil within the HEX, ideal for the actual operation of the HEX in an RC system. Then, further comparisons can be drawn regarding the ranking of the working fluids, based on the initial experimental values obtained through the efforts in this work.

Regarding the future HEX design efforts, the sizing of the apparatus and all components can be addressed. Not only will the newly designed HEX be more compact and appropriately sized for the engine, but also the DPF cores need to be suitably sized in diameter and length to prevent installation issues. With a single core being the appropriate length for the HEX's tube, the cores can serve their aftertreatment function, while encouraging augmented heat transfer. Furthermore, smaller, more compact sizing will result in a lower pressure drop across the HEX, with the

potential to mitigate any latent performance degradation, while also allowing for an easier accommodation for steady state conditions (i.e., less thermal mass). In addition, through more appropriate design considerations, the engine can be run at higher loads, providing higher temperatures in the exhaust stream, increasing the potential heat to be recovered. Moreover, compact HEXs allow for larger heat transfer surface areas with smaller overall dimensions, ideal for future installation on-board a vehicle.

Additional precautions can also be taken to ensure that the maximum amount of data is collected. This defect was most apparent during the thermal resistance analysis. Without measuring tube surface temperatures, in addition to the thermocouples being located several inches upstream or downstream of the HEX's inlet and outlet, the conditions of the exhaust and working fluid inside of the shell and the tubes the HEX were not specified. Furthermore, with inadequate insulation and the potential for ambient free convection on the exterior, even the measured temperatures were not guaranteed to provide a comprehensive picture of the physical states and heat transfer occurring within the HEX.

As such, any future apparatus should include comprehensive measurements of the physical states of both the exhaust and working fluid entering, leaving, and within the HEX, through the installation of additional outer surface thermocouples, intermediate thermocouples and pressure transducers midstream, and ideally, surface temperature measurements within the HEX itself. Additionally, since the HEX will be more compact, it will be easier to properly insulate, and the use of an enclosed box surrounding the HEX with ambient temperature and pressure measurements will reduce external free convection and ambient losses. The presence of such

measures should allow for the quantification of losses within the system for more precise representations of the heat transfer mechanisms within the HEX. Moreover, additional trials should be taken across all experiments conducted in order to reduce errors in the data and improve the repeatability of the experiments.

The final component to be included in future work is to introduce the use of additive manufacturing (AM) to create the new HEX. This manufacturing technique will aid in the compact design of the HEX and reduce the weight of the apparatus, aiding in the overall goal of the DPFHX to reduce fuel consumption for CI engines. Furthermore, magnesium and titanium are more common materials for AM, and as such, the thermal properties of the HEX itself may change, including differences induced by the manufacturing technique. The effect of AM is conjecture, as this is the primary subject of the author's PhD research and will be addressed in the future, but remains important to note.

Thus, despite the seemingly negative experimental results obtained, as well as the subsequent struggles encountered in analyzing the heat transfer pathways, the experiments conducted still yielded substantial contributions to the overall work of the author. Furthermore, addressing such struggles and unexpected results at this stage presents the opportunity for improvement in future iterations of the DPFHX concept.

3.8 Conclusions

The purposes of the experiments conducted and described in this chapter were to validate the performance of the WHR apparatus on the single-cylinder test engine, compare the performance

of working fluids in the apparatus, and evaluate the performance of the DPFHX apparatus all done via experimental, HEX, and convection parameters. Ideally, the desired outcome was to validate the DPFHX's improved heat transfer performance over the WHR apparatus. Through the three rounds of experiments conducted, all -of the previous aims have been accomplished.

In the first round of experimental trials, the performance of the WHR apparatus with water was compared to the performance of the same apparatus during the experiments conducted by Sprouse [20]. The general agreement between the two dissimilar tests indicated that the apparatus was still operational after time out of service.

Following the first round of tests, multiple working fluids were used in the WHR apparatus to compare their efficacy as heat recovery fluids. These working fluids were selected after a thorough comparison of working fluid properties. The primary factors influencing the scope of the working fluid review were thermal properties for a working fluid in RC WHR operation (i.e., low specific heat, low viscosity, high thermal conductivity, low specific volume), a wide spread of property values (i.e., the Prandtl number), safety considerations (i.e., safe for use in an open system), and finally practical considerations (i.e., matching pump specifications, commercial availability, low cost). Based on these factors, ethylene glycol and propylene glycol were selected as the two primary working fluid options, in addition to water. Furthermore, the properties of 50/50 mixtures of propylene glycol/water and ethylene glycol/water were considered to provide a mid-range working fluid. A 50/50 ethylene glycol/water mixture had a higher thermal conductivity, lower specific heat, and a lower specific volume than a 50/50 propylene glycol/water mixture; thus, making it a more thermally attractive working fluid option.

Assessing the performance of the four working fluids (i.e., water, EG, PG, 50/50 EG/water) in the WHR apparatus, the primary parameters considered were the heat transfer rates, HEX effectiveness, and the overall heat transfer coefficient, all calculated from experimental data. For these values, water and 50/50 presented the highest values, indicating better efficacy and quantity of heat transfer occurring in the apparatus with these working fluids based on improved HEX parameters and heat transfer rates, respectively.

To provide another metric of the working fluid performance, a thermal resistance analysis was attempted on the WHR apparatus. However, due to a lack of data to quantify losses within the system, the analysis proved unable to generate correlations for the convective heat transfer coefficient and the Nusselt number of the working fluid. The influence of a HEX correction factor to allow for more realistic representation of flow complexities was also considered, subsequently indicating that a separate analysis method would be needed to determine the most accurate description of the convection. Thus, literature correlations applicable to the flow conditions (i.e., Depcik (universal) for the exhaust; Kays for the working fluid) were applied to the flows to provide general evaluations of the convective behavior. As such, the exhaust heat transfer parameters were similar for all of the working fluids, given the equivalent operating conditions used across all trials. However, a wider range of variability was seen in the various working fluid properties.

Consequently, water and 50/50 EG/water once again yielded the highest values, this time for the convective heat transfer coefficient of the working fluid and the working fluid Nusselt number, indicating more effective convective heat transfer occurring. The larger magnitudes of

these values indicate that for the same temperature change of the working fluid across the same surface area, water and 50/50 EG/water will provide more heat transfer than the other working fluids, in conjunction with their superior experimental performance in the apparatus. Thus, moving forward to the DPFHX experiments, water and 50/50 were the primary working fluids used.

In conducting the DPFHX experiments, several modifications were made to the DPF cores before installation since they were not sized for the HEX tubes. As such, the cores were sanded down in diameter and pieced together in length to fit within the tubes of the HEX. These modifications, although done with care, ultimately caused performance degradations in the DPFHX experimental results. Across a wide array of heat transfer and HEX parameters, the DPFHX experiments achieved worse results than the WHR apparatus, although the insertion of the cores should have improved (postulation) the overall heat transfer coefficient of the HEX.

Upon applying literature correlations to describe the flow in the DPFHX apparatus (i.e., Depcik flow in square DPF channels for the exhaust; Kays for the working fluid), the change in the exhaust Nusselt number and decrease in the exhaust convective heat transfer coefficient supported this theory. The exhaust flow had a lower heat transfer coefficient due to laminar flow, but more residence time within the cores to allow heat transfer to occur. However, with additional complications arising from the presence of thermal tape and the misalignment of the cores, the expected outcome was not the same.

Although the results of the DPFHX experiments do not support the anticipated outcome, conceptually, the DPFHX still holds weight. The degraded results do not conclusively specify

that the DPFHX vitiates the heat transfer performance of the apparatus, without more experimental trials and data. Through the failed thermal resistance network and contradictory experimental results, additional lessons and ideas were garnered that can be applied to future work on the concept to improve performance (i.e., more trials, more data collected, better insulation). Furthermore, the general superiority of water and 50/50 EG/water is supported across a range of experimental trials; however, selecting a single ideal working fluid requires additional trials and additional experimental considerations.

A supplementary aspect of the experiments conducted is the conclusion that the installation of both apparatuses in the exhaust stream in this case negatively influences the performance of the engine, confirmed by the in-cylinder pressure traces of the engine for standard operation. This designates that the presence of WHR or DPFHX devices in the exhaust and the subsequent possibility for changes in the engines in-cylinder pressure must be targeted as a design criterion in future experiments. A complete WHR system would still capture and utilize the waste heat of an engine, providing benefits despite the potential for degraded performance. However, optimizing the system so that the in-cylinder pressure is unaffected by either device in the exhaust, yields the potential for further improvements in fuel consumption. Moreover, future iterations which consider such optimizations will be able to run at higher engine loads, further enhancing the fuel efficiency benefits available.

Ultimately, the three primary goals of the experimental efforts conducted were achieved. The performance of the WHR apparatus was confirmed and two working fluids were deemed more appropriate for the application. While the results of the DPFHX experiments were not positive,

they still provide invaluable information for the application of this concept in the future. Thus, important conclusions and data will be used moving forward, with the final goal of (ideally) validating improved DPFHX performance and alternative manufacturing techniques. These experiments serve as preliminary datasets for future work to be conducted, and as such, even the generally considered failure in the operation of the DPFHX provides irreplaceable information and insight.

Chapter 4: Conclusions

4.1 Thesis Conclusions

There were several primary goals driving the research conducted in this thesis; all aiming to evaluate the concept of a combined DPFHX for WHR from CI engine exhaust via an RC. First was the appraisal of literature published on WHR systems, covering RCs themselves, other power cycles in competition with RCs, working fluid and component selection, technologies available for components, and various applications of WHR. Second was the experimental validation of the WHR apparatus on-hand, comparing working fluids within this apparatus, and evaluating the performance of the apparatus as a DPFHX. Thus, these goals have each been addressed in detail in this thesis.

The literature review details the state of the art for WHR as of 2018, through a summary of the historical work done between 1973 and 2011 and a detailed review of the work completed between 2012 and 2018. From this review, several trends are apparent. Most notable is the growth in publications on WHR, increasing dramatically throughout the past few decades, revealing the growing interest and utility of WHR for various applications. Moreover, the literature indicates that even from as far back as 1973, RC is the principal system used in WHR applications. However, in recent years, the use of the RC for WHR has introduced new complexities over the basic RC, including multiple loops, reheating, preheating, and regenerating, as researchers find ways to utilize RC WHR in more effective and efficient manners.

Aside from manipulating the schema of the RC system itself, working fluid, heat source, and component selection are all highly researched subsets of RC WHR. In recent years, R245fa has become a widely used working fluid, with effective thermal performance and environmental safety; however, working fluid mixtures are also prevalent due to their ability to combine the ideal properties of multiple fluids. Regarding heat sources, exhaust gases are the most widespread, but as the systems themselves become more complicated, the combination of multiple heat sources, such as the coolant with the exhaust, display competitive performance and efficiency standards. Furthermore, the importance of expander selection is widely noted throughout the literature; as is the importance of HEX design in fully capturing waste heat with the greatest efficiency.

With CI as the predominant application studied for RC WHR, the implementation of a HEX on the single cylinder test engine described in this research proves to be intrinsically applicable. Additionally, the growing importance of working fluid selection, combined with the necessity of HEX design and tailoring an RC system to its specific application, all demonstrate the relevance of this work via the trends in the literature itself.

Hence, with the contextual background of the literature, the experimental efforts to assess and validate the DPFHX were undertaken. Contrary to most literature comparisons of working fluids, done using simulations and computational methods, various working fluids were experimentally compared in this work, providing concrete comparisons of their performance as opposed to trends obtained from simulations. Moreover, the working fluids evaluated experimentally were selected based on literature indications of properties displaying elevated

performance (i.e., low specific heat, low viscosity, high thermal conductivity, low specific volume), as well as safety and practical considerations. Furthermore, based on the ever-growing pervasiveness of mixtures, a mixed working fluid was tested as well.

Upon successful validation of the WHR apparatus based on its previous performance, four working fluids were tested under steady-state conditions in the HEX using the exhaust of the single-cylinder CI engine as a heat source. Comparing water, EG, PG, and 50/50 EG/water on their effectiveness and overall heat transfer coefficient, water and 50/50 EG/water displayed higher values, and thus superior performance as working fluids, over EG and PG. Further heat transfer analysis was done on the HEX to lend additional criteria (i.e., correlations for the Nusselt number of the exhaust and working fluid flows) for the comparisons.

However, in attempting to derive such metrics, gaps in the instrumentation on the apparatus proved to be a weak point in the experiments, lacking measurements to allow for the concrete description of system and ambient losses. Therefore, literature correlations were instead adopted: the Kays Nusselt number correlation for the working fluid, the Depcik (universal) Nusselt number correlation for the exhaust, and the subsequent heat transfer coefficients calculated from both. Water and 50/50 EG/water both yielded higher values, indicating that they provided more effective convective heat transfer as working fluids. Thus, with better experimental performance and enhanced convective heat transfer, these two working fluids were deemed ideal for the WHR apparatus and subsequently used in the DPFHX experiments.

For the DPFHX experiments, cordierite DPF cores were installed in the tubes of the HEX, hypothesized to enlarge the overall heat transfer coefficient of the HEX, consequently improving

the overall performance of the apparatus. Yet, for both working fluids tested, the DPFHX apparatus achieved lower overall heat transfer coefficients, effectiveness values, and heat transfer rates than the WHR apparatus, indicating inferior performance. Although, when comparing the experimental performance, water outperformed the 50/50 EG/water experimentally with a larger effectiveness and overall heat transfer coefficient. Once again, the working fluids' efficacy was compared using literature correlations: the Kays correlation for the working fluid and a constant Nusselt number for the exhaust flow in DPF cores. Nonetheless, from the Nusselt numbers and corollary heat transfer coefficients, the water indicated improved convective heat transfer over the 50/50 mixture, following the results of the experimental comparison.

It is worth mentioning the difference in the exhaust flow convection due to the presence of the DPF cores. In the WHR apparatus, the exhaust flow was turbulent within the HEX tubes, while the cores slowed down the exhaust flow in the DPFHX producing laminar flow. Although turbulence promotes larger heat transfer coefficients and thus more effective convection, the laminar flow within the cores provides additional residence time of the exhaust gas in the tubes with more heat transfer pathways, which can compensate for the laminar flow and allow for further heat transfer from the exhaust gas to the cores and subsequently to the working fluid. However, issues with the installation of the cores, stemming from the cores being inappropriately sized for the HEX tubes, likely prevented this conjectured outcome from occurring.

Moreover, the influence of both the WHR and DPFHX apparatuses on engine performance was evaluated using the engine in-cylinder pressure traces. Based on this metric, it can be

concluded that both the WHR apparatus and the DPFHX apparatus had a negative effect on engine performance, as the pressure within the cylinder decreased when the apparatuses were installed. Although there were slight differences in the engine loading points of the pressure traces compared, the trends of depressed pressures in the engine remain. Notably, the DPFHX device achieved a higher peak in-cylinder pressure than the WHR device. However, the aforementioned issues with the cores installed potentially grow the pressure drop across the HEX, further altering the engine's in-cylinder pressures; hence, additional experiments must be conducted before the true cause of the differences in performance can be concluded. Nonetheless, the changes in engine pressure indicate that although WHR structures provide benefits in the form of fuel efficiency rises, optimizing the systems to their specific applied heat sources can amplify these enhancements.

Therefore, this thesis fully describes the work done towards the aim of gauging the DPFHX concept. Ultimately, the literature review provided trends from other researchers for the author to investigate in the given apparatus. Results from the experiments indicate that mixtures provide competitive traits to standard working fluids, in agreement with the literature, specifically in the HEX utilized. Furthermore, the comparison of working fluids experimentally is relatively novel within the literature. Although the DPFHX experiments did not yield favorable results, the considerations garnered from the results will be tremendously useful in forthcoming work.

4.2 Future Work

The author's future work will continue with the concept of the DPFHX. However, the author will design a HEX specifically for the application of WHR from the single-cylinder Yanmar test

engine. Thus, the results and lessons from the work completed in this thesis provide the foundation for these efforts. As indicated in the literature review, tailoring an RC system to the specific application is the primary way to optimize performance and efficiency, validating the methodology moving forward.

Additionally, the trends in the selection of working fluids in the literature, as well as the experimental results, display the importance of working fluid selection and justification for the use of working fluid mixtures. Ideally, various working fluids can be compared within the HEX through both 3-D models and experiments, providing valuable correlations between model trends and experimental validation, while also corroborating the results of the heat transfer correlations. Furthermore, the 3-D heat transfer modeling of the devices and the subsequent performance of working fluids can aid in the selection and comparison of working fluids prior to experiments, providing an additional tier of metrics with which to compare the fluids on top of the thermodynamic, safety, and practical considerations utilized in this thesis.

From the experimental results of Chapter 3, many recommendations can be taken into consideration regarding future designs of the HEX itself. Based on the in-cylinder pressure data from the experiments conducted in this thesis, the sizing of the HEX should be made as compact as possible to mitigate the pressure drop across it, decreasing its potential influence on engine performance, and further enhancing the fuel efficiency savings. This becomes progressively more important if using DPF cores within the HEX, due to the added complexity of its induced backpressure. The compact sizing of the HEX also means less thermal mass within the system allowing for more realistic and achievable steady-state conditions during experimental testing.

Furthermore, a compact HEX will maximize the available heat transfer area while minimizing the required installation footprint and weight. With such attention to the HEX design, the engine can run at higher loads, thereby increasing the quantity of waste heat to retrieve.

Moreover, based on the difficulties faced in analyzing the heat transfer pathways and convection within the current apparatus, the need for additional instrumentation is apparent. By better capturing the states of the flows entering and exiting the HEX, within the HEX itself, and on the HEX's exterior, the state of each fluid and the losses occurring can be more appropriately described. This was most vividly illustrated through the unknown losses between where the inlet and outlet measurements were being taken and the shell of the HEX itself (i.e., in the tubing and reducers).

If compact sizing of the HEX is achieved, not only will insulation of the apparatus be easier, but it will also be possible to enclose the apparatus in a box to reduce ambient losses via free external convection, as well as provide the ability to better define such losses via measurements of the thermophysical state within such an enclosure. By being able to identify and ideally quantify losses to the ambient, in conjunction with additional data regarding the flow entering, leaving, and within the system, the heat transfer pathways can be more accurately described; thus, ideally improving upon many of the failures encountered during the analysis attempted in this thesis. Experimentally, additional trials for each working fluid should be conducted, to improve the repeatability of the experiments.

Furthermore, the new HEX will be manufactured using AM, allowing for the HEX to be formed with materials such as magnesium or titanium, commonly used in AM, providing better

thermal characteristics of the HEX and the potential for supplementary changes in thermal properties from the manufacturing process. Additionally, AM is known for its ability to reduce the weight of a component compared to its traditionally manufactured counterpart, a significant benefit for a technology with on-board vehicle applications, as the reduction in weight will provide improved fuel efficiency savings.

Finally, the current work and future iterations focus only on the HEX component of an RC WHR system. In order to achieve the fuel consumption benefits for which an RC WHR system is desired, the entire cycle is required. Thus, beyond the scope of optimizing the capture of the waste heat from engine exhaust, additional components in the RC must also be individually researched and optimized, before implementing the entire system. Once this has been completed, the full employment of an RC for its intended purpose can be realized. Nonetheless, the work and conclusions in this thesis set the stage for such efforts in the future.

References

1. Heywood, J.B., *Internal Combustion Engine Fundamentals.* 1988.

2. Johnson, K.G., K. Mollenhauer, and H. Tschöke, *Handbook of Diesel Engines*. 2010: Springer Science & Business Media.

3. Jabłońska, M. and R. Palkovits, *Copper Based Catalysts for the Selective Ammonia Oxidation into Nitrogen and Water Vapour — Recent Trends and Open Challenges.* Applied Catalysis B: Environmental, 2016. 181: pp. 332-351.

4. Mohankumar, S. and P. Senthilkumar, *Particulate Matter Formation and Its Control Methodologies for Diesel Engine: A Comprehensive Review.* Renewable and Sustainable Energy Reviews, 2017. 80: pp. 1227-1238.

5. Hashimoto, S., Y. Miyairi, T. Hamanaka, R. Matsubara, T. Harada, and S. Miwa, *SiC and Cordierite Diesel Particulate Filters Designed for Low Pressure Drop and Catalyzed, Uncatalyzed Systems.* SAE Transactions, 2002: pp. 118-131.

6. Konstandopoulos, A.G., E. Skaperdas, and M. Masoudi, *Inertial Contributions to the Pressure Drop of Diesel Particulate Filters.* SAE Technical Paper, 2001. 2001-01-0909.

7. Depcik, C., B. Spickler, and A. Gaire, *Revisiting the Single Equation Pressure Drop Model for Particulate Filters.* SAE Technical Paper, 2018. 2018-01-0952.

8. England, S.B., C.J. Rutland, D.E. Foster, and Y. He, *Investigation of the Effect of DPF Loading and Passive Regeneration on Engine Performance and Emissions Using an Integrated System Simulation.* SAE Technical Paper, 2006. 2006-01-0263.

9. Dawei, Q., L. Jun, and L. Yu, *Research on Particulate Filter Simulation and Regeneration Control Strategy.* Mechanical Systems and Signal Processing, 2017. 87: pp. 214-226.

10. Zhan, R., Y. Huang, and M. Khair, *Methodologies to Control DPF Uncontrolled Regenerations.* SAE Technical Paper, 2006. 2006-01-1090.

11. EPA, *Regulatory Announcement: Cutting Carbon Pollution, Improving Fuel Efficiency, Saving Money, and Supporting Innovation for Trucks*. 2015, EPA-420-F-15-900.

12. Stone, D.L., M., *Fuel Consumption and Greenhouse Gas Emissions Phase 2 Standards for Medium- and Heavy-Duty Vehicles.* EIA Annual Energy Outlook 2016(DOE/EIA-0383(2016)).

13. Adler, J. and T. Bandhauer, *Performance of a Diesel Engine at High Coolant Temperatures.* Journal of Energy Resources Technology, 2017. 139(6): pp. 062203.

14. Bailey, M.M., *Comparative Evaluation of Three Alternative Power Cycles for Waste Heat Recovery from the Exhaust of Adiabatic Diesel Engines.* NASA, 1985.

15. Badr, O., S. Naik, P. O'Callaghan, and S. Probert, *Expansion Machine for a Low Power-Output Steam Rankine-Cycle Engine.* Applied Energy, 1991. 39(2): pp. 93-116.

16. Sprouse III, C. and C. Depcik, *Review of Organic Rankine Cycles for Internal Combustion Engine Exhaust Waste Heat Recovery.* Applied Thermal Engineering, 2013. 51(1-2): pp. 711-722.

17. Tchanche, B.F., G. Lambrinos, A. Frangoudakis, and G. Papadakis, *Low-Grade Heat Conversion into Power Using Organic Rankine Cycles – A Review of Various Applications.* Renewable and Sustainable Energy Reviews, 2011. 15(8): pp. 3963-3979.

18. Chintala, V., S. Kumar, and J.K. Pandey, *A Technical Review on Waste Heat Recovery from Compression Ignition Engines Using Organic Rankine Cycle.* Renewable and Sustainable Energy Reviews, 2018. 81: pp. 493-509.

19. Jacobs, T.J., *Waste Heat Recovery Potential of Advanced Internal Combustion Engine Technologies.* Journal of Energy Resources Technology, 2015. 137(4): pp. 042004.

20. Sprouse III, C.E., *Combined Diesel Particulate Filter/Heat Exchanger for Engine Exhaust Waste Heat Recovery with Organic Rankine Cycle*. 2016, University of Kansas.

21. Shu, G., J. Zhao, H. Tian, H. Wei, X. Liang, G. Yu, and L. Liu, *Theoretical Analysis of Engine Waste Heat Recovery by the Combined Thermo-Generator and Organic Rankine Cycle System.* SAE Technical Paper, 2012. 2012-01-0636.

22. Pradhan, S., A. Thiruvengadam, P. Thiruvengadam, M.C. Besch, and D. Carder, *Investigating the Potential of Waste Heat Recovery as a Pathway for Heavy-Duty Exhaust Aftertreatment Thermal Management.* SAE Technical Paper, 2015. 2015-01-1606.

23. Moran Michael, J. and N. Shapiro Howard, *Fundamentals of Engineering Thermodynamics, 5th Edition* 2004 John Wiley & Sons, Inc.

24. Xu, Z., J. Liu, F. Jianqin, and C. Ren, *Analysis and Comparison of Typical Exhaust Gas Energy Recovery Bottoming Cycles.* SAE Technical Paper, 2013. 2013-01-1648.

25. Lu, Y., A.P. Roskilly, X. Yu, K. Tang, L. Jiang, A. Smallbone, L. Chen, and Y. Wang, *Parametric Study for Small Scale Engine Coolant and Exhaust Heat Recovery System Using Different Organic Rankine Cycle Layouts.* Applied Thermal Engineering, 2017. 127: pp. 1252-1266.

26. Zhou, F., E. Dede, and S. Joshi, *Application of Rankine Cycle to Passenger Vehicle Waste Heat Recovery - A Review.* SAE International Journal of Materials and Manufacturing, 2016. 9(2): pp. 224-235.

27. Peris, B., J. Navarro-Esbrí, and F. Molés, *Bottoming Organic Rankine Cycle Configurations to Increase Internal Combustion Engines Power Output from Cooling Water Waste Heat Recovery.* Applied Thermal Engineering, 2013. 61(2): pp. 364-371.

28. Ryms, M., T. Pyś, and E. Klugmann-Radziemska, *Adapting the Pinch Point Analysis to Improve the ORC Design Process.* International Journal of Energy Research, 2014. 38(1): pp. 29-40.

29. Bergman, T.L., F.P. Incropera, D.P. DeWitt, and A.S. Lavine, *Fundamentals of Heat and Mass Transfer*. 2011: John Wiley & Sons.

30. Tian, H., G. Shu, H. Wei, X. Liang, and L. Liu, *Fluids and Parameters Optimization for the Organic Rankine Cycles (ORCs) Used in Exhaust Heat Recovery of Internal Combustion Engine (ICE).* Energy, 2012. 47(1): pp. 125-136.

31. Hajabdollahi, Z., F. Hajabdollahi, M. Tehrani, and H. Hajabdollahi, *Thermo-Economic Environmental Optimization of Organic Rankine Cycle for Diesel Waste Heat Recovery.* Energy, 2013. 63: pp. 142-151.

32. Yang, M.-H., *Thermal and Economic Analyses of a Compact Waste Heat Recovering System for the Marine Diesel Engine Using Transcritical Rankine Cycle.* Energy Conversion and Management, 2015. 106: pp. 1082-1096.

33. Yang, F., H. Zhang, S. Song, C. Bei, H. Wang, and E. Wang, *Thermoeconomic Multi-Objective Optimization of an Organic Rankine Cycle for Exhaust Waste Heat Recovery of a Diesel Engine.* Energy, 2015. 93: pp. 2208-2228.

34. de Oliveira Neto, R., C.A.R. Sotomonte, C.J. Coronado, and M.A. Nascimento, *Technical and Economic Analyses of Waste Heat Energy Recovery from Internal Combustion Engines by the Organic Rankine Cycle.* Energy Conversion and Management, 2016. 129: pp. 168-179.

35. Bao, J. and L. Zhao, *A Review of Working Fluid and Expander Selections for Organic Rankine Cycle.* Renewable and Sustainable Energy Reviews, 2013. 24: pp. 325-342.

36. Imran, M., F. Haglind, M. Asim, and J.Z. Alvi, *Recent Research Trends in Organic Rankine Cycle Technology: A Bibliometric Approach.* Renewable and Sustainable Energy Reviews, 2018. 81: pp. 552-562.

37. Morgan, D., P. Patel, E. Doyle, R. Raymond, R. Sakhuja, and K. Barber. *Laboratory Test Results, Low Emission Ranking-Cycle Engine with Organic-Based Working Fluid and Reciprocating Expander for Automobiles*. in 8th Intersociety Energy Conversion Engineering Conference, Proceedings. 1973. Philadelphia: pp 158-164, 739062.

38. Patel, P.S. and E.F. Doyle, *Compounding the Truck Diesel Engine with an Organic Rankine-Cycle System.* SAE Technical Paper, 1976. 760343.

39. Wang, J., Y. Dai, and L. Gao, *Exergy Analyses and Parametric Optimizations for Different Cogeneration Power Plants in Cement Industry.* Applied Energy, 2009. 86(6): pp. 941-948.

40. Ringler, J., M. Seifert, V. Guyotot, and W. Hübner, *Rankine Cycle for Waste Heat Recovery of IC Engines.* SAE International Journal of Engines, 2009. 2(1): pp. 67-76.

41. Vaja, I. and A. Gambarotta, *Internal Combustion Engine (ICE) Bottoming with Organic Rankine Cycles (ORCs).* Energy, 2010. 35(2): pp. 1084-1093.

42. Teng, H., G. Regner, and C. Cowland, *Waste Heat Recovery of Heavy-Duty Diesel Engines by Organic Rankine Cycle Part I: Hybrid Energy System of Diesel and Rankine Engines.* SAE Technical Paper, 2007. 2007-01-0537.

43. Espinosa, N., L. Tilman, V. Lemort, S. Quoilin, and B. Lombard, *Rankine Cycle for Waste Heat Recovery on Commercial Trucks: Approach, Constraints and Modelling.* 2010.

44. Arias, D.A., T.A. Shedd, and R.K. Jester, *Theoretical Analysis of Waste Heat Recovery from an Internal Combustion Engine in a Hybrid Vehicle.* SAE Technical Paper, 2006. 2006-01-1605.

45. Oomori, H. and S. Ogino, *Waste Heat Recovery of Passenger Car Using a Combination of Rankine Bottoming Cycle and Evaporative Engine Cooling System.* SAE International, 1993. 930880.

46. Badr, O., P. O'Callaghan, and S. Probert, *Thermodynamic and Thermophysical Properties of Organic Working Fluids for Rankine-Cycle Engines.* Applied Energy, 1985. 19(1): pp. 1-40.

47. Hung, T.-C., *Waste Heat Recovery of Organic Rankine Cycle Using Dry Fluids.* Energy Conversion and Management, 2001. 42(5): pp. 539-553.

48. Liu, B.-T., K.-H. Chien, and C.-C. Wang, *Effect of Working Fluids on Organic Rankine Cycle for Waste Heat Recovery.* Energy, 2004. 29(8): pp. 1207-1217.

49. Mago, P., L. Chamra, and C. Somayaji, *Performance Analysis of Different Working Fluids for Use in Organic Rankine Cycles.* Proceedings of the Institution of Mechanical Engineers, Part A: Journal of Power and Energy, 2007. 221(3): pp. 255-263.

50. Quoilin, S., S. Declaye, B.F. Tchanche, and V. Lemort, *Thermo-Economic Optimization of Waste Heat Recovery Organic Rankine Cycles.* Applied Thermal Engineering, 2011. 31(14-15): pp. 2885-2893.

51. El Chammas, R. and D. Clodic, *Combined Cycle for Hybrid Vehicles.* SAE Technical Paper, 2005. 2005-01-1171.

52. Stobart, R. and R. Weerasinghe, *Heat Recovery and Bottoming Cycles for SI and CI Engines - A Perspective.* SAE Technical Paper, 2006. 2006-01-0662.

53. Leibowitz, H., I. Smith, and N. Stosic. *Cost Effective Small Scale ORC Systems for Power Recovery from Low Grade Heat Sources*. in ASME 2006 International Mechanical Engineering Congress and Exposition. 2006. American Society of Mechanical Engineers.

54. Marciniak, T., J. Krazinski, J. Bratis, H. Bushby, and E. Buyco, *Comparison of Rankine-Cycle Power Systems: Effects of Seven Working Fluids*. 1981, Argonne National Lab., IL (USA).

55. Boretti, A., *Improving the Efficiency of Turbocharged Spark Ignition Engines for Passenger Cars through Waste Heat Recovery.* SAE Technical Paper, 2012. 2012-01-0388.

56. Latz, G., S. Andersson, and K. Munch, *Comparison of Working Fluids in Both Subcritical and Supercritical Rankine Cycles for Waste-Heat Recovery Systems in Heavy-Duty Vehicles.* SAE Technical Paper, 2012. 2012-01-1200.

57. Arunachalam, P.N., M. Shen, M. Tuner, P. Tunestal, and M. Thern, *Waste Heat Recovery from Multiple Heat Sources in a HD Truck Diesel Engine Using a Rankine Cycle - A Theoretical Evaluation.* SAE Technical Paper, 2012. 2012-01-1602.

58. Boretti, A., A. Osman, and I. Aris, *Design of Rankine Cycle Systems to Deliver Fuel Economy Benefits over Cold Start Driving Cycles.* SAE Technical Paper, 2012. 2012-01-1713.

59. Lopes, J., R. Douglas, G. McCullough, R. O'Shaughnessy, A. Hanna, C. Rouaud, and R. Seaman, *Review of Rankine Cycle Systems Components for Hybrid Engines Waste Heat Recovery.* SAE Technical Paper, 2012. 2012-01-1942.

60. Dolz, V., R. Novella, A. García, and J. Sánchez, *HD Diesel Engine Equipped with a Bottoming Rankine Cycle as a Waste Heat Recovery System. Part 1: Study and Analysis of the Waste Heat Energy.* Applied Thermal Engineering, 2012. 36: pp. 269-278.

61. Serrano, J., V. Dolz, R. Novella, and A. Garcia, *Hd Diesel Engine Equipped with a Bottoming Rankine Cycle as a Waste Heat Recovery System. Part 2: Evaluation of Alternative Solutions.* Applied Thermal Engineering, 2012. 36: pp. 279-287.

62. Boretti, A., *Recovery of Exhaust and Coolant Heat with R245fa Organic Rankine Cycles in a Hybrid Passenger Car with a Naturally Aspirated Gasoline Engine.* Applied Thermal Engineering, 2012. 36: pp. 73-77.

63. Boretti, A.A., *Transient Operation of Internal Combustion Engines with Rankine Waste Heat Recovery Systems.* Applied Thermal Engineering, 2012. 48: pp. 18-23.

64. Xie, H. and C. Yang, *Dynamic Behavior of Rankine Cycle System for Waste Heat Recovery of Heavy Duty Diesel Engines under Driving Cycle.* Applied Energy, 2013. 112: pp. 130-141.

65. Shu, G.-Q., G. Yu, H. Wei, and X. Liang, *Simulations of a Bottoming Organic Rankine Cycle (ORC) Driven by Waste Heat in a Diesel Engine (DE).* SAE Technical Paper, 2013. 2013-01-0851.

66. Tian, H., G.-Q. Shu, H. Wei, X. Liang, and G. Yu, *Thermodynamic Analysis of a Novel Combined Power and Cooling Cycle Driven by the Exhaust Heat Form a Diesel Engine.* SAE International Journal of Engines, 2013. 6(2): pp. 766-776.

67. Jung, D., S. Park, and K. Min, *Study on the Application of the Waste Heat Recovery System to Heavy-Duty Series Hybrid Electric Vehicles.* SAE Technical Paper, 2013. 2013-01-1455.

68. Yamaguchi, T., Y. Aoyagi, H. Osada, K. Shimada, and N. Uchida, *BSFC Improvement by Diesel-Rankine Combined Cycle in the High EGR Rate and High Boosted Diesel Engine.* SAE International Journal of Engines, 2013. 6(2): pp. 1275-1286.

69. Hossain, S.N. and S. Bari, *Additional Power Generation from the Exhaust Gas of Diesel Engine by Bottoming Rankine Cycle.* SAE Technical Paper, 2013. 2013-01-1639.

70. Domingues, A., H. Santos, and M. Costa, *Analysis of Vehicle Exhaust Waste Heat Recovery Potential Using a Rankine Cycle.* Energy, 2013. 49: pp. 71-85.

71. Zhu, S., K. Deng, and S. Qu, *Energy and Exergy Analyses of a Bottoming Rankine Cycle for Engine Exhaust Heat Recovery.* Energy, 2013. 58: pp. 448-457.

72. Shu, G., L. Liu, H. Tian, H. Wei, and Y. Liang, *Analysis of Regenerative Dual-Loop Organic Rankine Cycles (DORCs) Used in Engine Waste Heat Recovery.* Energy Conversion and Management, 2013. 76: pp. 234-243.

73. Shu, G., L. Liu, H. Tian, H. Wei, and G. Yu, *Parametric and Working Fluid Analysis of a Dual-Loop Organic Rankine Cycle (DORC) Used in Engine Waste Heat Recovery.* Applied Energy, 2014. 113: pp. 1188-1198.

74. Zhang, C., G.-Q. Shu, H. Tian, H. Wei, G. Yu, and Y. Liang, *Theoretical Analysis of a Combined Thermoelectric Generator (TEG) and Dual-Loop Organic Rankine Cycle (DORC) System Using for Engines' Exhaust Waste Heat Recovery.* SAE Technical Paper, 2014. 2014-01-0670.

75. Yang, C., H. Xie, and S. Zhou, *Efficiency Analysis of the Rankine Cycle System Used for Engine Exhaust Energy Recovery under Driving Cycle.* SAE Technical Paper, 2014. 2014-01-0671.

76. Bari, S. and S. Rubaiyat, *Additional Power Generation from the Exhaust Gas of a Diesel Engine Using Ammonia as the Working Fluid.* SAE Technical Paper, 2014. 2014-01-0677.

77. Furukawa, T., M. Nakamura, K. Machida, and K. Shimokawa, *A Study of the Rankine Cycle Generating System for Heavy Duty HV Trucks.* SAE Technical Paper, 2014. 2014-01-0678.

78. Dickson, J., M. Ellis, T. Rousseau, and J. Smith, *Validation and Design of Heavy Vehicle Cooling System with Waste Heat Recovery Condenser.* SAE International Journal of Commercial Vehicles, 2014. 7(2014-01-2339): pp. 458-467.

79. Jin, L., G. Tan, X. Guo, R. Nie, J. Cai, and X. Shen, *Evaporator Boiling Heat Transfer Analysis for Engine Exhaust Heat Recovery.* SAE Technical Paper, 2014. 2014-01-2345.

80. Han, Y., J. Kang, X. Wang, Y. Chen, and Z. Hu, *The Effect of Cylinder Clearance on Output Work of ORC-FP Used in Waste Energy Recovery.* SAE Technical Paper, 2014. 2014-01-2563.

81. Hatami, M., D. Ganji, and M. Gorji-Bandpy, *A Review of Different Heat Exchangers Designs for Increasing the Diesel Exhaust Waste Heat Recovery.* Renewable and Sustainable Energy Reviews, 2014. 37: pp. 168-181.

82. Yue, C., D. Han, and W. Pu, *Analysis of the Integrated Characteristics of the CPS (Combined Power System) of a Bottoming Organic Rankine Cycle and a Diesel Engine.* Energy, 2014. 72: pp. 739-751.

83. Long, R., Y. Bao, X. Huang, and W. Liu, *Exergy Analysis and Working Fluid Selection of Organic Rankine Cycle for Low Grade Waste Heat Recovery.* Energy, 2014. 73: pp. 475-483.

84. Zhang, Y.-Q., Y.-T. Wu, G.-D. Xia, C.-F. Ma, W.-N. Ji, S.-W. Liu, K. Yang, and F.-B. Yang, *Development and Experimental Study on Organic Rankine Cycle System with Single-Screw Expander for Waste Heat Recovery from Exhaust of Diesel Engine.* Energy, 2014. 77: pp. 499-508.

85. Yang, F., X. Dong, H. Zhang, Z. Wang, K. Yang, J. Zhang, E. Wang, H. Liu, and G. Zhao, *Performance Analysis of Waste Heat Recovery with a Dual Loop Organic Rankine Cycle (ORC) System for Diesel Engine under Various Operating Conditions.* Energy Conversion and Management, 2014. 80: pp. 243-255.

86. Hou, G., S. Bi, M. Lin, J. Zhang, and J. Xu, *Minimum Variance Control of Organic Rankine Cycle Based Waste Heat Recovery.* Energy Conversion and Management, 2014. 86: pp. 576-586.

87. Muhammad, U., M. Imran, D.H. Lee, and B.S. Park, *Design and Experimental Investigation of a 1 kW Organic Rankine Cycle System Using R245fa as Working Fluid*

for Low-Grade Waste Heat Recovery from Steam. Energy Conversion and Management, 2015. 103: pp. 1089-1100.

88. Galindo, J., S. Ruiz, V. Dolz, L. Royo-Pascual, R. Haller, B. Nicolas, and Y. Glavatskaya, *Experimental and Thermodynamic Analysis of a Bottoming Organic Rankine Cycle (ORC) of Gasoline Engine Using Swash-Plate Expander.* Energy Conversion and Management, 2015. 103: pp. 519-532.

89. Feng, Y., T. Hung, K. Greg, Y. Zhang, B. Li, and J. Yang, *Thermoeconomic Comparison between Pure and Mixture Working Fluids of Organic Rankine Cycles (ORCs) for Low Temperature Waste Heat Recovery.* Energy Conversion and Management, 2015. 106: pp. 859-872.

90. Baldi, F., U. Larsen, and C. Gabrielii, *Comparison of Different Procedures for the Optimisation of a Combined Diesel Engine and Organic Rankine Cycle System Based on Ship Operational Profile.* Ocean Engineering, 2015. 110: pp. 85-93.

91. Esposito, M.C., N. Pompini, A. Gambarotta, V. Chandrasekaran, J. Zhou, and M. Canova, *Nonlinear Model Predictive Control of an Organic Rankine Cycle for Exhaust Waste Heat Recovery in Automotive Engines.* IFAC-PapersOnLine, 2015. 48(15): pp. 411-418.

92. Song, J. and C.-w. Gu, *Performance Analysis of a Dual-Loop Organic Rankine Cycle (ORC) System with Wet Steam Expansion for Engine Waste Heat Recovery.* Applied Energy, 2015. 156: pp. 280-289.

93. Yamaguchi, T., Y. Aoyagi, N. Uchida, A. Fukunaga, M. Kobayashi, T. Adachi, and M. Hashimoto, *Fundamental Study of Waste Heat Recovery in the High Boosted 6-Cylinder Heavy Duty Diesel Engine.* SAE International Journal of Materials and Manufacturing, 2015. 8(2): pp. 209-226.

94. Allouache, A., S. Leggett, M.J. Hall, M. Tu, C. Baker, and H. Fateh, *Simulation of Organic Rankine Cycle Power Generation with Exhaust Heat Recovery from a 15 Liter Diesel Engine.* SAE International Journal of Materials and Manufacturing, 2015. 8(2): pp. 227-238.

95. Shen, X., G. Tan, Q. Zhou, Z. Yang, and M. Hua, *The Organic Medium Physical State Analysis for Engine Exhaust Thermal Recovery.* SAE Technical Paper, 2015. 2015-01-1610.

96. Eichler, K., Y. Jeihouni, and C. Ritterskamp, *Fuel Economy Benefits for Commercial Diesel Engines with Waste Heat Recovery.* SAE International Journal of Commercial Vehicles, 2015. 8(2015-01-2807): pp. 491-505.

97. Kulkarni, K. and A. Sood, *Performance Analysis of Organic Rankine Cycle (ORC) for Recovering Waste Heat from a Heavy Duty Diesel Engine.* SAE Technical Paper, 2015. 2015-26-0037.

98. Kölsch, B. and J. Radulovic, *Utilisation of Diesel Engine Waste Heat by Organic Rankine Cycle.* Applied Thermal Engineering, 2015. 78: pp. 437-448.

99. Amicabile, S., J.-I. Lee, and D. Kum, *A Comprehensive Design Methodology of Organic Rankine Cycles for the Waste Heat Recovery of Automotive Heavy-Duty Diesel Engines.* Applied Thermal Engineering, 2015. 87: pp. 574-585.

100. Song, J. and C.-w. Gu, *Analysis of ORC (Organic Rankine Cycle) Systems with Pure Hydrocarbons and Mixtures of Hydrocarbon and Retardant for Engine Waste Heat Recovery.* Applied Thermal Engineering, 2015. 89: pp. 693-702.

101. Glover, S., R. Douglas, M. De Rosa, X. Zhang, and L. Glover, *Simulation of a Multiple Heat Source Supercritical ORC (Organic Rankine Cycle) for Vehicle Waste Heat Recovery.* Energy, 2015. 93: pp. 1568-1580.

102. Shi, R., T. He, J. Peng, Y. Zhang, and W. Zhuge, *System Design and Control for Waste Heat Recovery of Automotive Engines Based on Organic Rankine Cycle.* Energy, 2016. 102: pp. 276-286.

103. Ma, J., L. Liu, T. Zhu, and T. Zhang, *Cascade Utilization of Exhaust Gas and Jacket Water Waste Heat from an Internal Combustion Engine by a Single Loop Organic Rankine Cycle System.* Applied Thermal Engineering, 2016. 107: pp. 218-226.

104. Khaljani, M., R.K. Saray, and K. Bahlouli, *Evaluation of a Combined Cycle Based on an HCCI (Homogenous Charge Compression Ignition) Engine Heat Recovery Employing Two Organic Rankine Cycles.* Energy, 2016. 107: pp. 748-760.

105. Shu, G., X. Wang, and H. Tian, *Theoretical Analysis and Comparison of Rankine Cycle and Different Organic Rankine Cycles as Waste Heat Recovery System for a Large Gaseous Fuel Internal Combustion Engine.* Applied Thermal Engineering, 2016. 108: pp. 525-537.

106. Shu, G., G. Yu, H. Tian, H. Wei, X. Liang, and Z. Huang, *Multi-Approach Evaluations of a Cascade-Organic Rankine Cycle (C-ORC) System Driven by Diesel Engine Waste Heat: Part A – Thermodynamic Evaluations.* Energy Conversion and Management, 2016. 108: pp. 579-595.

107. Yu, G., G. Shu, H. Tian, H. Wei, and X. Liang, *Multi-Approach Evaluations of a Cascade-Organic Rankine Cycle (C-ORC) System Driven by Diesel Engine Waste Heat: Part B - Techno-Economic Evaluations.* Energy Conversion and Management, 2016. 108: pp. 596-608.

108. Yağlı, H., Y. Koç, A. Koç, A. Görgülü, and A. Tandiroğlu, *Parametric Optimization and Exergetic Analysis Comparison of Subcritical and Supercritical Organic Rankine Cycle (ORC) for Biogas Fuelled Combined Heat and Power (CHP) Engine Exhaust Gas Waste Heat.* Energy, 2016. 111: pp. 923-932.

109. Yang, M.-H., *Optimizations of the Waste Heat Recovery System for a Large Marine Diesel Engine Based on Transcritical Rankine Cycle.* Energy, 2016. 113: pp. 1109-1124.

110. Shu, G., M. Zhao, H. Tian, Y. Huo, and W. Zhu, *Experimental Comparison of R123 and R245fa as Working Fluids for Waste Heat Recovery from Heavy-Duty Diesel Engine.* Energy, 2016. 115: pp. 756-769.

111. Zhang, T., T. Zhu, W. An, X. Song, L. Liu, and H. Liu, *Unsteady Analysis of a Bottoming Organic Rankine Cycle for Exhaust Heat Recovery from an Internal Combustion Engine Using Monte Carlo Simulation.* Energy Conversion and Management, 2016. 124: pp. 357-368.

112. Torregrosa, A., J. Galindo, V. Dolz, L. Royo-Pascual, R. Haller, and J. Melis, *Dynamic Tests and Adaptive Control of a Bottoming Organic Rankine Cycle of IC Engine Using Swash-Plate Expander.* Energy Conversion and Management, 2016. 126: pp. 168-176.

113. Galindo, J., S. Ruiz, V. Dolz, and L. Royo-Pascual, *Advanced Exergy Analysis for a Bottoming Organic Rankine Cycle Coupled to an Internal Combustion Engine.* Energy Conversion and Management, 2016. 126: pp. 217-227.

114. Galindo, J., H. Climent, V. Dolz, and L. Royo-Pascual, *Multi-Objective Optimization of a Bottoming Organic Rankine Cycle (ORC) of Gasoline Engine Using Swash-Plate Expander.* Energy Conversion and Management, 2016. 126: pp. 1054-1065.

115. Uusitalo, A., V. Uusitalo, A. Grönman, M. Luoranen, and A. Jaatinen-Värri, *Greenhouse Gas Reduction Potential by Producing Electricity from Biogas Engine Waste Heat Using Organic Rankine Cycle.* Journal of Cleaner Production, 2016. 127: pp. 399-405.

116. Xia, J., J. Wang, J. Lou, P. Zhao, and Y. Dai, *Thermo-Economic Analysis and Optimization of a Combined Cooling and Power (CCP) System for Engine Waste Heat Recovery.* Energy Conversion and Management, 2016. 128: pp. 303-316.

117. Yu, G., G. Shu, H. Tian, Y. Huo, and W. Zhu, *Experimental Investigations on a Cascaded Steam-/Organic-Rankine-Cycle (RC/ORC) System for Waste Heat Recovery (WHR) from Diesel Engine.* Energy Conversion and Management, 2016. 129: pp. 43-51.

118. Grelet, V., T. Reiche, V. Lemort, M. Nadri, and P. Dufour, *Transient Performance Evaluation of Waste Heat Recovery Rankine Cycle Based System for Heavy Duty Trucks.* Applied Energy, 2016. 165: pp. 878-892.

119. Morgan, R., G. Dong, A. Panesar, and M. Heikal, *A Comparative Study between a Rankine Cycle and a Novel Intra-Cycle Based Waste Heat Recovery Concepts Applied to an Internal Combustion Engine.* Applied Energy, 2016. 174: pp. 108-117.

120. Shu, G., L. Shi, H. Tian, X. Li, G. Huang, and L. Chang, *An Improved CO_2-Based Transcritical Rankine Cycle (CTRC) Used for Engine Waste Heat Recovery.* Applied Energy, 2016. 176: pp. 171-182.

121. Ziviani, D., S. Gusev, S. Lecompte, E. Groll, J. Braun, W.T. Horton, M. van den Broek, and M. De Paepe, *Characterizing the Performance of a Single-Screw Expander in a Small-Scale Organic Rankine Cycle for Waste Heat Recovery.* Applied Energy, 2016. 181: pp. 155-170.

122. Xu, B., X. Liu, J. Shutty, P. Anschel, S. Onori, Z. Filipi, and M. Hoffman, *Physics-Based Modeling and Transient Validation of an Organic Rankine Cycle Waste Heat Recovery System for a Heavy-Duty Diesel Engine.* SAE Technical Paper, 2016. 2016-01-0199.

123. De Rosa, M., R. Douglas, and S. Glover, *Numerical Analysis on a Dual-Loop Waste Heat Recovery System Coupled with an ORC for Vehicle Applications.* SAE Technical Paper, 2016. 2016-01-0205.

124. Cipollone, R., D. Di Battista, A. Perosino, and F. Bettoja, *Waste Heat Recovery by an Organic Rankine Cycle for Heavy Duty Vehicles.* SAE Technical Paper, 2016. 2016-01-0234.

125. Shu, G.-Q., X. Wang, and H. Tian, *The Performance of Rankine Cycle as Waste Heat Recovery System for a Natural Gas Engine at Variable Working Conditions.* SAE Technical Paper, 2016. 2016-01-0237.

126. Wiedemann, J. and R. Span, *Simulation of an Exhaust Heat Driven Rankine-Cycle for Heavy-Duty Diesel Engines.* Energy Procedia, 2016. 88: pp. 531-536.

127. Kim, Y.M., D.G. Shin, C.G. Kim, and G.B. Cho, *Single-Loop Organic Rankine Cycles for Engine Waste Heat Recovery Using Both Low-and High-Temperature Heat Sources.* Energy, 2016. 96: pp. 482-494.

128. Hærvig, J., K. Sørensen, and T.J. Condra, *Guidelines for Optimal Selection of Working Fluid for an Organic Rankine Cycle in Relation to Waste Heat Recovery.* Energy, 2016. 96: pp. 592-602.

129. Lu, Y., A.P. Roskilly, A. Smallbone, X. Yu, and Y. Wang, *Design and Parametric Study of an Organic Rankine Cycle Using a Scroll Expander for Engine Waste Heat Recovery.* Energy Procedia, 2017. 105: pp. 1420-1425.

130. Li, L., Y. Ge, and S. Tassou, *Experimental Study on a Small-Scale R245fa Organic Rankine Cycle System for Low-Grade Thermal Energy Recovery.* Energy Procedia, 2017. 105: pp. 1827-1832.

131. Yu, H., J. Eason, L.T. Biegler, and X. Feng, *Simultaneous Heat Integration and Techno-Economic Optimization of Organic Rankine Cycle (ORC) for Multiple Waste Heat Stream Recovery.* Energy, 2017. 119: pp. 322-333.

132. Lu, Y., A.P. Roskilly, L. Jiang, and X. Yu, *Working Fluid Selection for a Small-Scale Organic Rankine Cycle Recovering Engine Waste Heat.* Energy Procedia, 2017. 123: pp. 346-352.

133. Wang, X., G. Shu, H. Tian, P. Liu, X. Li, and D. Jing, *Engine Working Condition Effects on the Dynamic Response of Organic Rankine Cycle as Exhaust Waste Heat Recovery System.* Applied Thermal Engineering, 2017. 123: pp. 670-681.

134. Seyedkavoosi, S., S. Javan, and K. Kota, *Exergy-Based Optimization of an Organic Rankine Cycle (ORC) for Waste Heat Recovery from an Internal Combustion Engine (ICE).* Applied Thermal Engineering, 2017. 126: pp. 447-457.

135. Tian, Y., H. Zhang, G. Li, X. Hou, F. Yu, F. Yang, Y. Yang, and Y. Liu, *Experimental Study on Free Piston Linear Generator (FPLG) Used for Waste Heat Recovery of Vehicle Engine.* Applied Thermal Engineering, 2017. 127: pp. 184-193.

136. Kuboth, S., M. Neubert, M. Preißinger, and D. Brüggemann, *Iterative Approach for the Design of an Organic Rankine Cycle Based on Thermodynamic Process Simulations and a Small-Scale Test Rig.* Energy Procedia, 2017. 129: pp. 18-25.

137. Galindo, J., V. Dolz, L. Royo-Pascual, and A. Brizard, *Dynamic Modeling of an Organic Rankine Cycle to Recover Waste Heat for Transportation Vehicles.* Energy Procedia, 2017. 129: pp. 192-199.

138. Alshammari, F., A. Karvountzis-Kontakiotis, A. Pesiridis, and T. Minton, *Radial Expander Design for an Engine Organic Rankine Cycle Waste Heat Recovery System.* Energy Procedia, 2017. 129: pp. 285-292.

139. Kosuda, O., T. Hikichi, O. Kido, and N. Nishiyama, *Development of Air-Cooled Compact Organic Rankine Cycle Power Generation Technology Utilizing Waste Heat.* Energy Procedia, 2017. 129: pp. 559-566.

140. Bufi, E.A., S.M. Camporeale, and P. Cinnella, *Robust Optimization of an Organic Rankine Cycle for Heavy Duty Engine Waste Heat Recovery.* Energy Procedia, 2017. 129: pp. 66-73.

141. Zhao, M., G. Shu, H. Tian, F. Yan, G. Huang, and C. Hu, *The Investigation of the Recuperative Organic Rankine Cycle Models for the Waste Heat Recovery on Vehicles.* Energy Procedia, 2017. 129: pp. 732-739.

142. Rijpkema, J., K. Munch, and S.B. Andersson, *Thermodynamic Potential of Rankine and Flash Cycles for Waste Heat Recovery in a Heavy Duty Diesel Engine.* Energy Procedia, 2017. 129: pp. 746-753.

143. Lion, S., I. Vlaskos, C. Rouaud, and R. Taccani, *Overview of the Activities on Heavy Duty Diesel Engines Waste Heat Recovery with Organic Rankine Cycles (ORC) in the Frame of the ECCO-MATE EU FP7 Project.* Energy Procedia, 2017. 129: pp. 786-793.

144. Landelle, A., N. Tauveron, R. Revellin, P. Haberschill, and S. Colasson, *Experimental Investigation of a Transcritical Organic Rankine Cycle with Scroll Expander for Low—Temperature Waste Heat Recovery.* Energy Procedia, 2017. 129: pp. 810-817.

145. Shu, G., X. Wang, H. Tian, P. Liu, D. Jing, and X. Li, *Scan of Working Fluids Based on Dynamic Response Characters for Organic Rankine Cycle Using for Engine Waste Heat Recovery.* Energy, 2017. 133: pp. 609-620.

146. Pang, K.-C., S.-C. Chen, T.-C. Hung, Y.-Q. Feng, S.-C. Yang, K.-W. Wong, and J.-R. Lin, *Experimental Study on Organic Rankine Cycle Utilizing R245fa, R123 and Their Mixtures to Investigate the Maximum Power Generation from Low-Grade Heat.* Energy, 2017. 133: pp. 636-651.

147. Chen, T., W. Zhuge, Y. Zhang, and L. Zhang, *A Novel Cascade Organic Rankine Cycle (ORC) System for Waste Heat Recovery of Truck Diesel Engines.* Energy Conversion and Management, 2017. 138: pp. 210-223.

148. Lemmens, S. and S. Lecompte, *Case Study of an Organic Rankine Cycle Applied for Excess Heat Recovery: Technical, Economic and Policy Matters.* Energy Conversion and Management, 2017. 138: pp. 670-685.

149. Yang, M.-H., R.-H. Yeh, and T.-C. Hung, *Thermo-Economic Analysis of the Transcritical Organic Rankine Cycle Using R1234yf/R32 Mixtures as the Working Fluids for Lower-Grade Waste Heat Recovery.* Energy, 2017. 140: pp. 818-836.

150. Budisulistyo, D. and S. Krumdieck, *A Novel Design Methodology for Waste Heat Recovery Systems Using Organic Rankine Cycle.* Energy Conversion and Management, 2017. 142: pp. 1-12.

151. Feng, Y.-q., T.-C. Hung, Y.-L. He, Q. Wang, S. Wang, B.-x. Li, J.-R. Lin, and W. Zhang, *Operation Characteristic and Performance Comparison of Organic Rankine Cycle (ORC) for Low-Grade Waste Heat Using R245fa, R123 and Their Mixtures.* Energy Conversion and Management, 2017. 144: pp. 153-163.

152. Shu, G., P. Liu, H. Tian, X. Wang, and D. Jing, *Operational Profile Based Thermal-Economic Analysis on an Organic Rankine Cycle Using for Harvesting Marine Engine's Exhaust Waste Heat.* Energy Conversion and Management, 2017. 146: pp. 107-123.

153. Tian, H., L. Chang, G. Shu, and L. Shi, *Multi-Objective Optimization of the Carbon Dioxide Transcritical Power Cycle with Various Configurations for Engine Waste Heat Recovery.* Energy Conversion and Management, 2017. 148: pp. 477-488.

154. Shi, L., G. Shu, H. Tian, G. Huang, T. Chen, X. Li, and D. Li, *Experimental Comparison between Four CO_2-Based Transcritical Rankine Cycle (CTRC) Systems for Engine Waste Heat Recovery.* Energy Conversion and Management, 2017. 150: pp. 159-171.

155. Liu, H., H. Zhang, F. Yang, X. Hou, F. Yu, and S. Song, *Multi-Objective Optimization of Fin-and-Tube Evaporator for a Diesel Engine-Organic Rankine Cycle (ORC) Combined System Using Particle Swarm Optimization Algorithm.* Energy Conversion and Management, 2017. 151: pp. 147-157.

156. Kyriakidis, F., K. Sørensen, S. Singh, and T. Condra, *Modeling and Optimization of Integrated Exhaust Gas Recirculation and Multi-Stage Waste Heat Recovery in Marine Engines.* Energy Conversion and Management, 2017. 151: pp. 286-295.

157. Yang, M.-H., *The Performance Analysis of the Transcritical Rankine Cycle Using Carbon Dioxide Mixtures as the Working Fluids for Waste Heat Recovery.* Energy Conversion and Management, 2017. 151: pp. 86-97.

158. Mondejar, M.E., F. Ahlgren, M. Thern, and M. Genrup, *Quasi-Steady State Simulation of an Organic Rankine Cycle for Waste Heat Recovery in a Passenger Vessel.* Applied Energy, 2017. 185: pp. 1324-1335.

159. Panesar, A.S., *An Innovative Organic Rankine Cycle System for Integrated Cooling and Heat Recovery.* Applied Energy, 2017. 186: pp. 396-407.

160. Wang, E., Z. Yu, H. Zhang, and F. Yang, *A Regenerative Supercritical-Subcritical Dual-Loop Organic Rankine Cycle System for Energy Recovery from the Waste Heat of Internal Combustion Engines.* Applied Energy, 2017. 190: pp. 574-590.

161. Uusitalo, A., J. Honkatukia, and T. Turunen-Saaresti, *Evaluation of a Small-Scale Waste Heat Recovery Organic Rankine Cycle.* Applied Energy, 2017. 192: pp. 146-158.

162. Xu, B., A. Yebi, S. Onori, Z. Filipi, X. Liu, J. Shutty, P. Anschel, and M. Hoffman, *Transient Power Optimization of an Organic Rankine Cycle Waste Heat Recovery System for Heavy-Duty Diesel Engine Applications.* SAE International Journal of Alternative Powertrains, 2017. 6(2017-01-0133): pp. 25-33.

163. Liu, P., G.-Q. Shu, H. Tian, X. Wang, and D. Jing, *Fluid Selection and Thermodynamic Analysis of an Electricity-Cooling Cogeneration System Based on Waste Heat Recovery from Marine Engine.* SAE Technical Paper, 2017. 2017-01-0159.

164. Merrett, R., J. Murray, and D. Kolak, *Validation of an Organic Rankine Cycle Simulation Tool against European Stationary Cycle Test Modes.* SAE Technical Paper, 2017. 2017-01-0521.

165. Teng, H., J. Klaver, T. Park, G.L. Hunter, and B. van der Velde, *A Rankine Cycle System for Recovering Waste Heat from HD Diesel Engines-WHR System Development.* SAE Technical Paper, 2011. 2011-01-0311.

166. Park, T., H. Teng, G.L. Hunter, B. van der Velde, and J. Klaver, *A Rankine Cycle System for Recovering Waste Heat from HD Diesel Engines-Experimental Results.* SAE Technical Paper, 2011. 2011-01-1337.

167. Yu, X., S. Li, Z. Ma, W. Du, F. Huang, W. Huang, and B. Jiang, *Performance Characteristics Analysis of Variable Expansion Ratio Expander Based on Organic Rankine Cycle for Automobile Waste Heat Recovery.* SAE Technical Paper, 2017. 2017-01-2183.

168. Di Battista, D. and R. Cipollone, *Experimental Analysis of an Organic Rankine Cycle Plant Bottoming a Heavy-Duty Engine Using Axial Turbine as Prime Mover.* SAE International Journal of Engines, 2017. 10(2017-01-9279): pp. 1385-1397.

169. Di Battista, D., M. Di Bartolomeo, C. Villante, and R. Cipollone, *A Model Approach to the Sizing of an ORC Unit for WHR in Transportation Sector.* SAE International Journal of Commercial Vehicles, 2017. 10(2017-24-0159): pp. 608-617.

170. Di Battista, D., R. Cipollone, C. Villante, C. Fornari, and M. Mauriello, *The Potential of Mixtures of Pure Fluids in ORC-Based Power Units Fed by Exhaust Gases in Internal Combustion Engines.* Energy Procedia, 2016. 101: pp. 1264-1271.

171. Cignitti, S., J.G. Andreasen, F. Haglind, J.M. Woodley, and J. Abildskov, *Integrated Working Fluid-Thermodynamic Cycle Design of Organic Rankine Cycle Power Systems for Waste Heat Recovery.* Applied Energy, 2017. 203: pp. 442-453.

172. Xu, B., D. Rathod, S. Kulkarni, A. Yebi, Z. Filipi, S. Onori, and M. Hoffman, *Transient Dynamic Modeling and Validation of an Organic Rankine Cycle Waste Heat Recovery System for Heavy Duty Diesel Engine Applications.* Applied Energy, 2017. 205: pp. 260-279.

173. Preißinger, M., J.A. Schwöbel, A. Klamt, and D. Brüggemann, *Multi-Criteria Evaluation of Several Million Working Fluids for Waste Heat Recovery by Means of Organic Rankine Cycle in Passenger Cars and Heavy-Duty Trucks.* Applied Energy, 2017. 206: pp. 887-899.

174. Hou, X., H. Zhang, F. Yu, H. Liu, F. Yang, Y. Xu, Y. Tian, and G. Li, *Free Piston Expander-Linear Generator Used for Organic Rankine Cycle Waste Heat Recovery System.* Applied Energy, 2017. 208: pp. 1297-1307.

175. Zhou, F., S.N. Joshi, R. Rhote-Vaney, and E.M. Dede, *A Review and Future Application of Rankine Cycle to Passenger Vehicles for Waste Heat Recovery.* Renewable and Sustainable Energy Reviews, 2017. 75: pp. 1008-1021.

176. Lion, S., C.N. Michos, I. Vlaskos, C. Rouaud, and R. Taccani, *A Review of Waste Heat Recovery and Organic Rankine Cycles (ORC) in on-Off Highway Vehicle Heavy Duty Diesel Engine Applications.* Renewable and Sustainable Energy Reviews, 2017. 79: pp. 691-708.

177. Saloux, E., M. Sorin, H. Nesreddine, and A. Teyssedou, *Reconstruction Procedure of the Thermodynamic Cycle of Organic Rankine Cycles (ORC) and Selection of the Most Appropriate Working Fluid.* Applied Thermal Engineering, 2018. 129: pp. 628-635.

178. Yang, Y., H. Zhang, Y. Xu, R. Zhao, X. Hou, and Y. Liu, *Experimental Study and Performance Analysis of a Hydraulic Diaphragm Metering Pump Used in Organic Rankine Cycle System.* Applied Thermal Engineering, 2018. 132: pp. 605-612.

179. Sarkar, J., *Generalized Pinch Point Design Method of Subcritical-Supercritical Organic Rankine Cycle for Maximum Heat Recovery.* Energy, 2018. 143: pp. 141-150.

180. Negash, A., Y.M. Kim, D.G. Shin, and G.B. Cho, *Optimization of Organic Rankine Cycle Used for Waste Heat Recovery of Construction Equipment Engine with Additional Waste Heat of Hydraulic Oil Cooler.* Energy, 2018. 143: pp. 797-811.

181. Zhao, R., H. Zhang, S. Song, Y. Tian, Y. Yang, and Y. Liu, *Integrated Simulation and Control Strategy of the Diesel Engine–Organic Rankine Cycle (ORC) Combined System.* Energy Conversion and Management, 2018. 156: pp. 639-654.

182. Garcia, S.I., R.F. Garcia, J.C. Carril, and D.I. Garcia, *A Review of Thermodynamic Cycles Used in Low Temperature Recovery Systems over the Last Two Years.* Renewable and Sustainable Energy Reviews, 2018. 81: pp. 760-767.

183. Langness, C., M. Mangus, and C. Depcik, *Construction, Instrumentation, and Implementation of a Low Cost, Single-Cylinder Compression Ignition Engine Test Cell.* SAE Technical Paper, 2014. 2014-01-0817.

184. Sprouse III, C. and C. Depcik, *Combining a Diesel Particulate Filter and Heat Exchanger for Waste Heat Recovery and Particulate Matter Reduction.* SAE Technical Paper, 2014. 2014-01-0673.

185. Kroenlein, K., C. Muzny, A. Kazakov, V. Diky, R. Chirico, J. Magee, I. Abdulagatov, and M. Frenkel, *NIST/TRC Web Thermo Tables (WTT), Nist Standard Reference Subscription Database 3—Professional Edition, Version 2-2012-1-Pro.* 2011.

186. Villamanan, M.A., C. Gonzalez, and H.C. Van Ness, *Excess Thermodynamic Properties for Water/Ethylene Glycol.* Journal of Chemical and Engineering Data, 1984. 29(4): pp. 427-429.

187. Company, T.D.C., *Specific Heats of Aqueous Glycol Solutions*. 2017: https://dowac.custhelp.com/app/answers/detail/a_id/7470.

188. Dynalene, I., *Dynalene Ethylene Glycol Series*, in *Dynalene EG Technical Data Sheet*. 2018, http://www.dynalene.com/wp-content/uploads/2018/09/Dynalene_EG_Technical_Data_Sheet.pdf.

189. Dynalene, I., *Dynalene EG (Heat Transfer Fluid)*, in *Dynalene EG SDS*. 2014, https://www.dynalene.com/wp-content/uploads/2018/07/Dynalene_EG_MSDS.pdf.

190. Dynalene, I., *Dynalene PG (Heat Transfer Fluid)*, in *Dynalene PG SDS*. 2014, https://www.dynalene.com/wp-content/uploads/2018/07/Dynalene_PG_MSDS.pdf.

191. Dynalene, I., *Dynalene Propylene Glycol Series*, in *Dynalene PG Tecnical Data Sheet*. 2018, https://www.dynalene.com/wp-content/uploads/2018/09/Dynalene_PG_Technical_Data_sheet.pdf.

192. Figliola, R.S. and D. Beasley, *Theory and Design for Mechanical Measurements*. 2011: John Wiley & Sons.

193. Depcik, C. and D.N. Assanis, *A Universal Heat Transfer Correlation for Intake and Exhaust Flows in an Spark-Ignition Internal Combustion Engine.* SAE Technical Paper, 2002. 2002-01-0372.

194. Kakaç, S., R.K. Shah, and W. Aung, *Handbook of Single-Phase Convective Heat Transfer.* 1987.

195. Wang, Y., X. Gu, Z. Jin, and K. Wang, *Characteristics of Heat Transfer for Tube Banks in Crossflow and Its Relation with That in Shell-and-Tube Heat Exchangers.* International Journal of Heat and Mass Transfer, 2016. 93: pp. 584-594.

196. Kim, W.-K. and T. Aicher, *Experimental Investigation of Heat Transfer in Shell-and-Tube Heat Exchangers without Baffles.* Korean Journal of Chemical Engineering, 1997. 14(2): pp. 93-100.

197. Kern, D.Q., *Process Heat Transfer*. 1950: Tata McGraw-Hill Education.

198. Kays, W.M., M.E. Crawford, and B. Weigand, *Convective Heat and Mass Transfer*. 2005.

199. Miller, P., J.J. Byrnes, and D.M. Benforado, *Heat Transfer to Water Flowing Parallel to a Rod Bundle.* AIChE Journal, 1956. 2(2): pp. 226-234.

200. Rieger, M., *Experimental Study of Heat Transfer for Parallel Flow in Tube Bundles with Constant Heat Flux and for Medium Prandtl Numbers.* 1969.

201. Dingee, D.A., W. Bell, J. Chastain, and S. Fawcett, *Heat Transfer from Parallel Rods in Axial Flow*. 1955, Battelle Memorial Inst.: Columbus, Ohio.

202. Toledo-Velázquez, M., P. Quinto-Diez, J.C. Alzelmetti-Zaragoza, S.R. Galvan, J. Abugaber-Francis, and A. Reyes-León, *Delaware Method Improvement for the Shell and Tubes Heat Exchanger Design.* Engineering, 2014. 6(04): pp. 193.

203. *Christopher Depcik - Google Scholar Citations*. Google Scholar 2019 [cited 2019 1/25/2019].

204. Depcik, C. and D. Assanis, *Simulating Area Conservation and the Gas-Wall Interface for One-Dimensional Based Diesel Particulate Filter Models.* Journal of Engineering for Gas Turbines and Power, 2008. 130(6): pp. 062807.

Appendices

Appendix A: Transient Conduction Calculations

To evaluate the time for the apparatus to achieve steady state conduction (i.e., determining an allowable time for the apparatus to run prior to collecting experimental data), transient conduction calculations were carried out, assessing conduction on the tube side (i.e., exhaust). First, the Biot (*Bi*) number was calculated for via Eq. (A.1), where h is the convection heat transfer coefficient, L_c is the characteristic length, and k is the thermal conductivity [29]; however, since the convection heat transfer coefficient of the flow was unknown initially, the Biot number was calculated with the maximum and minimum values for gases in forced convection, yielding values of 0.0506 for the maximum convection heat transfer coefficient (h = 250 W/m^{2}K) and 0.00506 for the minimum value (h = 25 W/m^{2}K) [29].

$$Bi = \frac{hL_c}{k} \tag{A.1}$$

Since the Biot number is greater than 0.1, the lumped capacitance method is valid, allowing for the use of Eq. (A.2) to calculate the time required for the HEX tube to reach approximately 99% of the exhaust temperature (i.e., 0.99*375 K ≈ 371.25 K) [29]. In Eq. (A.2), ρ is the density of stainless steel (8238 kg/m^3), c is the specific heat of stainless steel (468 J/kgK), and V and A_s represent the volume and inner surface area of the tubes [29].

$$t = \frac{\rho V c}{h A_s} \ln\left(\frac{T_i - T_{ex}}{T - T_{ex}}\right) \tag{A.2}$$

The calculated time for the tube to reach approximately ambient temperature of the exhaust gas for the minimum convection coefficient was 1596.17 s (approximately 26 minutes) and 159.62 s (approximately 2.66 minutes) for the maximum convection coefficient. Although this rudimentary calculation does not take into account the circulation of the working fluid on the outside of the tubes, it provides a decent estimate of the time required for the solid components of the apparatus to achieve steady state conditions. Thus, prior to capturing experimental data, the engine and apparatus were run for approximately 30 minutes each, allowing plenty of time for this conduction to take place.

The calculations were also considered for the working fluid, via the lumped capacitance method for the minimum convection coefficient for fluids in forced convection and the approximate solution method for the maximum based on their respective Biot numbers. However, the values were significantly lower than that of the exhaust side. Therefore, the exhaust values provide the maximum approximation of the time to reach steady state.

Appendix B: Code for Experimental Calculations

```
% % Bailey Spickler
% % Experimental Calculations
% % Includes pulling in data from Excel spreadsheet of all experimental
% data to calculate all trials in one run & write the results to the same
% Excel sheet

clc
clear

input = xlsread('Test Results File');
inputsize = size(input);
output = zeros(inputsize(1),5);

for j = 1:inputsize(1)
% Experimental Inputs
wf = input(j,1); % Denote as 1 water, 2 as EG, 3 as PG, or 4 as W-EG

% Working fluid temperatures [K] & pressures [psi]
Twfin = input(j,3); % [K]
Twfout = input(j,4); % [K]
pwfin = input(j,5); % [psi]
pwfout = input(j,6); % [psi]

% Exhaust temperatures [K] & pressures [psi]
Texin = input(j,7);  % [K]
Texout = input(j,8); % [K]
pexin = input(j,9); % [psi]
pexout = input(j,10); % [psi]

mwf = input(j,11); % working fluid flow rate [kg/s]
mfuel = input(j,12); % Fuel flow rate [g/s]
mair = input(j,13); % Air flow rate [g/s]

%% Exhaust Calcs

R = 8.314; % [kJ/kmol]

Cx = 14.2; % Fuel composition
Hy = 25.54;

C = 12; % Molar weights
H = 1;
O = 16;
N = 14;

MCO2 = C + O*2;
MH2O = 2*H + O;
MN2 = 2*N;
MO2 = 2*O;
```

```
% Flow rates & molar weights
Mfuel = Cx*C + Hy*H; % Fuel molar weight [g/mol]
Mair = 2*O + 3.76*2*N; % Air molar weight [g/mol]

nfuel = mfuel/Mfuel; % Fuel molar flow rate [mol/s]
nair = mair/Mair; % Air molar flow rate [mol/s]

Z = (mair/mfuel)*(Mfuel/Mair); % Number of air molecules needed

% Balance lean combustion equation
% CxHy + Z(O2 + 3.76N2) -> b*CO2 + d*H2O + e*N2 + f*O2

cCO2 = Cx;
cH2O = Hy/2;
cN2 = Z*3.76;
cO2 = 0.5*(2*Z - cH2O - 2*cCO2);

% Finding molar flow rates [mol/s]
% Based on conservation mass flow in = mass flow out
% Reactants
nRO2 = Z*nfuel;
nRN2 = 3.76*Z*nfuel;
% Products
nPCO2 = cCO2*nfuel;
nPH2O = cH2O*nfuel;
nPN2 = cN2*nfuel;
nPO2 = cO2*nfuel;

% Finding enthalpies
% Interpolating using values from Moran & Shapiro 5th Edition, Table A-23
% h = hof + dh(from 298K)
Temps_species = [0; 220; 230; 240; 250; 260; 270; 280; 290; 298; 300; 310;
320; 330; 340; 350; 360; 370; 380; 390; 400; 410; 420; 430; 440; 450; 460;
470; 480; 490; 500]; % [K]
h_CO2_table = [0; 6601; 6938; 7280; 7627; 7979; 8335; 8697; 9063; 9364; 9431;
9807; 10186; 10570; 10959; 11351; 11748; 12148; 12552; 12960; 13372; 13787;
14206; 14628; 15054; 15483; 15916; 16351; 16791; 17232; 17678]; % [kJ/kmol]
h_H2O_table = [0; 7295; 7628; 7961; 8294; 8627; 8961; 9296; 9631; 9904; 9966;
10302; 10639; 10976; 11314; 11652; 11992; 12331; 12672; 13014; 13356; 13699;
14043; 14388; 14734; 15080; 15428; 15777; 16126; 16477; 16828]; % [kJ/kmol]
h_O2_table = [0; 6404; 6694; 6984; 7275; 7566; 7858; 8150; 8443; 8682; 8736;
9030; 9325; 9620; 9916; 10213; 10511; 10809; 11109; 11409; 11711; 12012;
12314; 12618; 12923; 13228; 13535; 13842; 14151; 14460; 14770]; % [kJ/kmol]
h_N2_table = [0; 6391; 6683; 6975; 7266; 7558; 7849; 8141; 8432; 8669; 8723;
9014; 9306; 9597; 9888; 10180; 10471; 10763; 11055; 11347; 11640; 11932;
12225; 12518; 12811; 13105; 13399; 13693; 13988; 14285; 14581]; % [kJ/kmol]

% CO2
hofCO2 = -393522; % [kJ/kmol]
h298CO2 = 9364; % [kJ/kmol]
hTinCO2 = interp1(Temps_species, h_CO2_table, Texin); % [kJ/kmol]
hToutCO2 = interp1(Temps_species, h_CO2_table, Texout); % [kJ/kmol]
```

```
hinCO2 = hofCO2 + hTinCO2 - h298CO2;  % [kJ/kmol]
houtCO2 = hofCO2 + hToutCO2 - h298CO2;  % [kJ/kmol]

% H2O
hofH2O = -241820; % [kJ/kmol]
h298H2O = 9904; % [kJ/kmol]
hTinH2O = interp1(Temps_species, h_H2O_table, Texin); % [kJ/kmol]
hToutH2O = interp1(Temps_species, h_H2O_table, Texout); % [kJ/kmol]

hinH2O = hofH2O + hTinH2O - h298H2O; % [kJ/kmol]
houtH2O = hofH2O + hToutH2O - h298H2O; % [kJ/kmol]

% O2
hofO2 = 0; % [kJ/kmol]
h298O2 = 8682; % [kJ/kmol]
hTinO2 = interp1(Temps_species, h_O2_table, Texin); % [kJ/kmol]
hToutO2 = interp1(Temps_species, h_O2_table, Texout); % [kJ/kmol]

hinO2 = hofO2 + hTinO2 - h298O2; % [kJ/kmol]
houtO2 = hofO2 + hToutO2 - h298O2; % [kJ/kmol]

% N2
hofN2 = 0; % [kJ/kmol]
h298N2 = 8669; % [kJ/kmol]
hTinN2 = interp1(Temps_species, h_N2_table, Texin); % [kJ/kmol]
hToutN2 = interp1(Temps_species, h_N2_table, Texout); % [kJ/kmol]

hinN2 = hofN2 + hTinN2 - h298N2; % [kJ/kmol]
houtN2 = hofN2 + hToutN2 - h298N2; % [kJ/kmol]


% Heat Transfer Qexhaust
QCO2 = nPCO2*(houtCO2 - hinCO2); % [W]
QH2O = nPH2O*(houtH2O - hinH2O); % [W]
QN2 = nPN2*(houtN2 - hinN2); % [W]
QO2 = nPO2*(houtO2 - hinO2); % [W]
Qex = QCO2 + QH2O + QN2 + QO2; % [W]


if wf == 1
    %% Working Fluid Calcs (water)
    % Calculate enthalpies
    % Interpolation of saturated water (liquid) table based on temperature
    % Values from Moran & Shapiro, 5th Edition, Table A-2

    Wtempinterp =
[10;11;12;13;14;15;16;17;18;19;20;21;22;23;24;25;26;27;28;29;30;31;32;33;34;3
5;36;38;40;45]+273.15; % [K]
    Whinterp = [42.01; 46.20; 50.41; 54.60; 58.80; 62.99; 67.19; 71.38;
75.58; 79.77; 83.96; 88.14; 92.33; 96.52; 100.70; 104.89; 109.07; 113.25;
117.43; 121.61; 125.79; 129.97; 134.15; 138.33; 142.50; 146.68; 150.86;
159.21; 167.57; 188.45]; % [kJ/kg]
```

```
    % Twfin
    hwfin = interp1(Wtempinterp, Whinterp, Twfin);

    % Twfout
    hwfout = interp1(Wtempinterp, Whinterp, Twfout);

    % Qwf
    Qwf = mwf*(hwfout - hwfin)*1000; % [W]


    % Calculating cpwf for effectiveness calculations (later)
    % values from Moran & Shapiro 5th Edition, Table A-19
    water_temp = [275; 300; 325; 350; 375; 400]; % [K]
    water_cp = [4.211; 4.179; 4.182; 4.195; 4.220; 4.256]; % [kJ/kgK]

    cpwfin = interp1(water_temp, water_cp, Twfin); % [kJ/kgK]
    cpwfout = interp1(water_temp, water_cp, Twfout); % [kJ/kgK]

elseif wf == 2
    %% Working Fluid Calcs (Pure EG)
    % Pull in Excel enthalpy data

    m = xlsread('EG Enthalpy Data.csv');
    % From: NIST Chemistry WebBook
    % https://wtt-pro.nist.gov/wtt-pro/index.html?cmp=1.2-ethanediol#1.2-
ethanediol;06;0Z;4g;1g;7g;3g;5g;Hg;8g;8f;8a;8b;O6;Qg;T2;Re;zg,259.26,472.96,1
;Ye;ag;ae;ef;hf;jg;ja;na;ng;ya;yf/c;0,0/a;50,50/zgR;100,100/zgT;150,150,508,3
82/

    TempEG = m(:,1); % [K]
    EnthalpyEG = m(:,2); % [kJ/mol]
    UncertaintyEG = m(:,3); % [kJ/mol]

    MWEG = 62/1000; % Molar weight of EG, [kg/mol]


    % Interpolate data to find enthalpy values at inlet & exit temperatures
of
    % the wf
    hwfin = interp1(TempEG,EnthalpyEG,Twfin); % [kJ/mol]
    hwfout = interp1(TempEG,EnthalpyEG,Twfout); % [kJ/mol]

    hwfin = hwfin/MWEG; % [kJ/kg]
    hwfout = hwfout/MWEG; % [kJ/kg]

    Qwf = mwf*(hwfout - hwfin)*1000; % [W]

    % Calculating cpwf for effectiveness (later)
    % Data from Bergman 6th Ed.
    EG_temp = [273 280 290 300 310 320 330 340 350 360 370 373]; % [K]
    EG_spheat = [2.294 2.323 2.368 2.415 2.460 2.505 2.549 2.592 2.637 2.682
2.728 2.742]; % [kJ/kgK]
```

```
    cpwfin = interp1(EG_temp, EG_spheat, Twfin); % [kJ/kgK]
    cpwfout = interp1(EG_temp, EG_spheat, Twfout); % [kJ/kgK]

elseif wf == 3
    %% Working Fluid Calcs (Pure PG)

    PGrho = 1.032*1000; % [kg/m^3]
    PGv = 1/PGrho; % [m^3/kg]

    % Temperatures & Specific Heats for 100% PG
    % From NIST WebBook
    % https://wtt-pro.nist.gov/wtt-pro/index.html?cmp=1.2-propanediol#1.2-
propanediol;06;4g;1g;7g;3g;5g;Hg;8g,263,676.4,1;8f;8b;Qg;Tg,300,600,20;Re;Ye,
200,450,1;ae;ag;ef;hf;mg;jg,273.001,670,1;ja;na;ng,250,600,1;ya;yf/c;0,0/a;50
,50/
    n = xlsread('PG Enthalpy Data.csv');

    TempPG = n(:,1); % [K]
    EnthalpyPG = n(:,2); % [kJ/mol]
    UncertaintyPG = n(:,3); % [kJ/mol]

    MWPG = 76/1000; % Molar weight of PG, [kg/mol]


    % Interpolate data to find enthalpy values at inlet & exit temperatures
of
    % the wf
    hwfin = interp1(TempPG,EnthalpyPG,Twfin); % [kJ/mol]
    hwfout = interp1(TempPG,EnthalpyPG,Twfout); % [kJ/mol]

    hwfin = hwfin/MWPG; % [kJ/kg]
    hwfout = hwfout/MWPG; % [kJ/kg]

    Qwf = mwf*(hwfout - hwfin)*1000; % [W]


    % Calculate specific heat for effectiveness calculations (later)
    % Temperatures & Specific Heats for 100% PG

    PG_temp = [15.6; 26.7; 37.8; 48.9; 60.0; 71.1; 82.2; 93.3; 104.4;
115.5]+273.15; % [oC] --> [K]
    PG_spheat = [ 0.587; 0.603; 0.619; 0.635; 0.651; 0.667; 0.683; 0.699;
0.715; 0.731]*4.1868; % [cal/g/oC]

    cpwfin = interp1(PG_temp, PG_spheat, Twfin); % [kJ/kgK]
    cpwfout = interp1(PG_temp, PG_spheat, Twfout); % [kJ/kgK]

elseif wf == 4

    m = xlsread('EG Enthalpy Data.csv');
```

```
    TempEG = m(:,1); % [K]
    EnthalpyEG = m(:,2); % [kJ/mol]
    UncertaintyEG = m(:,3); % [kJ/mol]

    MWEG = 62/1000; % Molar weight of EG, [kg/mol]


    % Interpolate data to find enthalpy values at inlet & exit temperatures
of
    % the wf
    EGhwfin = interp1(TempEG,EnthalpyEG,Twfin); % [kJ/mol]
    EGhwfout = interp1(TempEG,EnthalpyEG,Twfout); % [kJ/mol]

    EGhwfin = EGhwfin/MWEG; % [kJ/kg]
    EGhwfout = EGhwfout/MWEG; % [kJ/kg]

    % Interpolation of saturated water (liquid) table based on temperature
    % Values from Moran & Shapiro, 5th Edition

    MWW = MH2O/1000; % molar weight of H2O, [kg/mol]

    Wtempinterp =
[10;11;12;13;14;15;16;17;18;19;20;21;22;23;24;25;26;27;28;29;30;31;32;33;34;3
5;36;38;40;45]+273.15; % [oC] --> [K]
    Whinterp = [42.01; 46.20; 50.41; 54.60; 58.80; 62.99; 67.19; 71.38;
75.58; 79.77; 83.96; 88.14; 92.33; 96.52; 100.70; 104.89; 109.07; 113.25;
117.43; 121.61; 125.79; 129.97; 134.15; 138.33; 142.50; 146.68; 150.86;
159.21; 167.57; 188.45]; % [kJ/kg]

    % Twfin
    Whwfin = interp1(Wtempinterp, Whinterp, Twfin); % [kJ/kg]

    % Twfout
    Whwfout = interp1(Wtempinterp, Whinterp, Twfout); % [kJ/kg]

    Y_EG_mix = (0.5*MWEG)/(0.5*MWW + 0.5*MWEG); % [-]
    Y_W_mix = (0.5*MWW)/(0.5*MWW + 0.5*MWEG); % [-]

    hwfin = Y_EG_mix*EGhwfin + Y_W_mix*Whwfin; % [kJ/kg]
    hwfout = Y_EG_mix*EGhwfout + Y_W_mix*Whwfout; % [kJ/kg]

    Qwf = mwf*(hwfout - hwfin)*1000; % [W]

    % specific heat calculation for effectivness (later)
    % Data from Dynalene for 50% EG & Water

    HEG_temp = (([0 10 20 30 40 50 60 70 80 90 100 120 140]-
32)*(5/9))+273.15; % [oF] --> [oC] --> [K]
    HEG_spheat = [0.740 0.745 0.751 0.756 0.761 0.766 0.772 0.777 0.782 0.781
0.793 0.803 0.814]*4186/1000; % [Btu/lboF] --> [J/kgoC] = [J/kgK] -->
[kJ/kgK]
```

```
    cpwfin = interp1(HEG_temp, HEG_spheat, Twfin); % [kJ/kgK]
    cpwfout = interp1(HEG_temp, HEG_spheat, Twfout); % [kJ/kgK]

end

%% Cp Calculations
% Total number of moles
np = cCO2 + cH2O + cN2 + cO2;

% Coefficients by species for Cp calcs
% CO2
aCO2 = 2.401;
bCO2 = 8.735e-3;
yCO2 = -6.607e-6;
dCO2 = 2.002e-9;
eCO2 = 0;

% H20
aH2O = 4.07;
bH2O = -1.108e-3;
yH2O = 4.152e-6;
dH2O = -2.964e-9;
eH2O = 0.807e-12;

% N2
aN2 = 3.675;
bN2 = -1.208e-3;
yN2 = 2.324e-6;
dN2 = -0.632e-9;
eN2 = -0.226e-12;

% O2
aO2 = 3.626;
bO2 = -1.878e-3;
yO2 = 7.055e-6;
dO2 = -6.764e-9;
eO2 = 2.156e-12;


% Calculate Cp,in & Cp,ex for each species
% CO2
CpCO2in = R*(aCO2 + bCO2*Texin + yCO2*(Texin^2) + dCO2*(Texin^3) +
eCO2*(Texin^4)); % [kJ/kmolK]
CpCO2in = CpCO2in/MCO2; %[kJ/kgK]
CpCO2out = R*(aCO2 + bCO2*Texout + yCO2*(Texout^2) + dCO2*(Texout^3) +
eCO2*(Texout^4));
CpCO2out = CpCO2out/MCO2;
% H20
CpH2Oin = R*(aH2O + bH2O*Texin + yH2O*(Texin^2) + dH2O*(Texin^3) +
eH2O*(Texin^4));
CpH2Oin = CpH2Oin/MH2O;
CpH2Oout = R*(aH2O + bH2O*Texout + yH2O*(Texout^2) + dH2O*(Texout^3) +
eH2O*(Texout^4));
CpH2Oout = CpH2Oout/MH2O;
```

```
% N2
CpN2in = R*(aN2 + bN2*Texin + yN2*(Texin^2) + dN2*(Texin^3) + eN2*(Texin^4));
CpN2in = CpN2in/MN2;
CpN2out = R*(aN2 + bN2*Texout + yN2*(Texout^2) + dN2*(Texout^3) +
eN2*(Texout^4));
CpN2out = CpN2out/MN2;
% O2
CpO2in = R*(aO2 + bO2*Texin + yO2*(Texin^2) + dO2*(Texin^3) + eO2*(Texin^4));
CpO2in = CpO2in/MO2;
CpO2out = R*(aO2 + bO2*Texout + yO2*(Texout^2) + dO2*(Texout^3) +
eO2*(Texout^4));
CpO2out = CpO2out/MO2;


% Mole & mass fractions for each species
XCO2 = cCO2/np;
XH2O = cH2O/np;
XN2 = cN2/np;
XO2 = cO2/np;

M_mix = XCO2*MCO2 + XH2O*MH2O + XN2*MN2 + XO2*MO2;

YCO2 = (XCO2*MCO2)/M_mix;
YH2O = (XH2O*MH2O)/M_mix;
YN2 = (XN2*MN2)/M_mix;
YO2 = (XO2*MO2)/M_mix;
% YN2 = 1 - YCO2 - YH2O - YO2;

% Adding individual species for overall exhaust Cp
Cpexin = YCO2*CpCO2in + YH2O*CpH2Oin + YN2*CpN2in + YO2*CpO2in;
Cpexout = YCO2*CpCO2out + YH2O*CpH2Oout + YN2*CpN2out + YO2*CpO2out;
Cpexavg = (Cpexin + Cpexout)/2;

%%

% Calculating working fluid Cp
% cpwfin & cpwfout calculated for each working fluid separately

Cpwfavg = (cpwfin + cpwfout)/2;
%% Calculating Effectiveness & Overall Heat Transfer Coefficient
Awf = 0.1915; % [m^2]
Thin = Texin; % [K]
Thout = Texout; % [K]
Tcin = Twfin; % [K]
Tcout = Twfout; % [K]

mh = (mfuel + mair)/1000; % [kg/s]
Cph = Cpexavg;
mhCph = mh*Cph;
mc = mwf;
Cpc = Cpwfavg;
mcCpc = mc*Cpc;
```

```
mCpmin = min(mhCph, mcCpc);
mCpmax = max(mhCph, mcCpc);

eff1 = ((mcCpc)*(Tcout - Tcin))/(mCpmin*(Thin - Tcin)); % Based on wf heat
transfer
eff2 = ((mhCph)*(Thin - Thout))/(mCpmin*(Thin - Tcin)); % Based on exhaust
heat transfer

% Parallel Flow
dT1 = Thin - Tcin;
dT2 = Thout - Tcout;
LMTD = (dT1-dT2)/log(dT1/dT2);

U = (Cpc*mc*1000*(Tcout-Tcin))/(Awf*LMTD); % Overall Heat Transfer
Coefficient

NTU = U*Awf/(mCpmin*1000);
Cr = mCpmin/mCpmax;

% Parallel concentric flow
exp_eff = (1-exp(-NTU*(1+Cr)))/(1+Cr);

%% Write results to single matrix

output(j,1) = Qex;
output(j,2) = Qwf;
output(j,3) = eff1;
output(j,4) = eff2;
output(j,5) = exp_eff;
output(j,6) = U;
output(j,7) = LMTD;
output(j,8) = Cpc;
output(j,9) = Cph;
output(j,10) = mCpmin;

end

xlswrite('Test Results Output File', output, 'O2:S16');
```

Appendix C: Working Fluid Heat Transfer Coefficients Calculated via the Thermal Resistance Network and Literature Exhaust Gas Correlation

Table C.1: Working fluid heat transfer coefficients [W/m^{2}K] calculated from the thermal resistance network using the following literature exhaust gas correlations: (1) Dittus-Boelter; (2) Colburn; (3) Gnielinkski; (4) Gnielinkski Simplification; (5) Sachdev with Meisner; (6) Malchow; (7) Shayler; (8) Depcik Exhaust; (9) Depcik Universal; (10) Kakaç.

Working Fluid	Trial	h_1	h_2	h_3	h_4	h_5	h_6	h_7	h_8	h_9	h_{10}
Water	1	-27.82	-28.85	-30.09	-43.86	1297.05	-141.51	-540.42	-252.80	-219.94	-41.98
Water	2	-28.47	-29.55	-30.84	-45.50	629.57	-160.01	-965.05	-318.51	-268.05	-43.47
Water	1	-30.43	-31.67	-33.14	-50.67	266.20	-246.35	881.64	-1041.80	-645.43	-48.15
Water	2	-33.48	-34.99	-36.83	-59.79	146.12	-1008.06	236.77	472.10	654.70	-56.36
Water	3	-33.81	-35.35	-37.26	-60.91	138.58	-1571.45	217.46	402.70	528.72	-57.38
Water	3	-32.97	-34.44	-36.35	-58.23	150.42	-805.63	246.57	524.82	762.50	-55.16
EG	1	-32.39	-33.80	-35.56	-56.45	167.60	-527.48	298.07	812.48	1566.58	-53.44
EG	2	-32.10	-33.49	-35.23	-55.52	176.05	-458.88	324.85	1053.60	2800.71	-52.65
EG	3	-31.95	-33.33	-35.07	-55.09	179.65	-435.08	336.92	1199.32	4141.64	-52.28
PG	1	-42.64	-45.13	-48.39	-97.07	74.44	179.74	92.31	114.97	123.38	-88.68
PG	2	-42.47	-44.94	-48.22	-96.01	74.94	182.65	92.96	116.10	124.68	-87.94
PG	3	-42.20	-44.64	-47.91	-94.56	75.77	187.65	94.18	118.07	126.95	-86.80
50/50	1	-28.13	-29.19	-30.49	-44.64	804.81	-151.32	-731.13	-286.77	-245.17	-42.74
50/50	2	-36.20	-37.98	-40.26	-69.01	108.53	738.29	151.10	222.98	256.88	-64.66
50/50	3	-41.72	-44.10	-47.25	-92.30	77.39	197.97	96.80	122.12	131.64	-84.78

Appendix D: MATLAB Codes for the Optimization of the Exhaust and Working Fluid Nusselt Number Coefficients

D.1 Optimization Start Code

```
%*********************************************************************%
%  This is the main optimization file to be run                       %
%*********************************************************************%
% Clear the workspace
clear all;
%**************************************************************************
%  Set nominal value for variables and ranges
%**************************************************************************

% % Std. Form & Staggered Tube coefficients
Fit0(1) = ; % a from Nuex --> 0.101747 is initial value used for first run
Fit0(2) = ; % d from Nuwf --> use correlation values for d,e,f for first run
Fit0(3) = ; % e from Nuwf
Fit0(4) = ; % f from Nuwf


% % % % % For Bell-Delaware correlation --->
% % % % Fit0(1) = ; % a from Nuex --> 0.101747 is initial value used for
first run
% % % % Fit0(2:53) = []; --> use correlation values for first run

for ll = 1:4

% Set the lower bounds
% % For std form & staggered tube correlations
FitLB = [0.001  0.001 0.001 0.001];

% % % % % For Bell-Delaware
% % % % FitLB(1) = 0.101751;
% % % % FitLB(2:53) = -10^-15;

% Set the upper bounds
% %  For std form and staggered tube correlations
FitUB = [0.1019 1000.0 1000.0 1000.0];

% % % % for Bell-Delaware -->
% % % FitUB(1:53) = 10000.0;

%**************************************************************************
% Create the optimization options parameter structure
% Try and guess decent values initially, but usually they need to be adjusted
options = optimset('Display','iter',...
                   'TolX',1e-5,...                      % Termination
tolerance on x
```

```
                    'TolFun',1e-5,...                       % Termination
tolerance on function value
                    'MaxIter',1e6,...                       % Maximum number of
iterations allowed
                    'MaxFunEvals',1e6,...                   % Maximum function
evaluations
                    'DiffMinChange',.0001,...               % Minimum change in
variables for finite difference derivatives
                    'DiffMaxChange',.001, ...               % Maximum change in
variables for finite difference derivatives
                    'Algorithm','interior-point');
%************************************************************************
A = []; b = []; Aeq = []; beq = [];
% Call the optimization routine
x = fmincon(@Numodel_thesis, Fit0, A, b, Aeq, beq, FitLB, FitUB, [],
options);
% Put the variables back in the workspace
%************************************************************************
% Check the results file for the minimum myfun
Fit0 = x;
End
```

D.2 Calculating LSQ for the Optimization

```
function myfun2 = Numodel_thesis(VAR,~)
resultsfile = ('BaileyOpt_v#_date.csv');
% % %  For Std. Form & Staggered Tube Correlations
av = VAR(1); % a for Nuex
const(1) = VAR(2); % d for Nuwf
const(2) = VAR(3); % e for Nuwf
const(3) = VAR(4); % f for Nuwf

% % % % %%% For Bell-Delware correlation
% % % % av = VAR(1); % a for Nuex
% % % % const(1:5) = VAR(2:6);
% % % % const(6) = VAR(7)*10^-5;
% % % % const(7:35) = VAR(8:36);
% % % % const(36) = VAR(37)*10^-7;
% % % % const(37:39) = VAR(38:40);
% % % % const(40) = VAR(41)*10^-8;
% % % % const(41:42) = VAR(42:43);
% % % % const(43) = VAR(44)*10^-6;
% % % % const(44) = VAR(45)*10^-8;
% % % % const(45) = VAR(46);
% % % % const(46) = VAR(47)*10^-4;
% % % % const(47) = VAR(48)*10^-5;
% % % % const(48) = VAR(49)*10^-7;
% % % % const(49:51) = VAR(50:52);
% % % % const(52) = VAR(53)*10^-8;
```

```
% Call the model routine
% modeltype: 1 = std form; 2 = staggered tubes; 3 = Bell-Delaware
[ Nuwfexp, Nuwfmod ] = Nuwfopt_thesis(av, 1, const);
% Now, compute myfun
myfun2 = 0;
for i=1:length(Nuwfexp)
    myfun2 = real(myfun2 + (log(Nuwfexp(i)) - log(Nuwfmod(i)))^2);
end
myfun2 = sqrt(myfun2)
% Write the results file
fd=fopen(resultsfile,'a');
c = clock;
s = date;
fprintf(fd, 'The current date is: %s,', s);
fprintf(fd, 'The current time is: %.0f:%.0f.%.2f,', c(4), c(5), c(6));
fprintf(fd,'The parameters are:,');
% %  For std form & staggered tube correlations
fprintf(fd, '%.7e,%.7e,%.7e,', av, const(1), const(2), const(3));

% % % % % % Bell-Delaware -->
% % % % fprintf(fd, '%.7e,%.7e,%.7e,', av, const(1:5), const(6)*10^5,
const(7:35), const(36)*10^7, const(37:39), const(40)*10^8, const(41:42),
const(43)*10^6, const(44)*10^8, const(45), const(46)*10^4, const(47)*10^5,
const(48)*10^7, const(49:51), const(52)*10^8);

fprintf(fd, 'The least-squared factor is:,');
fprintf(fd, '%.7e\n', myfun2);
fclose(fd);
```

D.3 Calculating Nusselt Number Based on Optimization Coefficients

```
function [ Nuwfexp, Nuwfmod ] = Nuwfopt_thesis( a, modeltype, const)

% % Use calculated values for Re, Pr, k, and Rtotal to use for comparison
Reex = [];
Prex = [];
kex = []; % [W/mK]

Rewf = [];
Prwf = [];
kwf = []; % [W/mK]

Rtot = [];

R2 = 0.000526088953122251;

b = 3/4;
c = 1/3;
```

```
dti = 2*0.009525;
dto = 2*0.0111125;
Ltb = 0.4572;
Dis = 0.08265;

for i=1:length(Reex)

    Nuex(i) = a*(Reex(i)^b)*(Prex(i)^c);

    % Nuwf,exp
    hex(i) = (Nuex(i)*kex(i))/dti;
    R1(i) = 1/(6*pi*dto*Ltb*hex(i));
    R3(i) = Rtot(i) - R1(i) - R2;
    hwf(i) = 1/(6*R3(i)*pi*dto*Ltb);
    Nuwfexp(i) = hwf(i)*dto/kwf(i);

    % Nuwf,model
    %if modeltype == 'Zukauskas' "OR" 'Hausen' "OR" 'Short' "OR" 'Kim_min'
"OR" 'Kim_max' "OR" 'Dittus-Boelter' "OR" 'Kern' "OR" 'Kays'
    if modeltype == 1
        d = const(1);
        e = const(2);
        f = const(3);
        Nuwfmod(i) = d*(Rewf(i)^e)*(Prwf(i)^f);

    %elseif modeltype == 'StaggeredTubes'
    elseif modeltype == 2
        Sn = 0.028575;
        Sp = 0.034925;

        % % Insert values for u, mu, and rho based on experimental
        % conditions & working fluid
        uwf = [];
        muwf = [];
        rhowf = [];

        umax = (uwf(i)*(Sn/2))/(((((Sn/2)^2)+(Sp^2))^(1/2))-dto);
        Redmax = (rhowf(i)*umax*dto)/muwf(i);

        d = const(1);
        e = const(2);
        f = const(3);
        Nuwfmod(i) = d*(Redmax^e)*(Prwf(i)^f);

    %elseif modeltype == 'Bell-Delaware'
    elseif modeltype == 3
        % Rhombic arrangement of tubes
        Ai = const(1);
        Bi = const(2);
        Ci = const(3);
        Di = const(4);
        Ei = const(5);
        Fi = const(6);
```

```
        Ji = exp(Ai + Bi*log(Rewf(i)) + Ci*(log(Rewf(i))^2) +
Di*(log(Rewf(i))^3) + Ei*(log(Rewf(i))^4) + Fi*(log(Rewf(i))^5));

        % Recirculation flow effect correction
        jBc(1:25) = const(7:31);%[const(2) const(6) -0.185339 0.59250929 -
0.5964414 -1.3564474 16.400326 -116.51387 362.367998 -368.18466 1.18264455 -
19.614535 140.62959 -451.59784 478.689065 -1.1031648 16.9758369 -113.6298
396.869404 -457.40996 0.59140536 -8.7366322 56.8613935 -210.10305
253.214998]; %[0.991889 0.02071706 -0.185339 0.59250929 -0.5964414 -1.3564474
16.400326 -116.51387 362.367998 -368.18466 1.18264455 -19.614535 140.62959 -
451.59784 478.689065 -1.1031648 16.9758369 -113.6298 396.869404 -457.40996
0.59140536 -8.7366322 56.8613935 -210.10305 253.214998];
        N2 = 2/6;
        Fsbp = (pi*(Dis^2)/4)-6*(pi*((dto/2)^2));
        Jb = (jBc(1) + jBc(2)*N2 + jBc(3)*(N2^2) + jBc(4)*(N2^3) +
jBc(5)*(N2^4)) + (jBc(6) + jBc(7)*N2 + jBc(8)*(N2^2) + jBc(9)*(N2^3) +
jBc(10)*(N2^4))*Fsbp + (jBc(11) + jBc(12)*N2 + jBc(13)*(N2^2) +
jBc(14)*(N2^3) + jBc(15)*(N2^4))*(Fsbp^2) + (jBc(16) + jBc(17)*N2 +
jBc(18)*(N2^2) + jBc(19)*(N2^3) + jBc(20)*(N2^4))*(Fsbp^3) + (jBc(21) +
jBc(22)*N2 + jBc(23)*(N2^2) + jBc(24)*(N2^3) + jBc(25)*(N2^4))*(Fsbp^4);

        % Adverse Temp Gradient correction
        if Rewf(i) <= 20
            jRc(1:5) = const(32:36);
            N1 = 6+6;
            Jr = jRc(1) + jRc(2)*N1 + jRc(3)*(N1^2) + jRc(4)*(N1^3) +
jRc(5)*(N1^4);
        elseif Rewf(i) > 20
            jRc1(1:5) = const(32:36);
            N1 = 6+6;
            Jr1 = jRc1(1) + jRc1(2)*N1 + jRc1(3)*(N1^2) + jRc1(4)*(N1^3) +
jRc1(5)*(N1^4);
            jRc(1:16) = const(37:52);
            Jr = (jRc(1) + jRc(2)*Rewf(i) + jRc(3)*(Rewf(i)^2) +
jRc(4)*(Rewf(i)^3)) + (jRc(5) + jRc(6)*Rewf(i) + jRc(7)*(Rewf(i)^2) +
jRc(8)*(Rewf(i)^3))*Jr1 + (jRc(9) + jRc(10)*Rewf(i) + jRc(11)*(Rewf(i)^2) +
jRc(12)*(Rewf(i)^3))*(Jr1^2) + (jRc(13) + jRc(14)*Rewf(i) +
jRc(15)*(Rewf(i)^2) + jRc(16)*(Rewf(i)^3))*(Jr1^3);
        end

        % % Insert mu values for experimetal conditions & working fluid
        muwf = [];
        cpwf = (Prwf(i)*kwf(i))/muwf(i);

        hwf(i) = Ji*cpwf*((1/Prwf(i))^(2/3))*Jb*Jr;

        Nuwfmod(i) = hwf(i)*dto/kwf(i);

end

end
```

Appendix E: Results from Running Experimental Calculations and Optimizations

Adjusting for Losses (Using α and β Temperatures)

Table E.1: Best optimization results for the exhaust and working fluid Nusselt numbers and heat transfer coefficients taking ambient losses into consideration.

Working Fluid	Trial	T_α [K]	T_β [K]	$Nu_{ex,opt}$ [-]	$h_{ex,opt}$ [W/m^{2}K]	$Nu_{wf,opt}$ [-]	$h_{wf,opt}$ [W/m^{2}K]
Water	1	368.55	316.37	3861.97	5968.76	1.71	53.00
Water	2	364.56	317.25	3873.83	5963.64	1.69	50.46
Water	1	367.39	316.15	3877.10	5981.74	1.74	46.01
Water	2	365.02	317.02	3872.37	5963.13	1.74	40.57
Water	3	365.19	317.29	3862.12	5950.63	1.74	39.99
Water	3	372.73	320.55	3799.13	5933.29	1.73	40.46
EG	1	363.04	321.09	3849.67	5943.79	3.12	40.92
EG	2	365.56	322.15	3835.11	5948.02	3.11	41.43
EG	3	366.53	322.68	3826.23	5945.38	3.10	41.61
PG	1	361.77	325.30	3831.73	5938.00	3.78	30.95
PG	2	364.78	327.11	3811.02	5941.54	3.76	31.12
PG	3	366.32	328.07	3800.22	5943.24	3.74	31.28
50/50	1	364.50	322.08	3845.98	5956.45	2.20	50.18
50/50	2	364.14	325.19	3827.41	5948.09	2.21	35.96
50/50	3	363.88	326.40	3817.30	5939.45	2.21	31.82

Appendix F: Defining Flow via the Reynolds Number

For internal flow, turbulent flow begins at Reynolds' numbers greater than 2300. The range of experimental Reynolds' numbers for the exhaust flow in the WHR experiments (3446-3508) were within the turbulent range, while those for the exhaust flow in the DPFHX experiments (1524-1538) were within the laminar range, as discussed. The hydrodynamic and thermal boundary layer lengths for fully developed, internal flow were calculated using the following equations [29]:

$$\left(\frac{x_{fd,bl}}{2r_{tube,inner}}\right)_{laminar} \approx 0.05\,\mathrm{Re} \tag{F.1}$$

$$10 \le \left(\frac{x_{fd,bl}}{2r_{tube,inner}}\right)_{turbulent} \le 60 \tag{F.2}$$

$$\left(\frac{x_{fd,th}}{2r_{tube,inner}}\right)_{laminar} \approx 0.05\,\mathrm{Re}\,\mathrm{Pr} \tag{F.3}$$

$$\left(\frac{x_{fd,th}}{2r_{tube,inner}}\right)_{turbulent} = 10 \tag{F.4}$$

In the case of the utilized HEX, the value of $L_{tube}/(2r_{tube,inner})$ was 24, thus indicating fully developed thermal and hydrodynamic boundary layers for the turbulent WHR experiments (i.e., for (x/D) > 10, fully developed flow can be assumed). Furthermore, the lengths of the entry lengths were calculated as 0.1905 m for both $x_{fd,bl}$ and $x_{fd,th}$ in turbulent flow (i.e., WHR experiments), only 41.7% of the total length of the tube, indicating fully developed flow by the tube outlet. However, for laminar flow in the DPFHX experiments, the thermal and

hydrodynamic entry lengths were greater than the tube length ($x_{fd,bl}$ and $x_{fd,th}$ of 1.45 and 1.016 minimum, respectively), thus indicating developing flow.